Multivalency in the interaction of biological polymers

Dissertation
zur Erlangung des akademischen Grades

doctor rerum naturalium

(Dr. rer. nat.)

im Fach Physik

Spezialisierung: Experimentalphysik

eingereicht an der

Mathematisch-Naturwissenschaftlichen Fakultät

Humboldt-Universität zu Berlin

von

Dipl.-Phys. Valentin D. Reiter-Scherer

Präsidentin der Humboldt-Universität zu Berlin:

Prof. Dr.-Ing. Dr. Sabine Kunst

Dekan der Mathematisch-Naturwissenschaftlichen Fakultät:

Prof. Dr. Elmar Kulke

Gutachter:
1. Prof. Dr. Jürgen P. Rabe
2. Prof. Dr. Andreas Herrmann
3. Prof. Dr. Dario Anselmetti

Tag der mündlichen Prüfung: 3. August 2020

Abstract

Multivalency is ubiquitous in biophysical and biochemical processes, referring to the simultaneous interaction of several interaction partners, which may result either in an enhancement or an attenuation of the effect of the individual interactions. Proteins, such as the transmembrane proteins of the influenza virus hemagglutinin and neuraminidase, are a highly interesting class of biological polymers that fulfill many biologically relevant functions, such as cell signaling, by forming highly specific bonds with other proteins or ligands.

This thesis focuses on studying multivalent interactions between hemagglutinin as well as neuraminidase and the cellular ligand sialic acid by using scanning probe techniques, i.e. scanning force microscopy and single molecule force spectroscopy (SMFS). Unbinding forces as well as dissociation and association kinetics together with the free energy landscapes of two mayor influenza virus proteins of two different viral strains, namely the pandemic strains A/California/04/2009pdm (H1N1) and A/Aichi/2/1968 (H3N2), were, to the best knowledge for the first time, individually quantified on the single molecule level using SMFS. To this extent, monovalent and multivalent sialic acid displaying ligands, termed SAPEGLA and dPGSA, were employed.

Surprisingly, the experimental force spectra did not show the log-linear trend predicted by the classical Kramers-Bell-Evans model. To account for these deviations, the more recent Friddle-Noy-De Yoreo model was successfully applied.

It was expected that the bond strength of a cluster of SAPEGLA bound to proteins increases with the number of bonds in the cluster and that dPGSA binds to hemagglutinin with higher thermal stability than SAPEGLA, since its functional moiety had been specifically designed as a multivalent inhibitor of hemagglutinin. It was also presumed that the unbinding forces of hemagglutinin and neuraminidase are similar, since viral fitness depends on a precisely tuned balance of the fusogenic activity of hemagglutinin and the enzymatic activity of neuraminidase, which cleaves sialic acid, but subtle differences exist between viral strains.

The dissociation rate of neuraminidase was anticipated to be in the range of the enzymatic activity.

It was revealed that, despite similar unbinding forces, neuraminidase forms a more stable bond with sialic acid than hemagglutinin which holds true for both viral strains, and dissociates three to seven times slower. It is reasoned that the higher stability compensates for the lesser amount of neuraminidase compared to hemagglutinin that is typically found on the viral envelope. The unbinding forces of the cluster of monovalent ligands increased gradually with the number of bonds in the cluster and the dissociation kinetics follow the theoretically predicted trend.

The dissociation rate of neuraminidase was found to be about six times higher than its catalytic rate. It is concluded that multiple bonds are needed for cleavage of sialic acid. Interestingly, the dissociation rate of N1 neuraminidase is on the same order as that of H3 hemagglutinin. It is suggested that these similarities between the two strains favor the transmissibility of the influenza virus.

Furthermore, it is shown that the thermal stability of the bond between dPGSA and hemagglutinin is indeed higher that between SAPEG and hemagglutinin and that it is in the range of three to four SAPEGLA bonds. Such an enhancement of thermal stability could not be observed for the binding of neuraminidase. It is concluded that dPGSA binds specifically to hemagglutinin and that the binding strength of a multivalent ligand architecture depends not only on the degree of valency but also on the receptor specific presentation of the functional moieties.

By testing the probability of detecting specific binding events, this thesis also shows that SMFS could be used as a tool to screen antiviral inhibitors in competitive binding assays, which may contribute insight into the design of antiviral inhibitors on the single molecule level.

Keywords: Biophysics, Scanning Force Microscopy, Force Spectroscopy, Single Molecules, Multivalency, Cooperativity, Virus Inhibition

Zusammenfassung

Multivalenz ist in biophysikalischen und biochemischen Prozessen allgegenwärtig und bezieht sich auf das Zusammenwirken mehrerer Interaktionspartner, wobei es sowohl zu kooperativer Verstärkung wie kompetitiver Abschwächung kommen kann. Proteine, wie die Transmembranproteine des Influenzavirus Hämagglutinin und Neuraminidase, sind eine hochinteressante Klasse von biologischen Polymeren, die viele biologisch relevante Funktionen wie die Signalübertragung von Zellen erfüllen, indem sie hochspezifische Bindungen mit anderen Proteinen oder Liganden eingehen.

Diese Dissertation konzentriert sich auf die Untersuchung multivalenter Wechselwirkungen zwischen Hämagglutinin sowie Neuraminidase und dem zellulären Liganden Sialinsäure unter Verwendung von Rastersondenverfahren, d. h. Rasterkraftmikroskopie und Einzelmolekülkraftspektroskopie (SMFS). Bindungskräfte sowie Dissoziations- und Assoziationskinetiken, zusammen mit den intermolekularen Potentiallandschaften zweier Influenzavirus-Proteine zweier verschiedener Virusstämme, nämlich der pandemischen Stämme A / California / 04 / 2009pdm (H1N1) sowie A / Aichi / 2/1968 (H3N2), wurden, nach bestem Wissen erstmalig, separat auf Einzelmolekülebene mittels SMFS quantifiziert. Zu diesem Zweck wurden mono- und multivalente Sialinsäureliganden, die als SAPEGLA und dPGSA bezeichnet wurden, eingesetzt.

Überraschenderweise zeigten die experimentellen Kraftspektren nicht das vom klassischen Kramers-Bell-Evans-Modell vorhergesagte logarithmisch-lineare Verhalten. Um diese Abweichung zu berücksichtigen wurde das neuere Friddle-Noy—De Yoreo-Model erfolgreich angewandt.

Es wurde erwartet, dass die Bindungsstärke eines an Proteine gebundenen SAPEGLA-Clusters mit der Anzahl der Bindungen im Cluster zunimmt und dass dPGSA mit einer höheren thermischen Stabilität als SAPEGLA an Hämagglutinin bindet, da seine funktionelle Einheit als multivalenter, Hämagglutinin-spezifischer Inhibitor entwickelt wurde. Ebenso

wurde vermutet, dass die Bindungskräfte von Hämagglutinin und Neuraminidase ähnlich sind, da die virale Fitness von einem genau abgestimmten Gleichgewicht zwischen der fusogenen Aktivität von Hämagglutinin und der enzymatischen Aktivität von Neuraminidase, welche Sialinsäure spaltet, abhängt, wobei jedoch subtile Unterschiede zwischen den Virusstämmen bestehen. Es wurde erwartet, dass die Dissoziationsrate von Neuraminidase im Bereich der enzymatischen Aktivität liegt.

Es zeigte sich ungeachtet der untersuchten Virusstämme, dass Neuraminidase trotz ähnlicher Bindungskräfte eine stabilere Bindung mit Sialinsäure eingeht als Hämagglutinin und drei- bis siebenmal langsamer dissoziiert. Es wird vermutet, dass die höhere Stabilität die geringere Oberflächendichte von Neuraminidase auf der Virushülle im Vergleich zu Hämagglutinin ausgleicht. Die Bindungskräfte des Clusters monovalenter Liganden nehmen mit der Anzahl der Bindungen im Cluster allmählich zu und die Dissoziationskinetik folgt dem theoretisch vorhergesagten Trend. Es wurde festgestellt, dass die Dissoziationsrate der Neuraminidase etwa 6-mal höher ist als ihre katalytische Rate. Daraus wird geschlussfolgert, dass Mehrfachbindungen zur Spaltung von Sialinsäure erforderlich sind. Interessanterweise liegt die Dissoziationsrate von Neuraminidase (H1N1) in der gleichen Größenordnung wie die von Hämagglutinin (H3N2) und es wird vermutet, dass diese Ähnlichkeiten zwischen den beiden Stämmen die Übertragbarkeit des Influenzavirus begünstigen. Darüber hinaus wird gezeigt, dass die thermische Stabilität der Bindung zwischen dPGSA und Hämagglutinin tatsächlich höher ist als zwischen SAPEGLA und Hämagglutinin und im Bereich von drei bis vier SAPEGLA-Bindungen liegt. Eine solche Steigerung der thermischen Stabilität konnte für die Bindung von Neuraminidase nicht beobachtet werden. Daraus wird abgeleitet, dass dPGSA spezifisch an Hämagglutinin bindet und dass die Bindungsstärke einer multivalenten Ligandenarchitektur nicht nur vom Grad der Valenz, sondern auch von der rezeptorspezifischen Präsentation der funktionellen Einheiten abhängt.

Die in dieser Arbeit präsentierten Untersuchungen von Bindingswahrscheinlichkeiten verschiedenenr Kombinationen aus Proteinen und Liganden zeigen, dass SMFS zum Screening von antiviralen Inhibitoren in kompetitiven Inhibitonssassays verwendet werden kann und möglicherweise einen Zugang zum Design von antiviralen Inhibitoren auf Einzelmolekülebene liefern kann.

Schlagwörter: Biophysik, Rasterkraftmikroskopie, Kraftspektroskopie, Makromoleküle, Multivalenz, Kooperativität, Virus Inhibition

Contents

Chapter 1

Introduction

Biological polymers are ubiquitous constituents of all living matter. The term "polymer" encompasses an incredibly large class of materials that originate from synthetic as well as biological sources. Generally, it refers to macromolecular compounds built from individual subunits termed monomers. These monomers are covalently linked in the polymerization process and become the repeating units of the final polymer. In this sense, biological polymers, or biopolymers, are defined as "macromolecules formed by living organisms" [1] or alternatively as "substances composed of one type of biomacromolecule" [2].

Biological polymers can be subdivided into three classes based on the specific monomer or biomacromolecule. These classes are the polynucleotides, built from nucleotides, the polysaccharides, built from carbohydrates and the polypeptides, built from amino acids [3]. Polynucleotides, such as ribonucleic acid (RNA) and deoxyribonucleic acid (DNA), store the genetic code of an organism, required for reproduction. Polysaccharides, such as cellulose, provide structural stability and serve as a source of energy. Polypeptides fulfill various functions such as transportation or signaling [4].

Large polypeptides are referred to as proteins. Protein sizes vary from 50 to more than 30.000 amino acids [5, 6]. In suitable solution, the amino acid sequence of the protein folds into a three dimensional structure that enables proper function [7, 8, 9]. In particular, proteins contribute to cell mobility, transportation of metabolites, ion pumping and intermolecular recognition [10, 11, 12, 13].

Biophysical functions of biological polymers are governed by multivalent interactions, that are very often the result of an interplay of a multitude of different individual non-covalent molecular bonds, that cannot be described by the simple sum of the component bonds [14]. These interactions are typically highly dynamic and are governed by various forces such as shear stress, Van der Waals or Coulomb forces. While the non-covalent individual bonds are, in most cases, rather weak, the complex ensemble can increase the binding strength and therefore provide the base for the selection of useful combinations of receptors and ligands [15].

A common macroscopic example of such a strengthening through multivalency is the Arctium, which uses multivalent adhesion for seed dispersal [15]. The seed carrying burs of this plant are outfitted with dozens of tiny hooks that can snag to loops in the fur of animals or clothes. While the strength of a single hook-loop connection is weak, the combined strength of many connections ensures a strong binding. Once the burs have firmly attached to a carrier, they can get transported over large distances before they are stripped off. In this way the plant can spread its seeds over large areas.

A prominent example of multivalency in the biomolecular world is the interaction of enveloped viruses, such as the human immunodeficiency virus (HIV) or the influenza virus (IV), with host cells or antibodies. These viruses replicate by inserting their genome into host cells, where the viral RNA is copied and new virions are formed and released into the host. Once the virus has entered the host, the primary step required for replication is the attachment of the virion to the membrane of suitable host cells. This attachment is mediated by proteins present in the viral envelope. The proteins bind to cellular receptors and can initialize cell entry. Similar to the single hook-loop connection of the Arctium, a single protein-receptor bond is weak and will dissociate almost immediately due to thermal fluctuations and viscous shear forces. Therefore, to ensure sufficient residence time on the host cell membrane to become incorporated, the virus relies on multivalent binding of several individual proteins [16, 17, 18, 19]. Consequently, antibodies can bind to the virions using the same mechanism and annihilate the viral threat. The high degree of specificity of the multivalent protein-receptor interaction is also used in the design and development of antiviral drugs and inhibitors [20, 21, 22]. Despite continuous efforts and achievements in the field of viral research, viral infections

still pose a permanent threat to human health and prosperity. One of the major difficulties encountered when dealing with viral infections are the continuous mutations of the viral proteins involved in cell adhesion. These mutations can favor infectivity and transmissibility while simultaneously increasing drug resistance. Due to this complex behavior of a multitude of individual interactions, viral proteins represent an excellent example to study the multivalent interactions of biological polymers.

During the past decades an enormous effort has been undertaken to study the behavior and interactions of biomacromolecules and biological polymers. Insight in purpose and function of biological polymers was gained through fluorescence microscopy, nuclear magnetic resonance (NMR) spectroscopy, calorimetry experiments and binding assay studies, among other techniques [23, 24, 25, 26, 27, 28, 29, 30, 31]. These techniques typically provide ensemble-averaged information. Yet, despite such achievements, a full understanding of biomolecular interactions profits substantially from the knowledge of the involved forces on the single molecule level [32, 33, 34]. The nature of these forces can be hydrogen bonds, Van der Waals, Coulomb, hydrophobic, hydrophilic or capillary forces [35, 36, 37, 38].

About 30 years ago the toolbox for studying molecular phenomena was extended by the invention of the scanning force microscope (SFM) [39]. Originally conceived to reveal the topographies of non-conducting surfaces, the SFM quickly developed into a multifunctional tool that allows the measurement of mechanical and chemical properties, as well as intermolecular forces with unprecedented precision at high spatial resolution of a few nanometers [40]. The determination of these forces through SFM based single molecule force spectroscopy (SMFS) enables research of biomolecular interactions of biological polymers in their native environment on the single molecule level [41]. The forces required to rupture individual bonds provide the key to unveil the energy landscapes that govern the bonds between receptors and ligands, and thereby determine the stability of a certain receptor-ligand pair as well the rate of its dissociation [42]. Therefore, for a better understanding of the various ways of interaction between biological polymers, it is of vital importance to probe such energy landscapes [43]. Revealing those can shed light on the mechanics of dissociation of interacting biological polymers, as intermediate states, and different unbinding pathways can be determined.

In this sense SMFS could also be used for screening of new antibiotics and antivirals [44].

This thesis focuses on studying the multivalent nature of the interactions between biological polymers by means of SFM and SMFS. The scope of this work will be the interactions of the influenza virus proteins hemagglutinin (HA) and neuraminidase (NA) with their cellular receptor sialic acid (SA), because of their importance for antiviral research. The thesis will address the question, whether the binding of HA and NA to SA can be characterized on the single molecule level. It will be analyzed in which way the bond between HA and SA is different from the bond between NA and SA and how the kinetics of the bonds are affected by the valency. To this extent two SA displaying architectures were utilized that are referred to as SAPEGLA and dPGSA. The monovalent SAPEGLA was employed to study the kinetics of uncorrelated parallel bonds while the multivalent dPGSA was employed to observe true multivalency of correlated bonds. Differences in the binding and the energy landscapes of HA and NA of two different strains of IV, namely the pandemic strains A/California/04/2009pdm and A/Aichi/2/1968 (H3N2), will be discussed together with the biological relevance of the findings for viral fitness.

The thesis is organized as follows: In *chapter 2* biological polymers and the viral proteins HA and NA will be introduced as examples of such. Also the concepts of multivalency, SFM and SMFS will be illustrated. *Chapter 3* will describe the experimental procedures in detail. *Chapter 4* will present the results, starting with the visualization of virions and viral proteins through SFM imaging. Furthermore, the force spectra of the intermolecular bonds between SA and the two major proteins of the IV, HA and NA, will be presented. The multivalent and dynamic interactions will be characterized with the related kinetic parameters. These kinetic parameters include the dissociation rate, the potential energy landscapes and the dissociation constant. Additionally, the implications of the findings on the transmissibility and infectivity will be discussed. Finally, *chapter 5* will provide the conclusions and give a perspective for future research.

Chapter 2

Fundamentals

This chapter will introduce the principles of multivalency as well as biological polymers. In addition, the basic concepts of the applied techniques, namely scanning force microscopy (SFM) and single molecule force spectroscopy (SMFS), will be illustrated.

2.1 The Principle of Multivalency

Multivalency is ubiquitous in nature [45]. It is found in the interaction of small molecules that consist of only a few atoms, but also in large and complex structures, such as single cells or whole organisms [46].

In principle, the term multivalency refers to the combined interaction of more than one pair of interaction partners (*Figure 2.1*) [15]. Hereby, the total strength of the multivalently bound complex is not necessarily increased by combining the individual interactions but rather is influenced by the binding enthalpy that enhances binding and the loss in configurational entropy that inhibits binding [47]. This phenomenon is referred to as enthalpy-entropy compensation [48]. The paired interaction partners can work cooperatively together towards an increase of their individual effects, but their actions can also oppose each other, which will cause a weakening of the combined interactions [49]. This ambiguity is used by many chemical and biological processes to achieve a high level of specificity and selectivity [15, 50].

An example of these highly specific interactions are the various functions of proteins

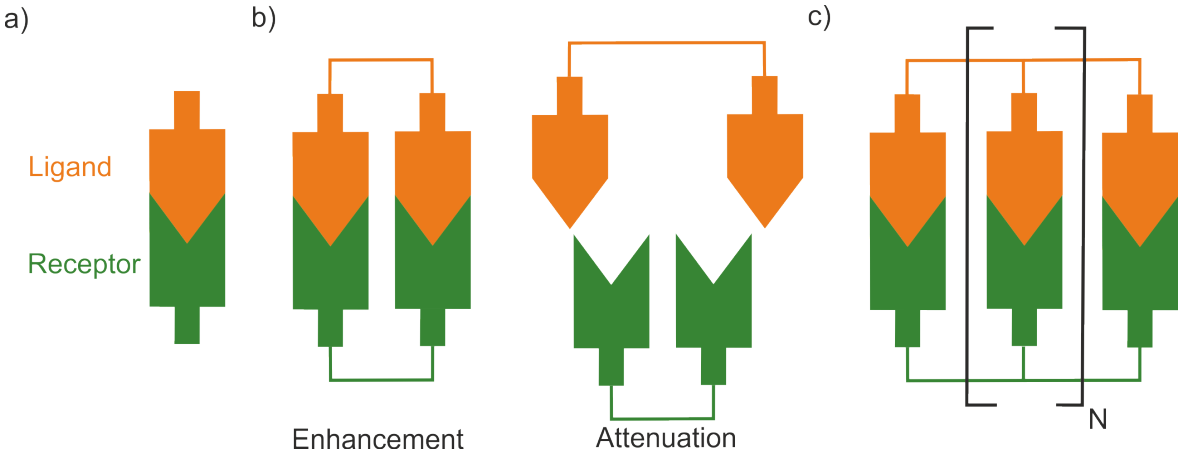

Figure 2.1 – ***Conceptual sketch of multivalency:*** *The different binding modes of ligand-receptor pairs are schematically shown. In a), the simplest conformation, monovalent binding, is shown. A single receptor is bound to a single ligand. In b), bivalent binding between two coupled receptors and two coupled ligands is shown. On the left, the spacing of the receptor coupling matches the coupling of the ligands. This will most likely result in higher bond strength. On the right side, the spacing does not match and hence the bond formation might be hindered. In c), the multivalent conformation of N receptors that are bound to N ligands is shown.*

[51]. Already in a single protein, multivalency is essential, since the protein will only be functional if it is folded into the proper tertiary structure [52]. The information that is contained in the sequence of amino acids, is not sufficient. In order to stabilize the folded structure, the protein relies on multivalent interactions between several amino acids that are mostly of hydrophobic nature [9]. Proteins often work by refolding and changing their tertiary structure. The refolding requires, that bonds that stabilize the folded structure are reversible and dissociate reasonably fast [53]. An advantage of multivalency is that a strong and stable connection can emerge as a result of several bonds that are individually much weaker than the absolute strength of the final complex. This property enables proteins to quickly break the stabilizing bonds and fold into new shapes.

2.2 Proteins as Examples of Biological Polymers

The term biological polymer, or biopolymer, refers to a broad class of materials of various origin and function and can be man-made or of natural origin. Generally speaking, biopolymers are macromolecules that are built from biological monomers [1]. The three fundamental monomers are the nucleotides, which assemble to DNA and RNA, the carbohydrates, which form polysaccharides and the amino acids, which form polypeptides [3]. Long polymers with a molecular weight of more than $10kDa$ and therefore consisting of more than 50 amino acids are named proteins [54]. Proteins are not just simple peptide chains in random configurations, but instead they form distinctive secondary and tertiary structures [55, 56, 57]. Secondary structures emerge when the peptide chain is twisted, which results in the so-called $\alpha-$ and $\beta-$ sheets. The tertiary structures emerge as a consequence of folding of the twisted peptide chain. The precise determination of the specific protein structure is a challenging task and is the goal of many investigations. Valuable insight in the mechanisms of protein folding and stability can also be gained from SMFS. For example, a pioneering study by Hermann Gaub and colleagues revealed the binding forces that govern the secondary and tertiary structure of recombinant titin immunoglobulin segments [58]. In this work the protein was held at both ends and stretched by using a scanning force microscope. Many of the various functions of proteins depend on the correct folding, which can also be alternated as a response to changes in the surrounding environment.

2.3 The Influenza Virus, Hemagglutinin and Neuraminidase

2.3.1 General Structure of the Influenza Virus

The influenza virus (IV) can be considered as a major threat to human health as it causes seasonal epidemics and occasional pandemics [59, 60]. Estimations by the World Health Organization (WHO) account for annually $\sim 10^9$ infections worldwide, of which $\sim 5 * 10^6$ lead to severe illness, causing $\sim 0.4 \times 10^6$ deaths [61]. The IV belongs to

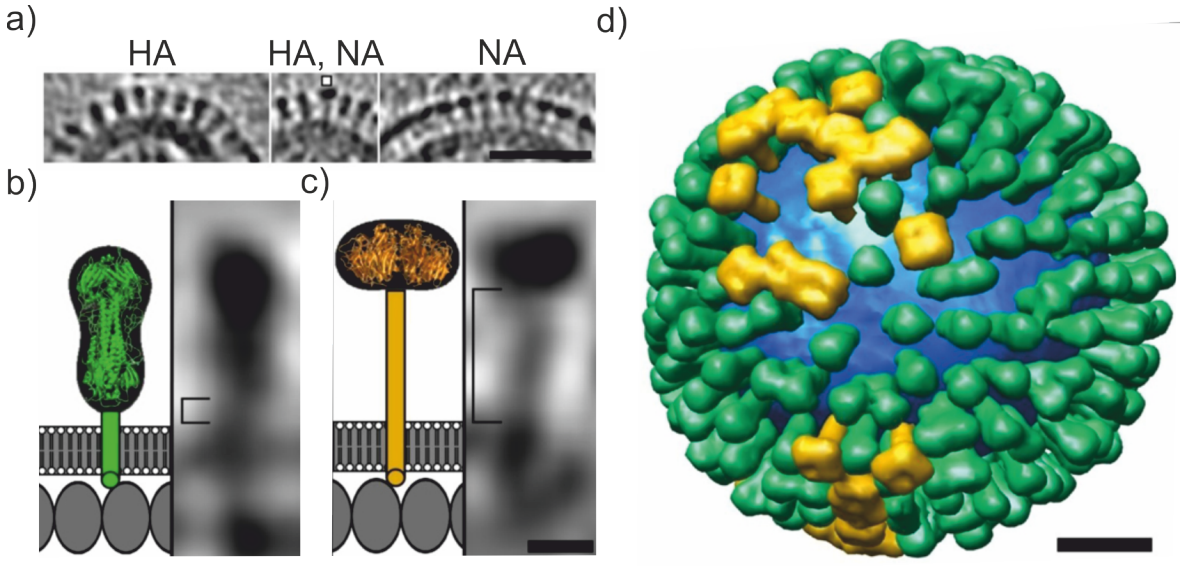

Figure 2.2 – ***Differentiation of HA and NA on X31 A/Aichi/68 (H3N2) virions using cryo-electron microscopy:*** *a) A cryo-electron microscopy images of different regions on the viral membrane are shown. From left to right, the images show a region that is occupied by only HA, an NA surrounded by HA, and a region only occupied by NA. (Scale bar:* $50nm$*.) The crystal structure and corresponding cryo-electron microscopy image is shown for HA in b) and for NA in c). (Scale bar:* $5nm$*.) The model of the virion that was derived from the analysis of the protein distributions is displayed in d). The model illustrates the arrangement of NA spikes in patches, but also isolated NA are visible. (Scale bar:* $20nm$*.) The image was reproduced from [66].(Copyright (2006) National Academy of Sciences, U.S.A)*

the family of enveloped viruses, which means that the viral RNA is encapsulated by a membrane [62]. The RNA is single stranded and the genome is segmented [63]. Encoded in the RNA segments are the RNA polymerase subunits, the viral glycoproteins, the nucleoproteins, matrixproteins, the nonstructural proteins NS1 and the nuclear export proteins [64]. The glycoproteins can be further subdivided into hemagglutinin (HA) and neuramindiase (NA) [65]. HA and NA are essential for viral entry into and exit from host cells. Both proteins were individually identified and their distribution on the viral membrane was visualized by Harris and colleagues using cryo-electron tomography [66]. It was shown in that study that the ratio HA:NA is about 6:1 and that NA assembles in patches. This is illustrated in *Figure 2.2*.

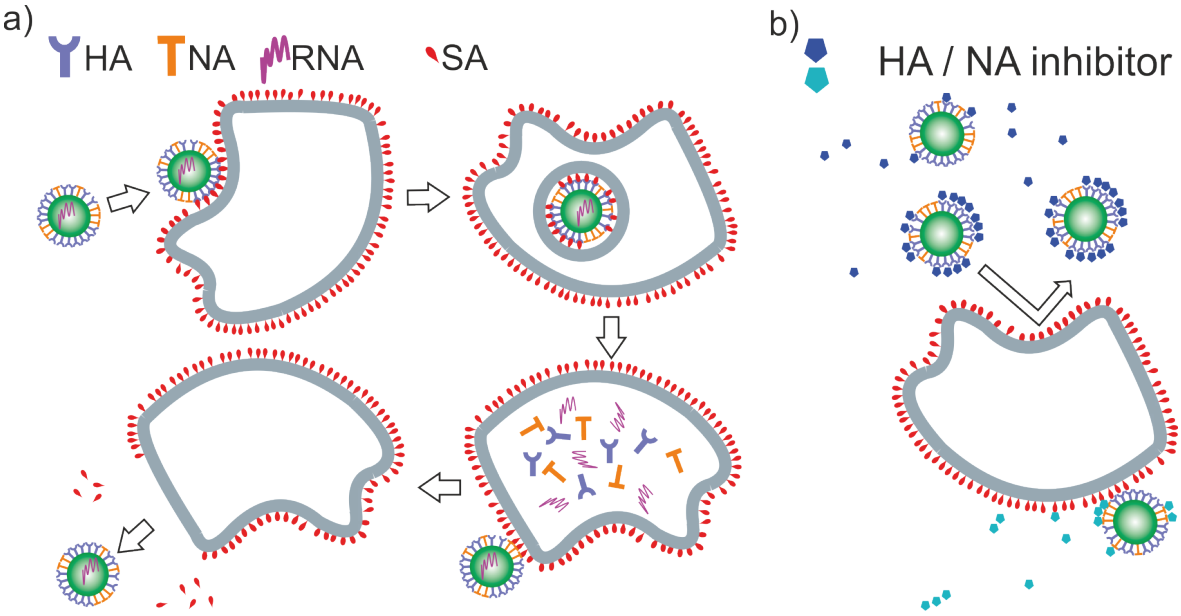

Figure 2.3 – ***Viral replication cycle and its inhibition:*** *In a), the replication cycle of an IAV is sketched. In the first step of the infection, the virion attaches to the membrane of the host cell through interaction of viral proteins with cellular glycoproteins. Following the initial attachment, the virion is taken up by the host cell where the genome and proteins are replicated. After replication of the genome, new virions are built at the membrane of the host. Cleavage of the cellular glycoproteins enables the release of the new virions. b) Inhibition of viral infection is focused on the design of small molecules that bind to the viral proteins with an affinity that can compete with the affinity between the proteins and the cellular ligand.*

In order to enter the host cell, the IV does not directly penetrate the cell membrane of the host, as it is done by similar viruses, but instead forms a vesicle after fusing with the cell membrane [16]. That process is called endocytosis and is depicted in *Figure 2.3* [67].

It is widely believed that the initial adhesion of a virion to a host cell is mediated by the HA binding to sialic acid (SA), which is a terminal sugar found on the glycoproteins of epithelial cells [68]. From nuclear magnetic resonance (NMR) experiments it is known that the binding strength of individual HA to SA is weak [23, 25]. Therefore, a multitude of these weak interactions is used by the virion to provide a stable attachment required for viral uptake [69]. Once the viral genome has been copied, the new proteins

and RNA segments are transported to the host cell membrane where the budding takes place and new virions are created [61]. These new virions are still bound to the host cell through the interaction of HA with SA [70]. Also virions can stick to one another and form aggregates [71]. The release of the virions from the cell and the separation of the aggregates is promoted by the NA, which is known to have an enzymatic activity that cleaves SA residues from glycoproteins [72]. It is obvious that a precisely tuned balance between the fusogenic activity of HA and the enzymatic activity of NA is required for effective viral replication, since both proteins share the same ligand [73, 74, 75, 76].

Current treatment of IV infections is based on the inhibition of the enzymatic activity of the NA. This is to some degree because the ligand binding domain (LBD) of NA is conserved through most influenza subtypes [77]. Inhibitors have been developed in order to inhibit viral spreading within the host after an infection has occurred. Two NA targeting inhibitors, zanamivir (ZV) and oseltamivir (OV), are commercially available and are frequently applied in medical treatment of infections. Even though their binding affinity to NA and an inhibitory effect in a variety of different influenza strains have been confirmed, they do not prevent initial infection or counteract symptoms, and only shorten the duration of illness by a small amount of time [78]. In addition to this, their effectiveness is further reduced due to recently emerging IV mutants that are resistant to ZV and OV [79, 80]. Therefore, current efforts in the struggle against influenza are focused on the inhibition of the HA. Gold nanoparticles presenting multiple SA have shown good inhibitory effect in in-vitro experiments [20, 21]. Current approaches focus on fulfilling the need for less toxicity and more bio-compatibility. To this extent scaffolds based on polyglycerol, DNA and peptide-polymer conjugates are highly interesting candidates [22, 81, 29, 82].

2.3.2 Hemagglutinin

Hemagglutinin is the most abundant protein, that is found on the viral envelope. It is a homotrimer, that is composed of 3 monomers of which each has a molar weight of $\approx 84kDa$ [83]. The monomer, that is also referred to as HA0, can be divided into two subunits, that are termed HA1 and HA2. HA1 has a peptide length of about 327 amino acids while HA2 is composed of about 222 amino acids [84]. Both subunits

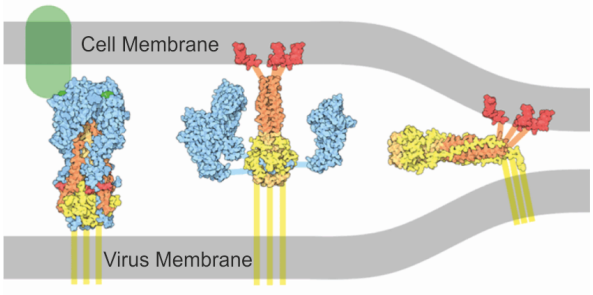

Figure 2.4 – ***Fusogenic action of hemagglutinin:*** *After attaching to the terminal SA of the glycoproteins of the host cell, the HA changes its conformation and pulls the membrane of the virion and the host cell together. This process is triggered by a reduction of the pH-level in the surrounding environment and initiates membrane fusion. The image was reproduced from https://pdb101.rcsb.org/motm/76.*

are linked by disulfide bonds. The globular head domain is completely located in the HA1 subunit, but the stem domain reaches over the HA1 and the HA2 subunit. The HA has a rod-like shape with a length of about $13.5nm$ and a diameter of about $6nm$ [83]. Hemagglutinin is responsible for the primary attachment of virions to the host cells. To fulfill this function, the head possesses an active binding site, that can bind to terminal sialic acid that is located on the glycoproteins of the host cell. In the trimer, the binding sites of the individual monomers are separated by a distance of about $3.5nm$ [85]. Upon attachment, HA mediates the fusion of the viral membrane with the host cell membrane. This is initiated by a change of the conformation, that is triggered by a reduction of the pH of the surrounding medium. Before cell adhesion, the HA can be seen as a spring loaded trap [86]. Immediately after attaching to the cellular glycoproteins, the HA undergoes a conformational change and pulls the viral membrane and the cell membrane together (see *Figure 2.4*). The fusion of the membranes triggers the endocytosis and allows the virion to enter the host cell.

2.3.3 Neuraminidase

As previously mentioned, neuraminidase (NA) is the second major protein that is found on the viral membrane on the influenza virus, but the virions feature significantly fewer NA than HA spikes. For example, cryo-electron microscopy studies that were conducted

by Harris and colleagues revealed that virions of the strain X-31 A/Aichi/68 (H3N2) displayed approximately 40-50 NA spikes opposed to 300-400 HA spikes [66]. It was also revealed in this study that the NA spikes were not distributed homogeneously over the surface of the virion, but rather were arranged in patches with an average center-to-center distance between proteins of $\approx 11nm$. Cryo-electron microscopy images and the derived model of the virions are shown in *Figure 2.2*. The general structure of neuramindiase can be described as a globular head on a thin stalk. This crude description can be refined by a closer examination. The neuraminidase is composed of four identical polypeptides that form a homo-tetramer [72]. The monomers, which have a peptide chain length of about $470nm$, can be subdivided into 4 domains, that serve different functions: The N-terminal cytoplasmic, the transmembrane, the stalk and the head domain [77]. The cytoplasmic domain, which is composed of merely 6 amino acids, is almost completely conserved across all influenza A subtypes, but its function has not been fully uncovered. The hydrophobic transmembrane domain fulfills two important functions. For one, it anchors the protein in the viral membrane. Secondly, it functions as a signal peptide and directs the NA across the endoplasmatic reticulum. The stalk of the NA of different subtypes can have various lengths [72]. Variations in the stalk length occur to such an extent, that the NA spikes protrude the HA spikes, but also the NA can lay below the HA [77]. Evidence that the stalk length is critically important for viral fitness has been reported in several studies, as reviewed by Munier and colleagues [87]. Overall, this appears to be a reasonable assumption, since a longer stalk would render the NA more accessible to SA binding. At the end of the stalk domain, the catalytic head domain follows. Each monomer in the head domain contains one active site, which is spatially and sequentially conserved to a high degree [77, 88]. The active site is responsible for the enzymatic activity of the NA and can cleave SA from the cellular glycoproteins or the mucus of the host [89]. Some, but not all, NA subtypes feature a second cavity in close proximity to the active site [90]. The function and importance for the viral life cycle of this cavity are still under debate. It is proposed that this secondary binding site can assist in adhering to host cells, as it can bind to SA at faster rates than the active site, but does not show catalytic activity [91, 92].

2.4 Scanning Force Microscopy

The scanning force microscope (SFM), also referred to as atomic force microscope, was invented by Gerd Binning, Calvin Quate and Christoph Gerber in 1985 [39]. The concept was based on the scanning tunneling microscope (STM), which at that time was an established tool to determine surface structures on an atomic scale. The STM made use of the tunneling current that occurred between a sharp probe and a surface at close proximity [93]. With the requirement of keeping the tunneling current constant, the probe had to follow the topography of the surface, revealing it in the process [94]. The drawback of the technique was that the surface had to be conductive to a certain degree. Non-conductive samples could not be studied, unless they had been treated with a thin metal coating [95, 96]. This, of course, was not possible with all samples. Especially biological particles such as cells, viruses, proteins and membranes were very likely to be damaged in the coating process and lose their original structure and functionality [97]. In order to profile these delicate samples, the SFM uses a sharp tip attached to the end of a flexible cantilever as a probe [98, 99, 40]. The apex of the tip mainly interacts with the surface via Coulomb forces at long distances between tip and surface while at short distances Van der Waals interactions predominate [100]. The interaction forces cause a deflection of the cantilever that is detected by an optical detection system. This system uses a laser beam that is focused on the end of the cantilever and reflected by the cantilever onto a photodetector. Typical diodes consist of four photodiodes arranged in a square, which is known as a four-quadrant detector. This diode arrangement not only detects the vertical deflection of the cantilever, but also the lateral deflection, which is caused by torsion around the long axis of the cantilever [101, 102]. The lateral movement as well as the height of the SFM probe relative to the surface is controlled by piezoelectric elements, which allow changes in the range of a few Å.

Several modes of imaging are available in modern SFM instruments. Among these are contact mode, tapping mode and force-spectroscopy mode and detailed descriptions of each mode can be found in many reviews [103, 104, 105, 106, 40, 107]. These fundamental imaging modes are illustrated in *Figure 2.5* and their basic working principles will be summarized as described in the mentioned reviews. The most basic

mode is contact mode [108]. In contact mode the tip is held in permanent contact with the sample surface, while it raster-scans line wise over the surface. The deflection of the cantilever, caused by the tip-surface contact, is kept constant by a feedback loop that regulates the tip-surface distance relative to the features on the surface [100]. The contact mode offers a high lateral resolution. Careful sample preparation provided, crystal lattice structures can be revealed [109]. Despite its high resolution, contact mode is not always the most appropriate mode. As a consequence of the constant contact between tip and sample, this mode is prone to exert large lateral forces on the sample [110]. That is especially true for samples with large features or high roughness of the surface but also for soft biological samples. Hence, in general, resolution of the crystal lattice can only be achieved on small scanning areas, with lateral dimensions below $100nm$.

The second commonly used mode of imaging is the tapping mode, also called 'intermitted contact' mode. In tapping mode, the SFM cantilever is actively driven to oscillate at a frequency near its resonance frequency [111]. The amplitude of the oscillation is used as a feedback to control the height of the SFM tip. As long as the distance between the tip and the sample is large, the cantilever oscillates with its free amplitude. As soon as the tip gets close to the sample, the free amplitude is damped. Damping of the amplitude also occurs as a result of changes in the topography or roughness of the sample that are encountered by the tip while scanning. The feedback loop can then react to the damping by adjusting the height of the tip relative to the sample. Keeping the amplitude of the cantilever oscillation constant is one way to profile the sample. This is termed amplitude modulation. A damping of the oscillation amplitude is always accompanied by a reduction of the oscillating frequency. Hence, it is also possible to use changes in the frequency as feedback for the control of the cantilever holder. This is termed frequency modulation [100]. A typical SFM image, which was obtained in tapping mode using amplitude modulation, is shown in *Figure 2.6 a)*. The image shows a red blood cell (RBC), or erythrocyte, which was immobilized on a glass slide. The disk-like structure with a diameter of approximately $8\mu m$ is clearly visible. The inset shows an scanning electron microscopy image of 3 RBC.

Depending on the magnitude of the lateral forces and the stability of the sample,

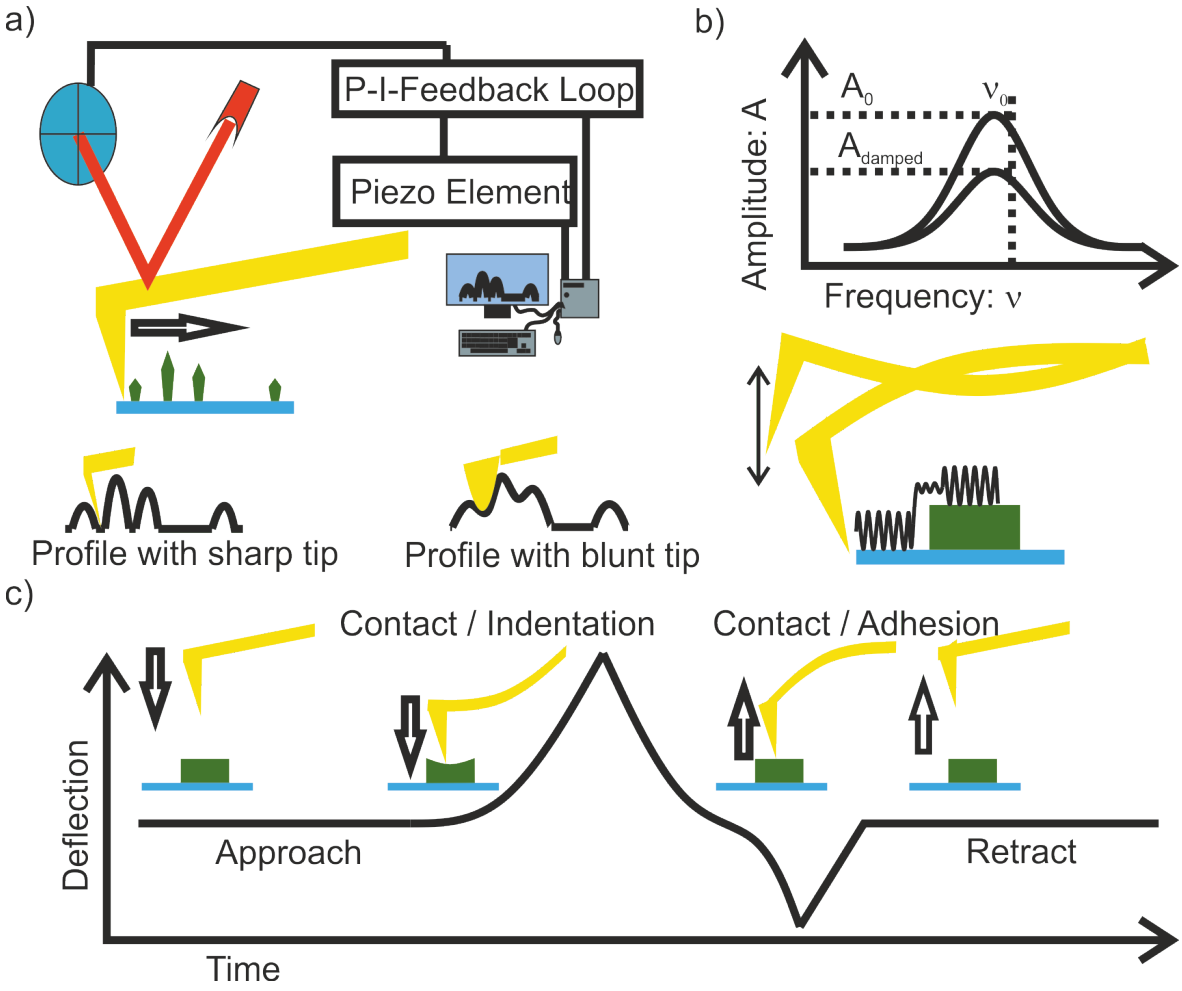

Figure 2.5 – ***Fundamental imaging modes of SFM:*** *In SFM imaging, a sharp tip on a flexible cantilever is used as a stylus to profile the topography of a sample surface. A laser beam, which is directed on the cantilever and reflected onto a photodiode array, is used to detect the deflections of the cantilever, which result from tip sample interactions. A feedback loop and piezo-electric elements control the height of the cantilever. In a), the general setup and the principle of contact mode are illustrated. In contact mode, the tip is kept in constant contact with the sample. Below the setup, the resolution limit as a result of tip geometry is illustrated. Only sharp tips can profile small features, which are overlooked by blunt tips. In tapping mode, b), the cantilever is driven to oscillate at a set amplitude. Upon contact with the sample, or as a result of changes in the sample topography, the amplitude is damped, which can be used as a feedback. In c), the quantitative nano-mechanical (QNM) imaging mode is illustrated. In QNM mode, the sample surface is probed point-wise with so-called force-separation curves. This allows determination of mechanical and chemical properties.*

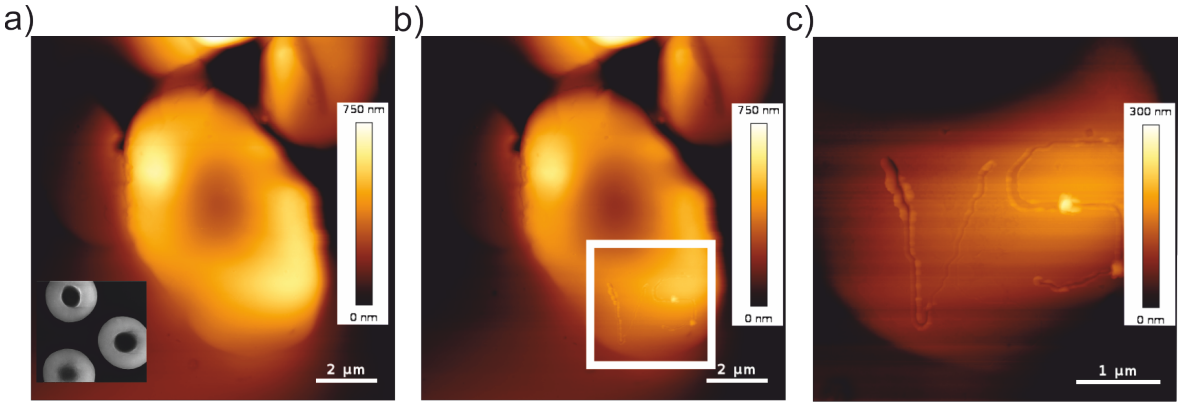

Figure 2.6 – ***Cutting of an erythrocyte by SFM based force manipulation:*** *The figure illustrates the capability of SFM to manipulate and cut biological particles, such as cells. a) The image shows the topography of an erythrocyte that was obtained from human blood. The inset shows an SEM image of erythrocytes. The inset was adopted from [112]. The structures correlate well with the structure that was found using the SFM. b) The same erythrocyte as in a) is shown after a cut had been inflicted with the tip of the SFM force probe. The cut is located in the area marked by a white box. c) The area with the cut is shown in more detail.*

the tip can inflict damage by shifting parts of the sample over the surface or destroying soft particles, such as cells or viruses [113]. While, on the one hand, these interactions of the tip with the surface can render the images obtained in the process useless, the modifications of the surface by the SFM tip can also, on the other hand, be applied intentionally [114, 115]. A simple example of such a manipulation of a soft sample is illustrated in *Figure 2.6 b)* and *c)*. After obtaining the initial image, the tip was moved along a defined pathway while a considerably high force was sustained on the cantilever. Further imaging revealed that the tip had cut into the surface of the RBC. Some of the material that was carved out of the cut can be seen as small dots along the line of cutting.

Over the years, SFM has evolved from a means to simply profile the topography of an underlying sample to a multifunctional tool that enables researchers to probe mechanical and chemical properties on the nanometer scale [99]. This progress is owed to a large extent to the invention of the quantitative nano-mechanical imaging (QNM) mode, which can be credited to Manfred Radmacher and colleagues [116]. In principle,

QNM mode imaging maps the attractive and repulsive forces between the SFM probe and the sample surface [117]. To this extent, the sample is imaged by measuring so-called force separation curves [118]. In these force-separation curves, the SFM tip approaches the sample surface, starting from a distance, that is outside the interaction potential between tip and sample. Hence, no acting force is detected by the SFM cantilever. When the tip is close enough to the sample, attractive forces cause the tip to snap into contact with the sample. When the tip is approached further, the cantilever relaxes at first, which is followed by the tip indenting the sample. As the tip indents the sample, the force acting on the cantilever rises depending on the elasticity of the sample. If the sample is rather stiff, the force will increase almost linearly with a steep slope. The slope S is related to the spring constant of the SFM cantilever k_c and the indentation depth d through the relation $S = k_c * d$. If the sample is elastic, the force will increase continuously depending on k_c and the Young's modulus of the sample. The Young's modulus can be obtained by fitting the part of the force separation curve that is associated with the indentation [119, 120]. One fit model for elastic deformation is the Hertz model. It is given by *Equation 2.1.* In this particular form the Hertz model is valid for an indenter, that is shaped like a circular paraboloid [119].

$$F(\delta) = \frac{E}{1-\nu^2}\frac{4\sqrt{r_{tip}}}{3}\delta^{3/2} \tag{2.1}$$

Here F denotes the force, E the Young's modulus, ν the Poisson ratio, which describes the ratio of transverse strain to axial strain, r_{tip} the radius of the SFM tip and δ the indentation depth. The Hertz model suffers from the fact that it does not include the adhesive forces between tip and sample. However, it is well suited to describing measurements performed in fluid since the fluid screens these forces, thereby reducing their importance.

The attractive forces can be included in the determination of the Young's modulus by using the Derjaguin-Müller-Toropov (DMT) model [121].

Typically, the tip will approach the sample until a defined setpoint force is reached. After reaching the setpoint, the movement is reversed and the tip is retracted. It is commonly observed that the tip adheres to the sample upon retraction and hence adhesive forces between tip and sample can be measured. If the tip is retracted to such

an extent that the forces acting on the cantilever exceed the adhesive forces, the tip breaks loose from the sample and the cantilever relaxes almost instantaneously. The topography of the sample can be obtained from the separation of the tip from the sample at a given force F. Typically, the setpoint force chosen as a reference for the topography. As an alternative the topography is determined from displacement of the force probe at the moment where the force starts to increase.

An example of a such a quantitative determination of mechanical properties with a lateral resolution on the nanometer-scale is shown in *Figure 2.7*. The figure is part of the investigation on the catalytic effect of zinc-oxide (ZnO) particles in sulfur-vulcanized butadiene-styrene rubber that was conducted by Yulia Glebova and colleagues [122]. In this study, the stiffness of the polymeric rubber matrix was analyzed with respect to the proximity to the ZnO particles, that were embedded into the rubber matrix. In *Figure 2.7 a)*, the topography of the rubber sample is shown. The angular protrusion in the center of the image was identified as ZnO with the help of scanning electron microscopy (SEM) and energy-dispersive X-ray spectroscopy (EDS). The colored points in the image correspond to the example force-separation curves that are shown in *Figure 2.7 b)*. The curve, that was taken directly on the ZnO particle features an almost vertical increase of the force, as the tip makes contact with the particle. This is a direct consequence of the hardness of the ZnO particle. In contrast, the rubber matrix can be indented by the tip. The slope of the force-separation curve during indentation becomes shallower with increasing distance from the ZnO particle. The Young's modulus of the rubber sample was obtained from fitting the curves with Hertz model. The authors concluded that the high stiffness of the rubber matrix close to the ZnO particle was due to the enhanced sulfur cross-linking of the rubber polymers as a result of the catalytic activity of ZnO.

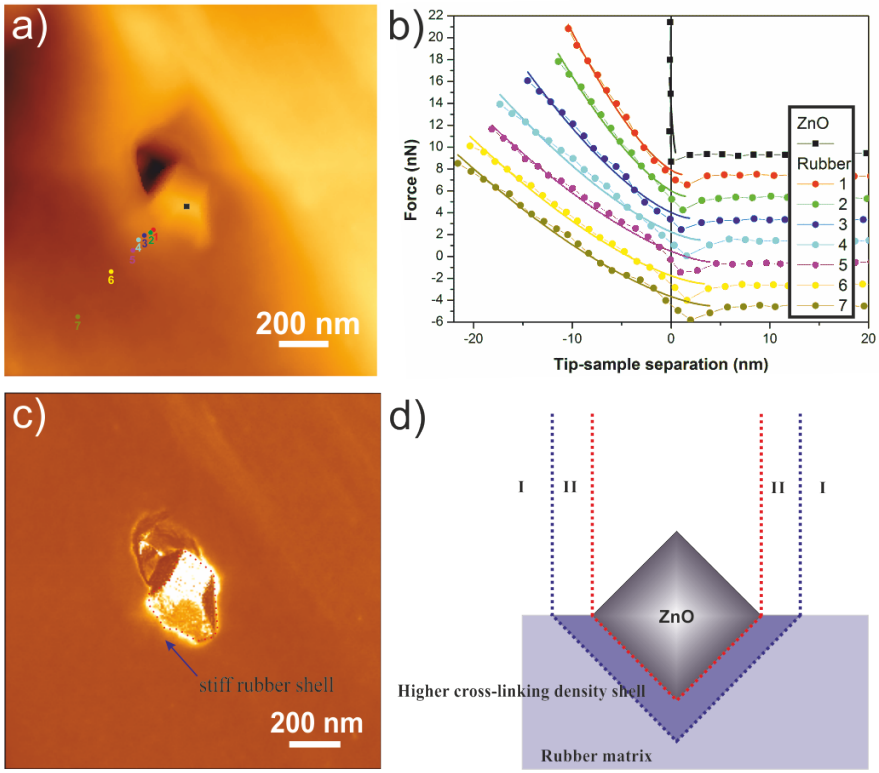

Figure 2.7 – ***Quantitative nano-mechanical mapping of the molecular structure of butadiene-styrene rubber:*** *The figure shows the capability of the SFM to map the topography and mechanical properties simultaneously on a nanometer scale. a) The topography of sulfur-vulcanized butadiene-styrene rubber was mapped by measuring force-separation curves over a 256*256 points matrix. The color scale from black to white represents 454nm. The angular protrusion in the center of the image is a ZnO-particle that was used as a catalyst in the vulcanization. The colored dots mark the points where the force-separation curves shown in b) were taken. b) The force-separation curves, that correlate to the marked spots in a) are shown. For clarity, only the approach curves are shown. Within the contact region, the curves feature a force gradient* $\frac{dF}{dx}$*, that decreases with the distance to the ZnO-particle. A steeper gradient is related to an increased Young's modulus. The thick solid lines represent the fit according to the Hertz model, which was used to determine the Young's modulus at each point. The calculated Young's modulus is shown with a color scale in c), with brighter points corresponding to a higher Young's modulus. In d), the model that was concluded from QNM imaging is shown. The image was adopted from [122].*

2.5 Single Molecule Force Spectroscopy

The upcoming section will illustrate the development of single molecule force spectroscopy (SMFS) and introduce the essentials of the technique. Firstly, a general introduction into forced dissociation will be given. Secondly, the most common models that are used to describe bond dissociation under external forces will be outlined. This part will introduce the Bell-Evans model, which was developed by Evan Evans and is based on Bell's formulation of Kramers' rate equations. This description is considered the standard model of dynamic SMFS. A later model developed by Raymond W. Friddle, Alexander Noy and James J. De Yoreo extends Evans' classical equation and is applicable to a broad variety of force spectra. This model will be outlined in the last part of this section.

2.5.1 Dissociation of Molecular Bonds under External Forces

In the macroscopic world the stable bond between two objects or surfaces is achieved if the attractive forces between the objects exceed the forces that act towards separation of the objects. An example would be two magnets that bind due to their magnetic force and are pulled apart by an external force. As long as the external force f_{ex} is smaller than the magnetic force f_{mag}, the magnets will remain connected for an infinitely long time. On the other hand, if f_{ex} is larger than f_{mag} the bond will fail immediately.

This simple picture does not hold true in the molecular world, where the stability of bonds has always to be seen with respect to time and thermal energy k_BT, which causes spatial fluctuations of the binding partners [123]. Here k_B is the Boltzmann constant and T the temperature. At a temperature $T > 0K$ a bond between two molecules will always fail at some time, if enough time is given for spontaneous dissociation. Therefore, it makes sense to use an average bond lifetime τ as a parameter to describe intermolecular bonds. An example for such an intermolecular bond would be a metal-chelate complex, which was extensively studied by Gensler and colleagues [124, 125]. In this study, the interaction of pyridine compounds, which is mediated by a metal ion, was investigated. If such a pyridine-ion complex is separated by an external force, the bond can be described by an energy landscape along the separation distance. A

conceptual sketch of a simple energy landscape is shown in *Figure 2.8*.

The energy barrier is characterized by an energetic minimum and a barrier height. The distance along the reaction coordinate between the minimum and the energy barrier is called the rupture length, or transition state distance [130]. It can seen as a measure for the malleability of the system that quantifies its ability to deform under load without rupturing [131, 125]. The actual shape of the energy landscape is typically not known and can be quite complicated. This is especially true for the bonds between complex macro-molecules [128]. These bonds might also unbind via various unbinding pathways or over several successive energy barriers, resulting in highly complicated energy landscapes. An external force that is applied to an intermolecular bond is always directional and it alters the energetic profile. In the simplest case, the external force will simply lower the height of the energy barrier but not change its location [128]. An example would be a deep harmonic well with steeply rising boundaries. In the case of more complex profiles, the location of the energy barrier can shift as well.

Early on, in 1940, a theoretical framework for calculating the rates that govern molecular interactions was developed by the Dutch physicist Hendrik Anthony Kramers [132]. His publication "Brownian motion in a field of force and the diffusion model of chemical reactions" was widely seen as a breakthrough in reaction-rate theory. Kramers' work is closely related to the transition state theory for reactions in gases that was proposed Henry Eyring, Meredith Gwynne Evans and Michael Polanyi among others [133, 134, 135]. That framework was later expanded by Peter Hänggi, Peter Talkner and Michal Borkovec [135]. Kramers' theory is based on the fundamental Van't Hoff-Arrhenius equation that is given in *Equation 2.2* [136]. Hereby k denotes the rate of escape from the stable state, E_b the activation energy threshold, and β the inverse of the Boltzmann thermal energy, which is the product of the absolute temperature T and the Boltzmann constant k_B. ν is a prefactor that has to be determined for the particular reaction.

$$k = \nu * \exp\left(-\beta E_b\right) \tag{2.2}$$

The precise determination of the prefactor ν can be seen as the holy grail of classical rate theory. The concept of forced dissociation of intermolecular bonds was introduced to

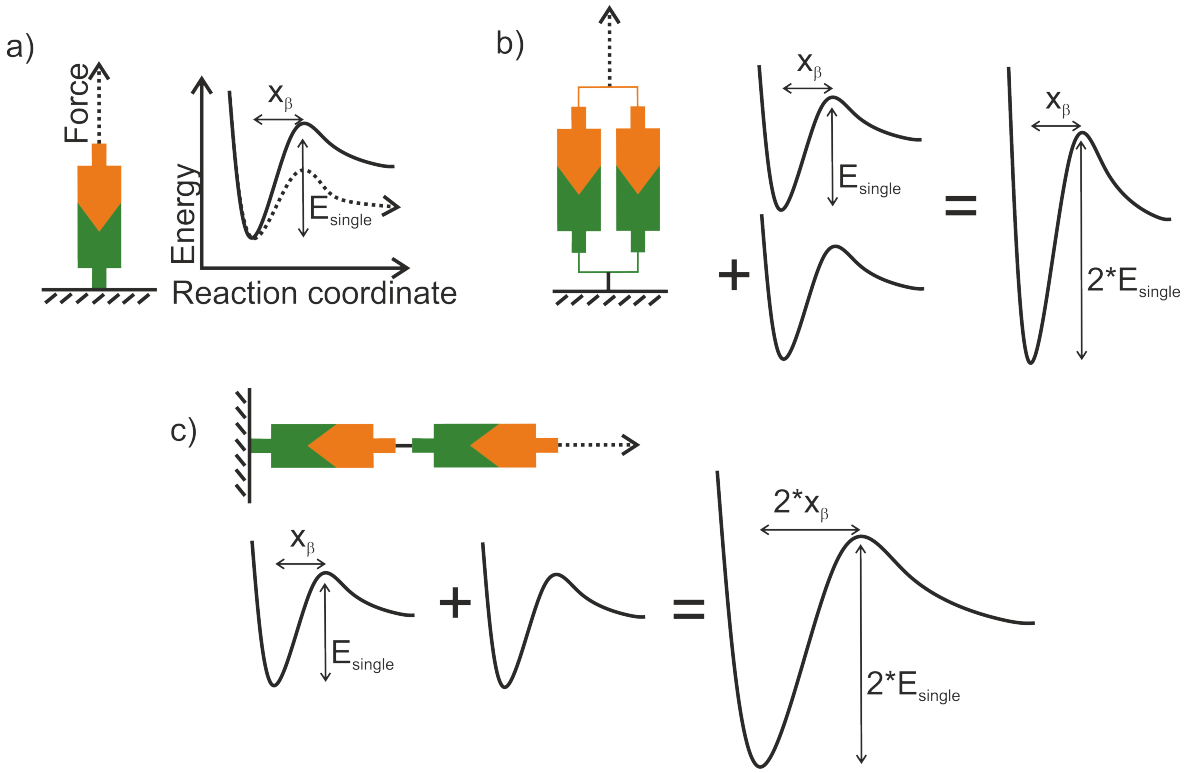

Figure 2.8 – ***A conceptual sketch of energy landscapes of intermolecular bonds:*** *a) A single intermolecular bond between a ligand a receptor can be approximated by an energy landscape that features a potential well. The potential well is characterized by the activation energy E_{single}, which imposes an energy barrier, and the distance x_β between the energetic minimum and the transition state, which is referred to as the rupture length. As a result of thermal fluctuations, the bond can overcome the energy barrier and dissociate. Application of an external force lowers the energy barrier increasing the rate of dissociation [126, 127, 128]. b) A combination of two identical uncorrelated intermolecular bonds arranged in parallel can be described with a single energy landscape that is characterized by an activation energy $2 * E_{single}$ and x_β of the single bond. c) The energy landscape of two identical uncorrelated intermolecular bonds in serial arrangement is characterized by the activation energy $2 * E_{single}$ and the rupture length $2 * x_\beta$ [129].*

the bio-physical world by George I. Bell in 1978 [35]. In his phenomenological approach, Bell altered the Van't Hoff-Arrhenius equation, *Equation 2.2*, by including a mechanical energy, which resulted in a reduction of the activation energy threshold and highlighted the significance of mechanical forces to biological interactions. If $E_{mech} = f * x_\beta$ denotes the mechanical energy, where f is the external force and x_β is the displacement of the bond along the reaction coordinate, then *Equation 2.2* can be generalized. Bell's equation is shown in *Equation 2.3*

$$k = \nu_0 * \exp\left[-\beta\left(E_b - f * x_\beta\right)\right] \tag{2.3}$$

Bell associated the prefactor in the Van't Hoff-Arrhenius equation with the natural frequency of oscillation of atoms in solids. With this assumption it holds: $\nu_0 \approx 10^{13} s^{-1}$. In this sense, ν_0 can be seen as an attempt frequency to cross the energy barrier and escape from the potential well.

2.5.2 The Kramers-Bell-Evans Model

In SMFS the force can be applied to the molecular bond in two distinct ways. Either the force is reached instantaneously, at least on the time scale of bond dissociation, and held sufficiently long for the bond to dissociate, or the force is continuously rising with time. The former procedure is called a force clamp experiment [137]. The latter is the more commonly applied experimental method, as in most SMFS experiments, the bound molecules are separated at a constant pulling speed. In general, the molecular dissociation is an escape process, in which the interacting molecules escape from the potential well of the bound state to the energetically favorable dissociated state [138]. Hence, the bound state represents a metastable state, that is characterized by a local minimum of the energy landscape. Such an escape process is a stochastic process and the escape rate k can be related to the survival probability P_S to remain in the metastable state with *Equation 2.4* [139].

$$P_S\left(f\right) = \exp\left[-\int_0^f \frac{k\left(f'\right)}{\frac{df'}{dt}} df'\right] \tag{2.4}$$

The survival probability $P_S(f)$ allows calculation of the probability density function

(PDF), that describes the probability $p(f)$ of the bond to rupture at a particular force. The PDF is defined as the derivative of $P_S(f)$ with respect to f, shown in *Equation 2.5*

$$\begin{aligned} p\,(f) &= -\frac{dP_S(f)}{df} \\ &= \frac{k(f)}{\frac{df'}{dt}} P_S(f) \end{aligned} \tag{2.5}$$

In the Bell-Evans model, Evan Evans and Ken Ritchie associated the natural vibration frequency ν in Bell's equation, *Equation 2.3*, with the force-free dissociation rate k_0 [127]. With this assumption, $k(f)$ in *Equation 2.5* can be substituted by *Equation 2.3* and, if the PDF of the rupture forces is known, both k_0 and x_β can be determined.

The concept of studying molecular bonds by applying an external force was developed by Hermann Gaub and colleagues and Richard Colton and colleagues independently but at the same time [140, 141, 142]. Gaub et al and Colton et al investigated the interaction of biotin with avidin and streptavidin. The biotin-avidin and the biotin-streptavidin bonds are among the strongest non-covalent bonds, that have been reported. The group around Hermann Gaub used an SFM based approach to probe the adhesive force between an SFM tip functionalized with avidin, and biotinylated agarose beads. They discovered adhesive forces, that were up to a few hundred pN. After adding free avidin, the probability of detecting an adhesion event was reduced significantly, but this was not the case if free bovine serum albumin (BSA) was added. This lead to the conclusion, that the detected events were a direct result of the specific adhesion of biotin and avidin. The distribution of the adhesive forces was rather broad, but featured several distinct peaks. By using an autocorrelation analysis Gaub and colleagues revealed a force quantum of $F = 160 \pm 20pN$, which was attributed to the unbinding of a single biotin-avidin bond. In a similar approach, the group around Richard Colton measured the adhesive forces between a SFM tip functionalized with biotin and a mica surface coated with streptavidin. With this setup, they found adhesive forces of around $300pN$, whereas forces dropped to around $60pN$ after the mica surface had been blocked. A conceptual sketch of a typical force spectroscopy experiment is depicted in *Figure 2.9*.

The biotin-avidin and the biotin-streptavidin bonds have been the subject of many

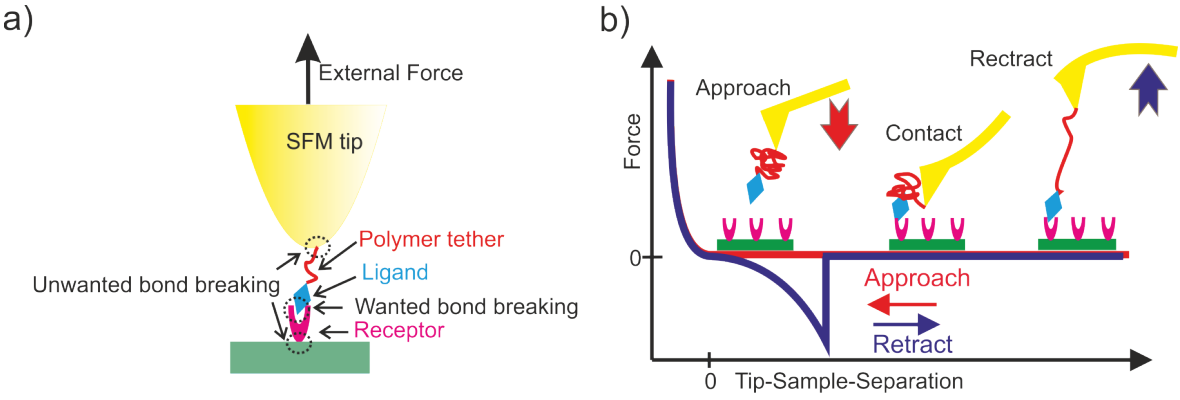

Figure 2.9 – ***Basic setup and typical force-separation curve:*** *A typical force-separation curve records the force that is deduced from the deflection of the cantilever using Hooke's law, at a given distance between the apex of the force probe and the sample. The measurement starts by approaching the force probe, with attached functional groups, towards the sample. During the approach no force is acting on the cantilever until the force probe makes contact with the sample and cantilever is bent, while the force probe is pushed on to the sample. When the force probe is retracted, the cantilever relaxes due to the diminishing force. If adhesive contact has been made, the cantilever is deflection in opposite direction during further retract. Specific interactions can be identified from the characteristic unfolding behavior of tethers between tip and functional group. Stable immobilization of samples on the surface as well as the tip is required in order to ensure that only the receptor-ligand bond is ruptured upon tip retraction.*

studies [143, 144, 145]. These investigations have revealed that the bond strength, that is, the most probable rupture force, is not an intrinsic property of the bonds. Rather, it is strongly influenced by the way the bond is loaded with the force [146]. In other word, the bond strength depends on how the force acting on the bond varies with time. The aspect of continuously increasing force was analytically treated by Evans Evans and colleagues [142, 128]. If the PDF of the rupture forces is known, the most probable rupture force f^* can be determined from $\frac{dp(f)}{df} = 0$. As a consequence, the dependence of f^* on the loading rate can be determined from *Equation 2.4* in combination with *Equation 2.5*. If one now assumes a constant rate of force loading, that is $\frac{df}{ft} = r$, and uses Bells formulation of Kramers' rate equation, *Equation 2.3*, then the famous Kramers-Bell-Evans (KBE) model is obtained. The fundamental equation of the (KBE)

model is given in *Equation 2.6*.

$$f^*(r) = \frac{k_B T}{x_\beta} ln\left(\frac{r x_\beta}{k_{off} k_B T}\right) \tag{2.6}$$

The KBE model states, that the bond strength depends on the loading rate according to $f^* \sim \ln(r)$. In order to obtain the kinetic parameters, that are characteristic of the bond, it is the established standard procedure to measure f^* for a broad range of loading rates. If f^* is then plotted against $\ln(r)$, the dissociation rate k_{off} and the distance to the transition state x_β can be determined from a linear regression fit. This procedure is typically termed dynamic force spectroscopy (DFS).

2.5.3 Friddle-Noy-De Yoreo Model

Over the last decades, DFS has been used to derive the kinetic characteristics of an enormous number of different molecular systems [147]. The KBE model has been most commonly used to interpret the spectra. Although the model has been very successful in characterizing the energy landscapes of many receptor-ligand systems, derivations from the linear dependence of f^* on $\ln(r)$ were found in many studies and the force spectra featured two or more distinct regimes. Most commonly, this succession of linear regimes was attributed to a cascade of energy barriers that are related to intermediate states of the intermolecular bond. Different attempts have been made to find an expression that describes force spectra over a wide range of loading rates [148, 149].

The widely accepted assumption of successive energy barriers was questioned by Raymond W. Friddle, Alexandr Noy and James J. De Yoreo, who doubted the existence of multiple barriers in unbinding reactions of small and simple molecules [147]. Unlike the thermal forces that induce the spontaneous dissociation of freely diffusing receptor-ligand pairs, the external force that induces forced dissociation is transmitted to the receptor-ligand pair via a force transducer [150]. In typical SFM based SMFS experiments the force transducer is the combination of the SFM cantilever and the polymeric tethers linking the receptor and ligands to the cantilever tip and the substrate. By relating the dissociated state with the potential induced by the force transducer that was used in the experimental setups they developed an extended model for DFS

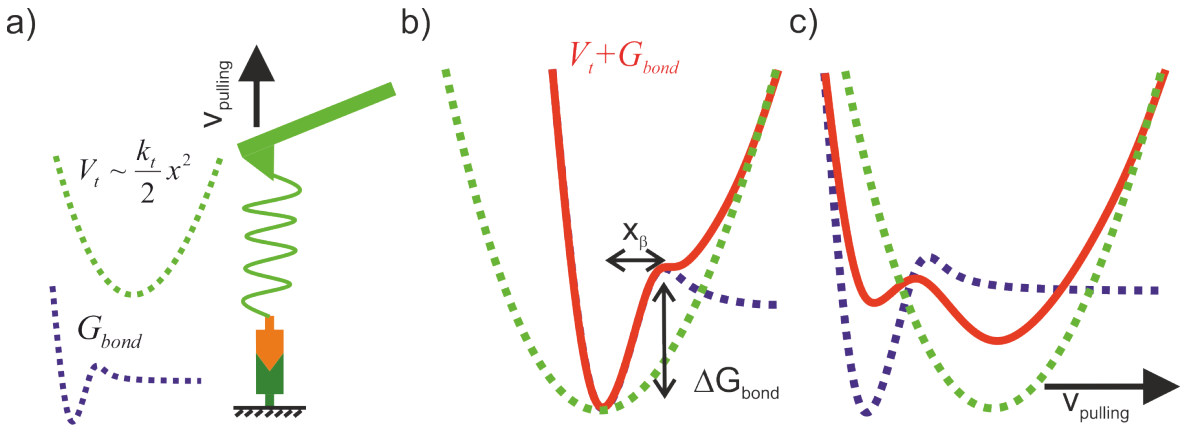

Figure 2.10 – ***Conceptual sketch of the energy landscape of an intermolecular bond under an external force:*** *a) In dynamic force spectroscopy an intermolecular bond is loaded with an external force by a force transducer that typically includes a force probe, such as a SFM cantilever, and a polymeric tether, such as polyethylene glycol. The energy landscape of the transducer V_t can be described with a harmonic potential that is characterized by the stiffness of the transducer k_t. The energy landscape of the bond V_{bond} is by the energy barrier ΔG_{bond} and the distance to the transitions state x_β, which is also referred to as the rupture length. b) V_t and V_{bond} overlap at zero force loading resulting in a deep potential well impeding dissociation. c) A second potential well is created when V_t is pulled beyond x_β. This second potential well is associated with the unbound state of the intermolecular bond.*

[150, 147, 151]. The basic concepts of the Friddle-Noy-De Yoreo (FNDY) model will be outlined in the following.

In this approach, Friddle and colleagues proposed, that the free energy as a function of the reaction coordinate, $G(x)$, of the bond between an immobilized receptor and a ligand, attached to the force probe can be written as the sum of the distant dependent energy of the free receptor-ligand bond, $G_{bond}(x)$, and the energy of the force transducer $V_t(x,t)$, as shown in *Equation 2.7*. The resulting energy landscape is illustrated in *Figure 2.10*.

$$G(x) = V_{bond}(x) + V_t(x,t) \tag{2.7}$$

It should be noted that the energy of the force transducer, $V(x,t)$, is time dependent

due to movement of the force transducer over time. The potential energy landscape of the unconfined intermolecular bond can be described, for example, by the Morse potential, which is given in *Equation 2.8* [152, 153].

$$U(x) = U_0 \left[1 - \exp\left(-2b(x/x_0 - 1)\right)\right]^2 \tag{2.8}$$

The Morse potential, which was originally derived as a solution of Schrödinger's equation for diatomic molecules, is well suited to describe the interaction between receptor-ligand pairs. The energy of the force transducer, that is separating the bond at a pulling speed $v_{pulling}$ over the time t, is described by the potential of the harmonic oscillator, which is given in *Equation 2.9*

$$V(x,t) = \frac{1}{2}k\left(x - vt\right)^2 \tag{2.9}$$

By combining the energy landscape of the bond and the transducer potential, the energy landscape of the receptor-ligand bond confined by the force transducer is obtained. The confinement hinders the spontaneous dissociation at zero force (*Figure 2.10 b)*). Hence, the receptor-ligand pair will remain trapped in the bound state for a quasi-infinite time, unless a certain threshold force f_{eq} is reached. f_{eq} is defined by *Equation 2.10.*

$$f_{eq} = \sqrt{2k\left(U_0 - T\Delta S\right)} = \sqrt{2k\Delta G} \tag{2.10}$$

Hereby, ΔG denotes the equilibrium free energy change between the bound and unbound state. This is a fundamental difference to the classic Bell-Evans model, which in principle describes the loading of the bond with a semi-harmonic potential of the transducer. It is convenient to define the minimum of $V(x,t)$ and the bound state of the free receptor-ligand pair to $x = 0$, $t = 0$. When the potential of the force transducer is shifted as a result of the transducer moving at the pulling speed v, a second metastable state is created (*Figure 2.10 c)*). The initially bound molecules can now dissociate by crossing the new energy barrier. The intermolecular bond is irreversibly broken when the external force exceeds the threshold force, i.d. $f >> f_{eq}$.

The forced bond rupture can be treated as a two-state process since the bond can either be connected or broken. Consequently, there exists a binding and an unbinding

transition rate. If these rates are subjected to the potential of the force transducer, they can be calculated from *Equation 2.12* and *Equation 2.11*

$$k_u\left(f\right) = k_u^0 \exp\left[\beta\left(fx_\beta - \frac{1}{2}k_t x_\beta^2\right)\right] \tag{2.11}$$

$$\begin{aligned} k_b\left(f\right) &= k_b^0 \exp\left[-\beta\frac{k_t}{2}\left(\frac{f}{k_t} - x_\beta\right)^2\right] \\ &= k_u\left(f\right)\exp\left[\beta\left(\Delta G_{bu} - \frac{f^2}{2k_t}\right)\right] \end{aligned} \tag{2.12}$$

Both rates cross at the equilibrium force f_{eq}, which was related to the free energy with *Equation 2.10*. With the rates that were defined in *Equation 2.12* and *Equation 2.11*, and assuming that the intra-well relaxation is faster than any time scale of the system, the two state Markov process can be written as shown in *Equation 2.13*. Hereby, p_{bound} denotes the probability of finding the system in the bound state and $p_{unbound}$ the probability of finding the system in the unbound state.

$$\frac{d}{dt}p_{bound} = -k_u(t)p_{bound} + k_b(t)p_{unbound} \tag{2.13}$$

The existence of f_{eq} inhibits the measurements of lower forces. Hence, *Equation 2.13* can be truncated and written in a simplified form.

$$\int_1^{p_{bound}} \frac{dp'_{bound}}{p'_{bound}} \cong -\frac{1}{r}\int_{f_{eq}}^{f} k_u(f')df' \tag{2.14}$$

With this, an expression for the dependence of the most probable rupture force on the loading rate can be derived. The result is shown in *Equation 2.15*.

$$f^* = f_{eq} + f_\beta e^{\frac{1}{R(f_{eq})}} E_{Int}\left(\frac{1}{R\left(f_{eq}\right)}\right) \tag{2.15}$$

$$R\left(f_{eq}\right) = \frac{r}{k_u\left(f_{eq}\right)f_\beta} \tag{2.16}$$

Hereby, the thermal force scale is set by $f_\beta = k_B T/x_\beta$, which is directly related to the transition state distance. The exponential integral $E_{Int}\left(z\right) = \int_z^\infty \frac{e^{-s}}{s}\,\mathrm{d}s$ satisfies the

analytical approximation $e^z E_{Int} \cong \ln(1 + e^{-\gamma}/z)$ with the Euler's constant $\gamma \approx 0.577$ and hence *Equation 2.15* can be analytically approximated by *Equation 2.17*.

$$f^*(r) = f_{eq} + f_\beta \ln\left(1 + \frac{e^{-\gamma} r}{k_u(f_{eq}) f_\beta}\right) \tag{2.17}$$

The equilibrium force f_{eq} defines the end of the equilibrium regime and the beginning of the kinetic regime. In their sublime paper, Friddle and colleagues illustrate that their model is well suited to fit many force spectra of preceding studies [147].

Chapter 3

Methods and Materials

In this chapter the experimental methods will be explained in detail and the materials used throughout this study will be introduced and elucidated.

3.1 Sample Preparation

This section will describe the immobilization of the viral proteins and virions as well as the functionalization of the SFM force probe with SA displaying ligands.

3.1.1 Surface Immobilization of the Viral Proteins Hemaglutnin and Neuraminidase

For this study hemagglutinin (HA) and neuraminidase (NA) of the influenza strain A/ California /04/2009pdm, as well as NA of the strain IAV X31 (H3N2), were immobilized onto a solid support using metal chelate complexation compounds that formed between nitrilotriacetic acid (NTA) and the terminal polyhistidine-tag (histag) that was fused to the viral proteins. The complexation was mediated by a Ni^{2+} ion.

The technique is based on immobilized metal affinity chromatography, which was introduced by Jerker Porath and colleagues, and is frequently used for protein immobilization [154, 155, 156, 157]. A conceptual sketch of the $histag - Ni^{2+} - NTA$ complex is shown in *Figure 3.1.* It was also shown that the histag serves well as a handle to hold and stretch proteins [158].

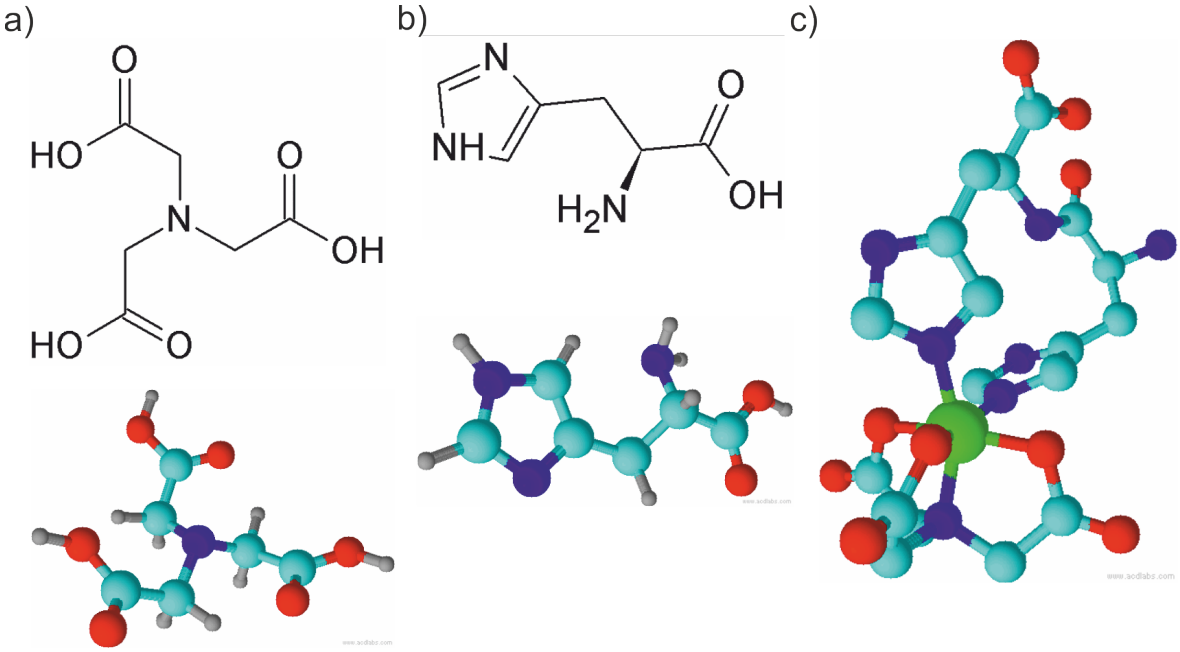

Figure 3.1 – ***Immobilization of a polyhistidine-tag through complexation with a*** **Ni^{2+} – NTA** ***chelate:*** *a) shows NTA. b) shows histidine. In both a) and b) the top image shows the chemical structure, and the bottom image shows the structure with color coding. c) shows the complex that is formed between a histag consisting of 2 histidine and NTA that is loaded with a Ni^2+ ion (shown in green). Two histidines can bind simultaneously to one NTA molecule. The hydrogen atoms are not shown for the sake of clarity. The image was made using ChemSketch (ACDLabs Freeware 2015).*

The H1 hemagglutinin (HA (H1N1)) was obtained from BEI resources (NIAID, NIH) (H1 Hemagglutinin (HA) Protein with C-Terminal Histidine Tag from Influenza Virus, A/ California /04/2009 (H1N1)pdm09, recombinant from Baculovirus, NR-15749). The amino acid sequence of the recombinant HA (H1N1) includes a poly-histidine tag at the C-terminus. This histag consists of 8 histidine residues. The HA was received in PBS, at $pH = 7.4$, with 50% glycerol at a concentration of $c_{HA} = 1mg/ml$ and used as received. Neuraminidase of the type H1N1 (NA H1N1)) and neuraminidase of the type H3N2 (NA (H3N2)) were obtained from Sinobiological (Beijing, China). The lyophilized NA were also recombinant and expressed with a N-terminal histag of 6 histidine residues. Following manufacturer's instructions, the NA were dissolved in Milli-Q water to a final concentration of $c_{NA} = 0.25mg/ml$.

The chelating agent nitrilotriacetic acid (NTA), covalently bound to glass slides, was

purchased from NanoCS Inc (New York, USA). Prior to incubation with proteins, the slides were cut to squares with a size of $1 * 1cm^2$ using a diamond stylus and thoroughly washed with Milli-Q water to remove dust and other macroscopic contamination. The NTA-functionalized slides were loaded with Ni^{2+} ions by covering the surface with a $10mM$ solution $NiCl$ for 2 hours. After loading, the slides were rinsed with Milli-Q water and remaining water was removed using paper towels. The Ni^{2+} loaded slides were incubated with either HA or NA for 1 hour by dropcasting the protein solution onto the NTA-surface. Unbound or unspecifically bound proteins were removed by washing the slides with PBS buffer solution.

3.1.2 Surface Immobilization of Influenza Virions

The influenza virions were immobilized on a self-assembled monolayer (SAM) on gold surfaces by Jose Luis Cuellar-Camacho during a collaboration. The details of the immobilization procedure, which was adopted from a protocol by Friedsam and colleagues [159], will be published in an upcoming manuscript but the main steps will be outlined here for the sake of completeness.

Purified X31 virus (influenza strain A/Aichi/2/68 H3N2, reassorted with internal segments of A/PuertoRico/8/1934 H1N1) was received in PBS buffer solution at a protein concentration of $4.4mg/ml$. Epitaxial gold 111 layer on mica (Georg Albert PVD, Heidelberg, Germany) were cleaned with an aqueous solution of ammonia (30%) and hydrogen peroxide (30%) followed by rinsing with Milli-Q water. The SAM was created by immersion of the gold-mica plate in an ethanol solution containing $2.5mg$ 16-mercaptohexadecanoic acid and $2mg$ 11-mecaptoundecanol immediately after cleaning. The SAM was activated using a solution of MES buffer (pH=6) with a 1:5 mixture of N-Hydroxysuccinimide and 1-Ethyl-3-(3-dimethylaminopropyl) carbodimide. After activation, the gold-mica plates were rinsed with MES buffer and immediately incubated with $10\mu l$ virus solution for one hour. The plates were rinsed with PBS buffer prior to experiments in order to remove unbound material.

3.1.3 Functionalization of the SFM Force Probe

Synthesis of the Sialic Acid Displaying Ligands and the Control Molecule

The measurements of the interaction forces between SA and the viral proteins HA and NA required not only sialic acid displaying ligands but also control molecule, designated to test the specificity of the interaction. All molecules were custom made and designed to meet the needs of single molecule force spectroscopy. The synthesis was carried out by Ph.D. Sumati Bhatia (Freie Universität Berlin, Organic Chemistry). The details of the synthesis are described elsewhere [160] but a brief description will be given for the sake of completeness. The control molecule was created by linking a hydroxide (OH) terminated polyethylene glycol tether (PEG) to a lipoic acid group and was called 'OHPEGLA'. The molar weight of the PEG tether was $5kDa$, which can be related to a contour length of about $40nm$. It was assumed that the terminating OH endgroup is not interacting specifically, if at all, with the viral proteins HA and NA. Its structure is depicted in *Figure 3.2 a)*. The SA displaying ligand, which was called 'SAPEGLA', was created using the same PEG tether that was used for the control molecule. The lipoic acid was attached to one end while the other end was terminated with SA, as illustrated in *Figure 3.2 b)*. In a similar fashion, the dendritic ligand, which was called dPGSA, was synthesized and linked to the PEG tether. Its structure is depicted in *Figure 3.2 c)*. A detailed description of the synthesis of the dendritic polyglycerol and its functionalization with SA can be found in the literature [22]. The amount of SA moieties was set to 15%. Bhatia and colleagues had shown that this concentration resulted in the maximum inhibitory effect [22]. In order to construct a corresponding control molecule, the dendritic polyglycerol was directly linked to the PEG tether without functionalization with SA.

Covalent Attachment of the Molecules to the Force Probe

Both of the hetero-functional SA displaying ligands, SAPEGLA and dPGSA, and the control molecules could be self-assembled on gold surfaces via the sulfur groups on the lipoic acid. The flexible PEG tether would then give the necessary freedom of motion for the terminal SA-group to find proper binding partners.

For all SMFS experiments force probes of the type OBL (Bruker Corporation) were used. These probes feature a low spring constant $k_c \approx 30mN/m$ that ensures the high deflection to force ratio needed to detect the small forces of bio-molecular interactions. The force probes are gold coated and therefore functionalization is straight forward. The force probes were illuminated with UV light for $30min$, using a low pressure mercury lamp. The ozone created by the UV radiation is known to clean surfaces from organic contamination. After UV treatment the probes were placed on a piece of Parafilm and covered with a droplet of solution containing either the ligand or the control molecule in Milli-Q water. Probes were incubated for $12h - 24h$ to ensure a dense surface coating. After the incubation, unspecifically bound molecules were removed from the force probes by gently dipping the force probe into Milli-Q water.

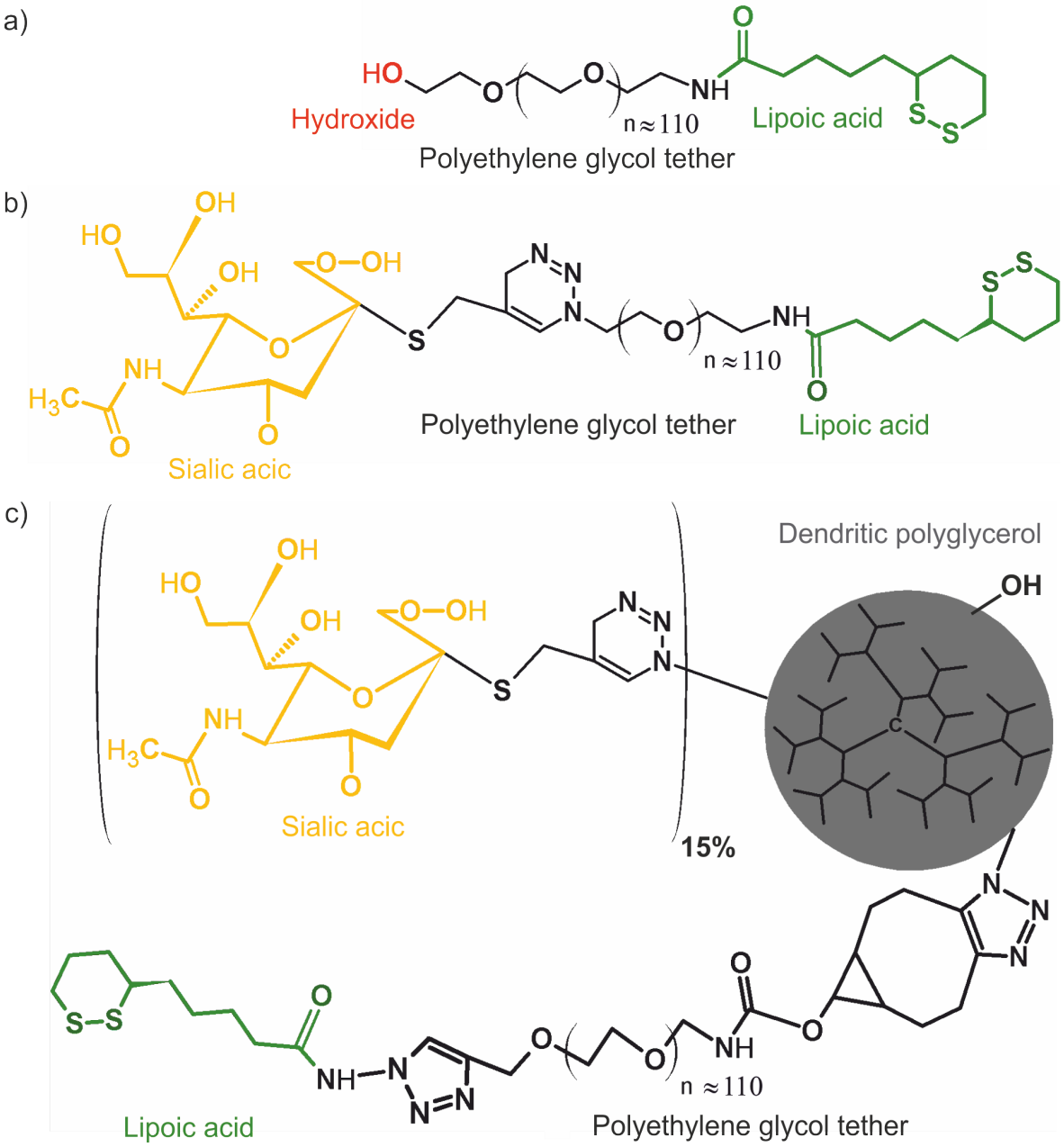

Figure 3.2 – ***SA displaying ligands and the control molecule:*** *All structures are composed of lipoic acid for the attachment to the force probe, a polyethylene glycol tether for identification of binding events and the terminal moiety. a) The hydroxide (OH) terminated control molecule (OHPEGLA) will not bind specifically to HA nor NA. b) The SA displaying ligand (SAPEGLA) will bind specifically to single binding pockets on HA and NA. c) The dendritic ligand (dPGSA) displays multiple SA (surface functionalization is 15 %). It is expected to bond multivalently, at least to HA. The image was made using ChemSketch (ACDLabs Freeware 2015).*

3.2 Experimental

Firstly, this section will outline the imaging by SFM. Secondly, the procedure to measure molecular forces is described.

3.2.1 Scanning Force Microscope Imaging

SFM images were taken using commercial SFM instruments, namely a Multimode 8 from Bruker Corporation and a Nanowizard 3 from JPK Instruments. For imaging at lower lateral resolution, Sharp Nitride Lever (SNL) probes from Bruker were used. These probes feature a sharp silicon tip on a flexible silicon nitride cantilever. The nominal tip radius is 2 nm but variations up to 12 nm are possible. In order to achieve a higher lateral resolution, probes of the type PEAK-FORCE HIRS were used. These probes have tips with a nominal radius of 1 nm and a maximum radius of 2 nm. All probes were used as received without further treatment or modifications. Images were recorded in force spectroscopy mode at a typical resolution of 256*256 pixels/image or 512*512 pixels/image. Image sizes varied from $10 * 10\mu m^2$ to $0.5 * 0.5\mu m^2$. In force spectroscopy mode a force separation curve is recorded for every point of the image. These force separation curves feature an approach of the SFM force probe towards the sample surface and a retract of the SFM force probe from the sample surface. During the approach and retraction, the deflection signal of the cantilever at the given height of the force probe is measured. The deflection signal is also a measure for the force acting on the SFM force probe. The topography of the sample surface was determined from the SFM probe height at a given deflection setpoint during the approach. This setpoint was $100pN - 200pN$. The vertical distance of the force probe movement was set to $50nm - 150nm$. The images were post processed using the software Nanoscope Analysis (Bruker Corporation) and JPK Data Processing (JPK Instruments). The images were line-wise flattened using a polynomial fit of $2nd$ order. All images were taken in PBS buffer solution, if not stated otherwise.

3.2.2 Single Molecule Force Spectroscopy

Single molecule force spectroscopy was done on a Force Robot 300 with motorized precision stage by JPK Instruments (Berlin, Germany). Force-separation curves were measured by approaching the functionalized SFM force probe towards the sample surface at a constant speed of $v_a = 0.5\mu m/s$. The approach was stopped when the deflection signal reached the given setpoint force $F_{SP} = 100pN$. Then, the force probe was either retracted immediately or allowed to rest on the surface over contact times up to $10s$, with the setpoint force maintained. An increased contact time is supposed to increase the likelihood that a ligand bound to the SFM force probe will interact with a protein immobilized on the Ni^{2+}-NTA surface. After contact, the force probe was retracted. The retraction speed v_r was varied between $0.1\mu m/s$ and $10\mu m/s$ in discrete steps: $v_r = [0.1, 0.3, 0.5, 1.0, 2.0, 5.0, 10]\mu m/s$. On retract binding forces could be measured, if a ligand attached to the tip of the force probe had formed a bond with either the surface or the proteins immobilized on the surface. In addition, there exists the possibility of an interaction of the tip of the force probe with the surface or proteins on the surface. The unspecific interactions of the tip could be distinguished from the interactions of the ligand by considering the behavior of the PEG tether of the ligand. In the case of a ligand interacting with the surface, the force applied to the molecular bond does not increase linearly with the distance of the force probe to the surface, following Hooke's law, but rather is distributed over the PEG tether. The PEG tether is stretched before bond rupture, resulting in a non-linear increase of the interaction force due to the entropic unfolding of the PEG tether. As a consequence, only those rupture events were considered for further analysis that displayed a non-linear increase of the interaction force and bond rupture within the contour length of the PEG tether, which is $l_c^{PEG} = 40nm$.

The non-linear force peaks, which are identified as interactions of the ligands, were fitted with a polymer chain model, in order to extract the unbinding forces. Namely the freely jointed chain (FJC) model (Equation 3.1) and the extensible freely jointed chain model (Equation 3.2) were used. These models provide a mathematical description of the extension of a polymer chain, such as PEG, under an externally applied force.

While the FJC model allows the polymer to be stretched to maximum length l_{max} that is equal to its contour length l_c, yielding $l_{max} = l_c$, the extensible FJC model includes stretching of the backbone of the polymer and therefore allows $l_{max} > l_c$. The equations corresponding to the particular model can be found in literature [161].

$$l(F) = l_c \left[\coth\left(\frac{F l_K}{k_B T}\right) - \frac{k_B T}{F l_K} \right] \tag{3.1}$$

$$l(F) = l_c \left[\coth\left(\frac{F l_K}{k_B T}\right) - \frac{k_B T}{F l_K} \right] \left(1 + \frac{F}{\kappa l_c}\right) \tag{3.2}$$

Fitting these equations to the force separation curves yielded not only the rupture force, but also the rate of force loading at bond rupture, which is also called the critical loading rate r_{crit}. In general, the force loading rate r at a given force F is defined as the change in force F in relation to the change in tip-sample separation x_{tss} according to *Equation 3.3*

$$r\big(F\left(x_{tss}\right)\big) = \frac{\partial F\left(x_{tss}\right)}{\partial x_{tss}} v_{pulling} \tag{3.3}$$

with the pulling speed $v_{pulling}$. As a consequence of the bond rupturing at the critical tip-sample separation x_{crit} the critical loading rate is calculated from 3.4

$$r_{crit} = \left.\frac{\partial F\left(x_{tss}\right)}{\partial x_{tss}}\right|_{x_{crit}} v_{pulling} \tag{3.4}$$

Unlike the simple approach using the apparent loading rate $r_{app} = k_{probe} * v_{pulling}$ with k_{probe} being the spring constant of the force probe, the critical loading rate accounts for the combined elasticity of the force probe and the PEG tether. The critical loading rate can be interpreted as the apparent loading rate using an effective spring constant k_t. The effective spring constant stands for the elasticity of the whole transducer system.

The rupture of a single molecular bond, such as the detachment of a sialic acid from the binding pocket of a viral protein, does not, at first, reveal relevant information of the molecular interactions, since these are subjected to their stochastic nature. Therefore, in order gain insight into the physics of the bond rupture, the distribution of rupture forces needs to be determined. Up to several hundred force-separation curves displaying

a characteristic rupture event were recorded to acquire the appropriate amount of data. This was achieved by moving the force probe over the surface in discrete steps between two successive force-separation curves. The discrete steps were preset by defining a lattice of $10 * 10$ points over an area of $10\mu m * 10\mu m$. It is assumed that the viral proteins are disturbed when the force probe makes contact with the surface, especially regarding their tertiary structure. Also, proteins might stick to the tip of the force probe, so that they are unfolded upon retraction. These unfolded proteins are not likely to reshape into their original form and will therefore most likely not interact as intact proteins. This might cause unspecific rupture events. To minimize these, only one force-separation curve was recorded per lattice point. The distance of $1\mu m$ between points ensures that almost every contact of the force probe will be on unharmed surface areas. The rupture forces with their corresponding critical loading rates could be displayed in either a scatter plot, where each point represents a single rupture event or they were summarized to histograms for every individual pulling speed. From these histograms the most probable rupture forces, and respectively the most probable critical loading rates, were obtained by fitting the histograms with Gaussian functions.

As previously mentioned, the experimental technique ensures that only rupture events caused by interactions of the ligand with the surface or with proteins on the surface are considered in the analysis. This is achieved by including the PEG tether to indicate specific interactions. The drawback of SMFS is that the interaction of the ligand with the plain surface cannot be discriminated from its interaction with the protein. In both cases, the PEG tether will be stretched during retraction of the force probe, resulting in the characteristic non-linear signal. To exclude the possibility that the measurements are blurred by unspecific ligand-surface interactions, leading to false conclusions, additional control experiments need to be performed. These control experiments follow the logic of competitive binding assays of which the concept is sketched in *Figure 3.3*.

First, the probability of binding p_b of the ligand was compared to the probability of binding of the OH terminated control molecule. Secondly, p_b of the ligand was probed on the surface, where viral proteins had been immobilized, and it was compared to p_b of the ligand probed on a surface without viral proteins. Finally, the p_b of the ligand to

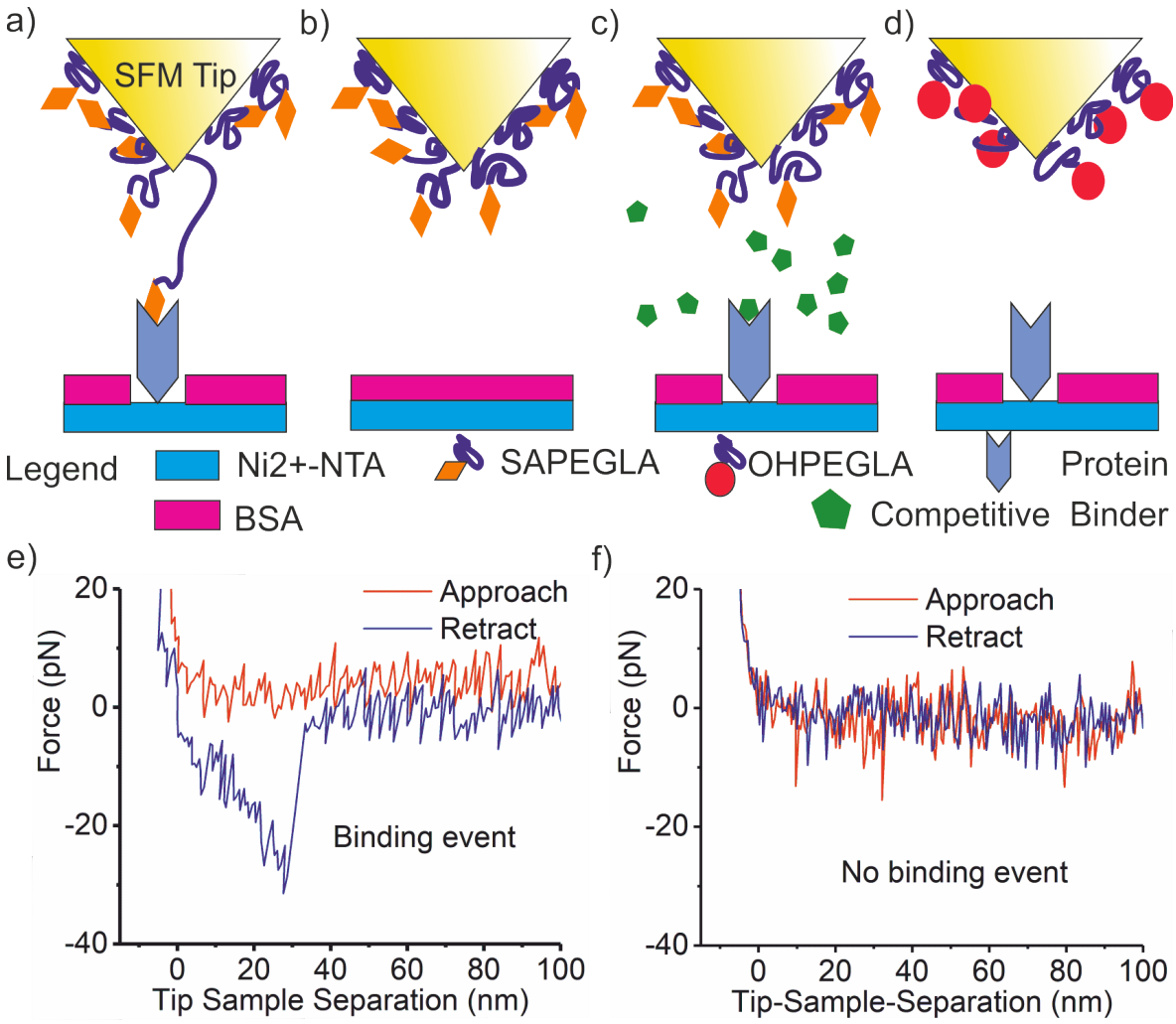

Figure 3.3 – ***Schematics of experimental setups to test the specificity of the observed interactions and characteristic force-separation curves:*** *a) SAPEGLA binds to one of the influenza proteins that were immobilized on the surface. Upon retraction of the SFM tip a high p_b to record a characteristic rupture event is expected. b) Without any influenza proteins immobilized on the support, the ligand is not supposed to bind to the support and a diminishing p_b is expected. c) If competitive binders, which block the binding pocket of the proteins are introduced to the setup, binding will be suppress and p_b will be reduced. d) An alternative, OH displaying ligand is assumed to show no specific adhesion to the influenza proteins. e) and f) A force-separation curves either show (e)) binding events or not (f)).*

surface immobilized viral proteins was determined in the presence of, or after incubation of the surface with, alternative binders. Free sialic acid and oseltamivir were used as the alternative binders.

Chapter 4

Results and Discussion

This chapter will present the experimentally obtained results and discuss their physical origins and biological implications with regard to multivalent protein-ligand interactions. It is organized as follows: The first section will focus on the immobilization and the visualization of the viral proteins HA and NA on solid supports, using the technique of metal-chelate complexes and SFM imaging. In this section, SFM images of surface immobilized proteins obtained in buffer solution will be shown. Surface characteristics, such as homogeneity of the coating and density of proteins, will be analyzed. Additionally, influenza virions will be detected on self-assembled monolayers and their distributions over the surface will be revealed. In *section 4.2* the results obtained using SMFS will be presented. The rupture forces will be shown that were measured for the interaction of the SA terminated ligand SAPEGLA with hemagglutinin and neuraminidase of the type H1N1 and their dependence on the applied rate of force loading will be discussed in the framework of the KBE model and the more recent FDYN model. The analysis will reveal that the determination of the kinetic parameters of sophisticated biomolecular interactions requires knowledge of the full DFS over a broad range of loading rates. In addition to kinetic and energetic parameters that can be derived from the DFS, the association of protein-ligand complexes will be illustrated with respect to determination of chemically relevant equilibrium parameter, i.e. the dissociation constant. The multivalent aspects of intermolecular bonds will be illuminated in section 4.3. Firstly, the simultaneous dissociation of multiple SAPEGLA bonds is analyzed. Secondly, the kinetics of the dendritic ligand dPGSA will exemplify

truly multivalent enhancement of binding strength. Finally, the biological implications of kinetic and energetic parameters of the protein-ligand interaction will be discussed with regard to viral transmissibility and infectivity.

4.1 Immobilization and Imaging Using SFM of Viral Proteins and Virions

4.1.1 The Viral Proteins HA and NA

Self-assembly is a reliable tool to generate surfaces with desirable functionality. The high affinity between certain chemical moieties promotes the stable attachment of sample molecules in a defined orientation, which is convenient for SMFS. Throughout this study, the viral proteins HA and NA were immobilized on glass surfaces. This was achieved by forming a metal-chelate complex between nitrilotriacetic acid (NTA), which was linked to the glass surface, and a poly-histidine tag, that had been included into the sequences of the proteins. This section will now demonstrate the effectiveness of the method of immobilization.

SFM imaging was used to characterize the glass surfaces both prior to and after incubation with HA or NA. In order to precisely characterize the structure and orientation of the proteins, the topography of the NTA-coated glass surface (NTA-GS) was analyzed prior to incubation with proteins. This was necessary, since the clean uncoated surface needs to be known in order to differentiate between the immobilized proteins and the background. A characteristic image of the NTA-coated glass surface is shown in *Figure 4.1 a)*.

The image has a lateral size of $5 * 5\mu m^2$ and reveals a surface that is smooth over large areas, but also displays multiple protrusions of indistinctive shape, size and height. These irregular protrusions were present on all analyzed NTA-GS, even when slides from several different batches were tested. It was concluded that these inhomogeneities were caused during the production. In addition, they could not be removed, by subsequent rinsing of the glass slides with PBS buffer. In order to prevent further contamination or degradation of the surfaces, more aggressive cleaning agents or procedures were not

used.

As expected, the surface topography changes significantly after incubation of the NTA-GS with the viral proteins HA and NA of the influenza strain A/ California /04/2009pdm (H1N1). A contrasting juxtaposition of the three different types of samples is shown in *Figure 4.1.* The scan size is also $5 * 5\mu m^2$ in the images showing NA (H1N1) (*Figure 4.1 c)*) and HA (H1N1) (*Figure 4.1 e)*). The figure illustrates that incubation of the NTA-GS with the viral proteins results in attachments between the viral proteins and NTA that are sufficiently stable to withstand rinsing and the forces that occur during scanning. In *Figure 4.1 b), d), f)* an overlap of three profiles for each surface topography is shown. The profiles clearly demonstrate the increase in surface roughness as a result of protein immobilization. The profiles also indicate that the height of HA (H1N1) on the surface, $h_{HA(H1N1)} \approx 12nm$, is greater than that of NA (H1N1), with $h_{NA(H1N1)} \approx 7nm$. Even though the NA (H1N1) - coated NTA-GS, which is shown in *Figure 4.1 c)*, and the HA (H1N1) - coated NTA-GS, which is shown in *Figure 4.1 e)*, are similar in that their surface topographies are higher compared to the uncoated NTA-GS, they differ in the way the viral proteins arrange on the surface. While the NA is distributed in rather homogeneously over the surface, the HA builds up aggregates. Nevertheless, the images provide good evidence that the viral proteins can be immobilized on the NTA-GS. Since it has now been demonstrated that the technique of metal-chelate complexes is well suited to immobilize his-tagged proteins, the coating of NTA-GS with HA (H1N1), or respectively NA (H1N1), will be further analyzed. This intends to provide a deeper understanding of the surface properties, such as protein density.

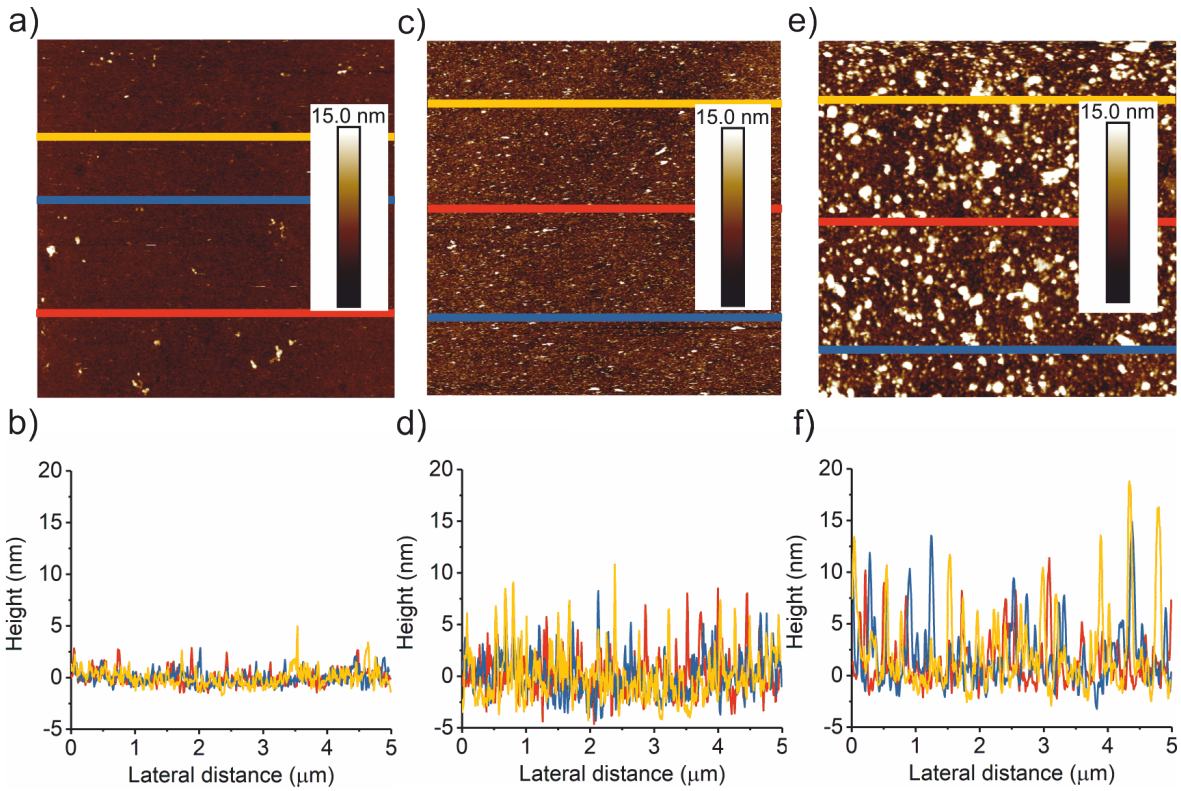

Figure 4.1 – ***SFM images of the NTA surface before and after incubation with NA and HA of the type H1N1:*** *All images were taken with a Multimode 8, using a tip of the type SNL. The size of the images is* $5 * 5\mu m^2$. *Colored lines indicate positions of the profiles shown below each image. a) The NTA surface is rather smooth. b) Three profiles taken from the NTA surface. c) After incubation with NA (H1N1) the surface is covered with small particles with a height of* $\approx 6 - 8nm$. *d) Three profiles taken from the NA (H1N1) covered surface. e) After incubation with HA (H1N1) the surface is covered with small particles with a height of* $\approx 10 - 20nm$. *f) Three profiles taken from the HA (H1N1) covered surface.*

Hemagglutinin of the type A/California/04/2009pdm (H1N1)

As mentioned in *chapter 3*, cantilevers with ultra-sharp tips designed for high resolution SFM were used for detailed imaging of the viral proteins. A representative SFM image displaying the topography of NTA-GS coated with HA (H1N1) is shown in *Figure 4.2*.

The size of the image in *Figure 4.2 a)* is $3 * 3\mu m^2$ and the color scale represents a height between $0 - 13nm$. It clearly shows that the surface is fully covered with proteins. The proteins show up as small dots that are distributed over the surface. Even though some aggregates, especially in the upper right corner of the image, are visible, most of the proteins have similar shape and size. A more detailed view is given in *Figure: 4.2 b)*. The size of the image is $1 * 1\mu m^2$ and the color scale represents a height between $0 - 10.2nm$. It can clearly be seen that the HA (H1N1) attach individually to the surface and are uniformly spaced. *Figure 4.2 b)* shows that the NTA-GS surface is not completely packed with proteins. Instead, the individual proteins are separated from another by distance of roughly $30nm$. This enables the tip of the SFM cantilever to scan not only the topographical features given by the head domains of the HA (H1N1), but also to reach the NTA-GS surface between two neighboring proteins and therefore to probe the actual height of HA (H1N1). A small scale image of HA (H1N1) is given in *Figure 4.2 c)* together with the profiles of six randomly selected individual HA (H1N1). The image shows that HA (H1N1) appear as particles of similar shape and size. HA (H1N1) of which the profiles were taken are marked with colored circles. The profiles were measured across the maximum of the particle and the concatenated data of all profiles was fitted with a Gaussian fit. For a better illustration, the profiles and the plot of the fit function were horizontally offset so that the peak of the fit function is at a lateral distance of $0nm$. The Gaussian fit returns a height of $h_{HA(H1N1)} = 13.5 \pm 0.2nm$ (error accounts for standard error) and a standard deviation of $\sigma_{HA(H1N1)} = \pm 10nm$. The height corresponds well to literature values [162], as was illustrated in *chapter 2*. This is good evidence that the HA (H1N1) are immobilized in an upright orientation.

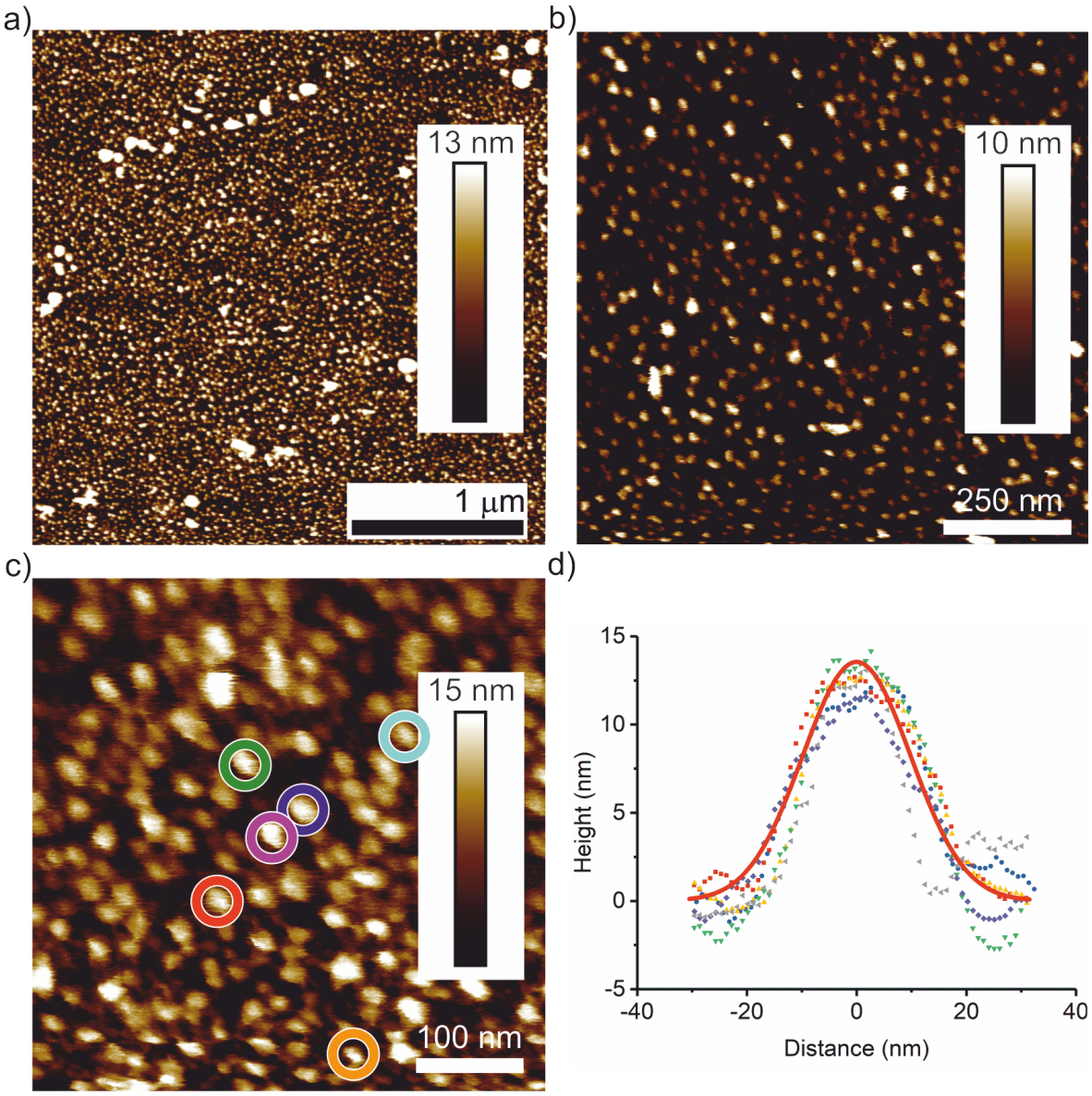

Figure 4.2 – ***SFM images of HA (H1N1) immobilized on NTA surface and corresponding topography profiles:*** *a) The image with a scan size of* $3 * 3\mu m^2$ *shows that the NTA surface is densely covered with HA (H1N1). b) The image with a scan size of* $1 * 1\mu m^2$ *shows that HA (H1N1) is distributed homogeneously. Surface density is* $\approx 1 * 10^3 \mu m^{-2}$*. c) A high resolution SFM image with a size of* $0.5 * 0.5\mu m^2$ *is shown. The image was taken with a Multimode 8 (Bruker) using an ultra sharp tip of the type PEAKFORCE-HIRS A. Six individual HA (H1N1) are highlighted by colored circles. d) The topographic profiles of the HA (H1N1) highlighted in c) are shown as scatter plots. The solid red line represents the best fit to the concatenated data by a Gaussian function.*

Neuraminidase of the type A/California/04/2009 (H1N1)

In the same way the HA (H1N1) was identified on the NTA-GS, the immobilization of the NA (H1N1) will now be analyzed. In order to achieve a better resolution and reduce the impact of tip artifacts, the ultra-sharp cantilevers were used, as previously described. A characteristic image of the surface topography after incubation with NA (H1N1) is shown in *Figure 4.3 a)*.

The size of the image is $5 * 5\mu m^2$ and the color scale from black to white represents a height of $0 - 15nm$. Similar to the previously described immobilized HA (H1N1), the NA (H1N1) seems to adhere to the NTA-GS well, but it also forms aggregates of various shapes and sizes on the surface. Nevertheless, on several regions of the image a homogeneous coating with particles of similar shape and size can be seen. An image, typical for these areas is shown in *Figure 4.3 b)*. The size of the image is $1 * 1\mu m^2$ and the color scale from black to white represents $15nm$. The appearance of the homogeneously shaped and distributed particles is a good indication that single NA (H1N1) were immobilized. In order to analyze the shape and size distribution of the immobilized NA (H1N1) further, SFM images were taken at a smaller scale. Such an image is shown in *Figure 4.3 c)*. The size of the image is $0.5 * 0.5\mu m^2$ and the color scale represents a height of $10nm$. It can clearly be seen that the individual NA (H1N1) are homogeneously shaped and separated from another. In *Figure 4.3 d)* the profiles of six randomly selected NA (H1N1) are shown as colored dots. The NA (H1N1) of which the profiles were taken are color coded in the SFM image. The profiles overlap well, supporting the assumption that particles of the same type were immobilized. The concatenated date of all profiles were fit with a Gaussian function. The fit returned a height of $h_{NA(H1N1)} = 5.8 \pm 0.3$ (error accounts for standard error) and a standard deviation of $\sigma_{NA(H1N1)} = 2.9$. The value of the height corresponds well to those reported in literature. Therefore, it is concluded that NA (H1N1) were immobilized on NTA-GS in an upright orientation.

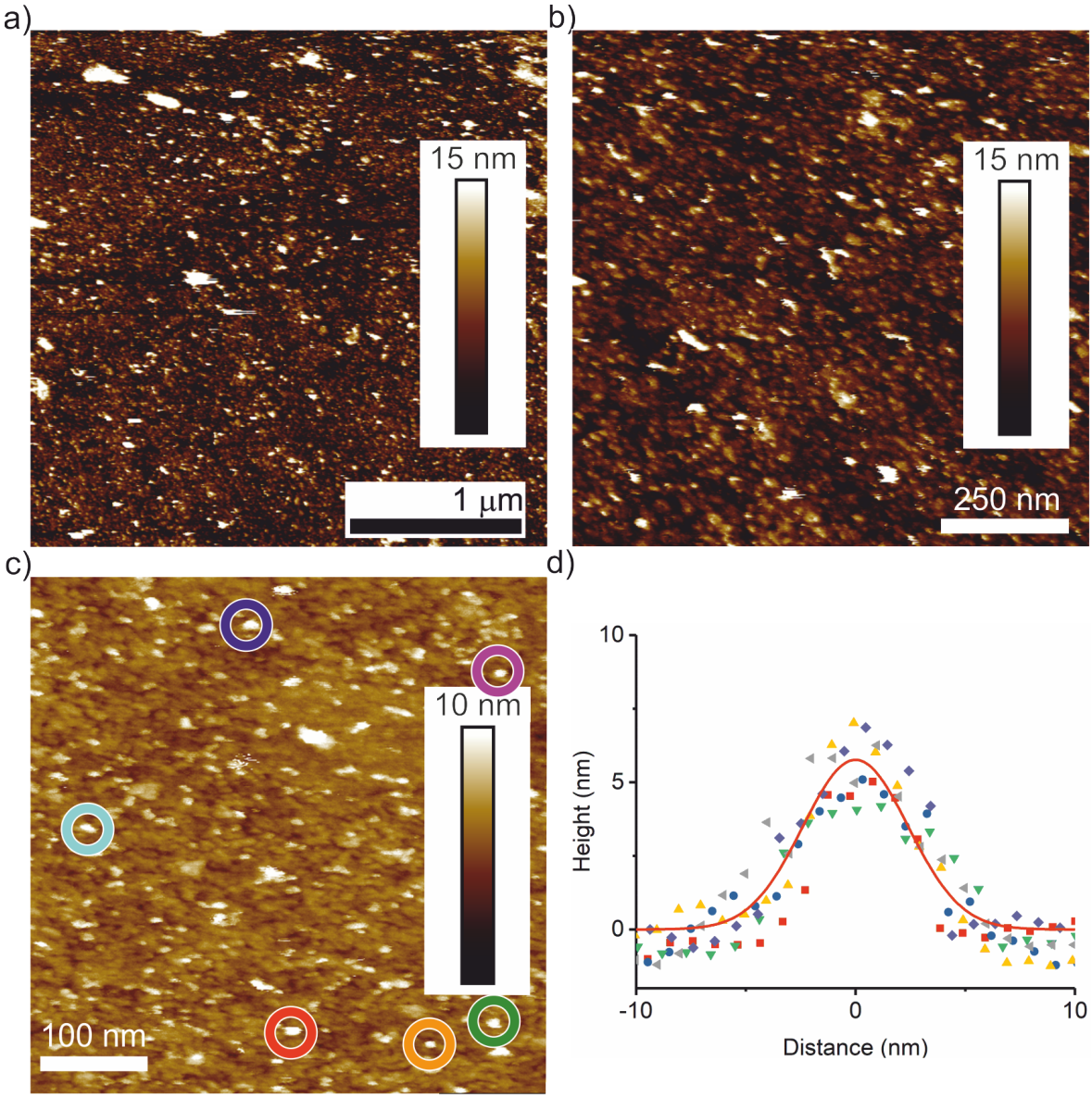

Figure 4.3 – ***SFM images of NA (H1N1) immobilized on NTA surface and corresponding topography profiles:*** *a) The image with a scan size of* $3 * 3\mu m^2$ *shows that the NTA surface is densely covered with NA (H1N1). b) The image with a scan size of* $1 * 1\mu m^2$ *shows that NA (H1N1) is distributed homogeneously. Surface density is* $\approx 1 * 10^3 \mu m^{-2}$*. c) A high resolution SFM image with a size of* $0.5 * 0.5\mu m^2$ *is shown. The image was taken with a Multimode 8 (Bruker) using an ultra sharp tip of the type PEAKFORCE-HIRS A. Six individual NA (H1N1) are highlighted by colored circles. d) The topographic profiles of the HA (H1N1) highlighted in c) are shown as scatter plots. The solid red line represents the best fit to the concatenated data by a Gaussian function.*

In order to give further proof that HA (H1N1) and NA (H1N1) were immobilized in the desired orientation, i.e. upright with the active head domain accessible for molecular interaction, the height and width of ~ 100 HA (H1N1) and NA (H1N1) were measured. The measured values were binned into histograms, that are depicted in *Figure 4.4*.

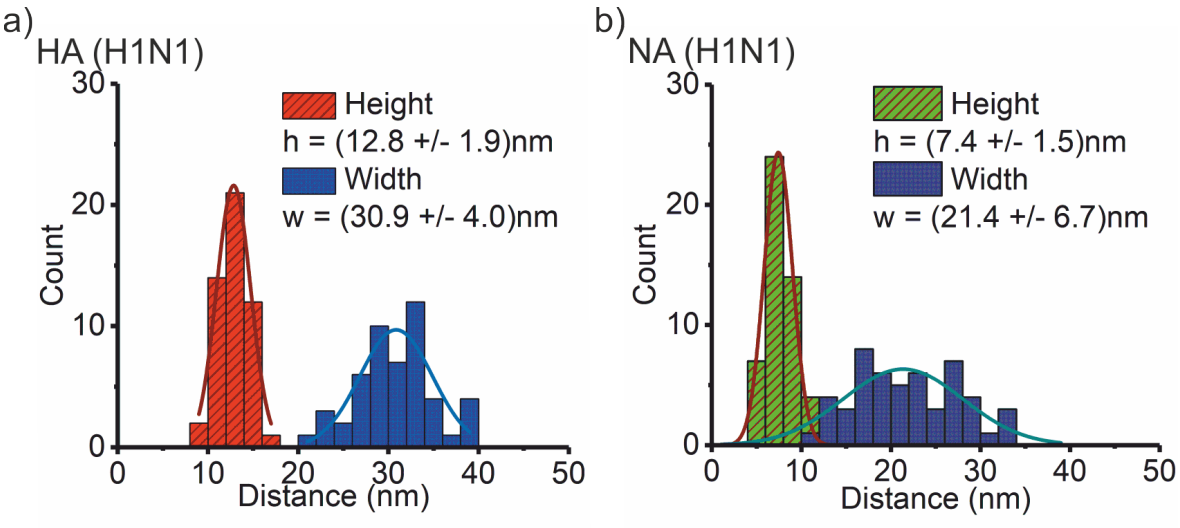

Figure 4.4 – ***Histograms showing the distributions of height and width for HA and NA respectively:*** *a) The figure shows the distribution of the height and width of HA (H1N1) proteins. The distributions were determined from the analysis of 50 individual, randomly selected proteins. b) The figure shows the distribution of the height and width of NA (H1N1) proteins. The distributions were determined from the analysis of 51 individual, randomly selected proteins.*

Fitting the histograms with Gaussian functions returned for HA (H1N1) a height of $h_{HA(H1N1)} = 12.8 \pm 1.9nm$ and a width of $w_{HA(H1N1)} = 30.9 \pm 4.0nm$, while the height of NA (H1N1) was $h_{NA(H1N1)} = 7.4 \pm 1.5$ and the width was $w_{NA(H1N1)} = 21.4 \pm 6.7nm$. The height of HA (H1N1) and NA (H1N1) corresponds well to values reported in literature. However, this does not apply to the width of either of the two proteins. Typical values of the width of HA (H1N1) are expected around $\sim 4nm$. For NA (H1N1), a width of $\sim 5nm$ is expected. This deviation by a factor of $5 - 6$ can be explained is, for one, caused by the typical broadening of lateral features by the tip of the SFM probe. Since the geometry of the tip is known, the effect of tip broadening can be calculated and the true width of the immobilized proteins can be approximated. From

Table 4.1 – ***Measured and calculated values of the height and width of HA and NA:*** *The measured values were obtained from the histograms shown in Figure 4.4. These values were corrected by including the effect of tip broadening.*

Protein	$h_{measured}$ nm	$w_{measured}$ nm	$w_{corrected}$ nm	$h_{Literature}$ nm	$w_{Literature}$ nm
HA (H1N1)	12.8 ± 1.9	30.9 ± 4.0	20	13.5	4
NA (H1N1)	7.4 ± 1.5	21.4 ± 6.7	15	6	5

geometrical considerations *Equation 4.1* for the corrected width w follows.

$$w = w_{measured} - 2\{(h_{protein} - r_{tip}) \tan \alpha + r_{tip}\} \tag{4.1}$$

Equation 4.1 yields a corrected width for HA (H1N1) of $\sim 20nm$ and for NA (H1N1) of $\sim 15nm$. In both cases the corrected width is still too broad. This discrepancy is assumed be caused through thermal fluctuations of the immobilized proteins. Additionally, the actual opening angle of the tip is expected to be wider in the experiment than the value given by the manufacturer, since the cantilever is typically mounted in the SFM in a tilted position. The measured and calculated values for the height and width of HA and NA are summarized in *Table 4.1*.

Neuraminidase of the type A/Aichi/2/1968 (H3N2)

Immobilization and imaging of the NA (H3N2) of the IV strain A/Aichi/2/1968 (H3N2) was achieved with the same procedure previously described for the HA and NA of the IAV strain California/04/2009 (H1N1). As expected, after incubation with NA (H3N2) proteins, the topography of the NTA-GS showed similar features as seen after incubation with NA (H1N1) proteins. Since the NA (H1N1) and the NA (H3N2) are almost identical in their geometrical appearance and only differ by just a few amino acids, the SFM will not be able to differentiate between the two proteins. A typical image of NA (H3N2) immobilized on NTA-GS is shown in *Figure 4.5*.

The NA (H3N2) cover the NTA-GS well with an inter-protein distance of $\sim 14 \pm 4nm$, as can be seen in *Figure 4.5 a)*. The profiles of six randomly selected NA (H3N2)

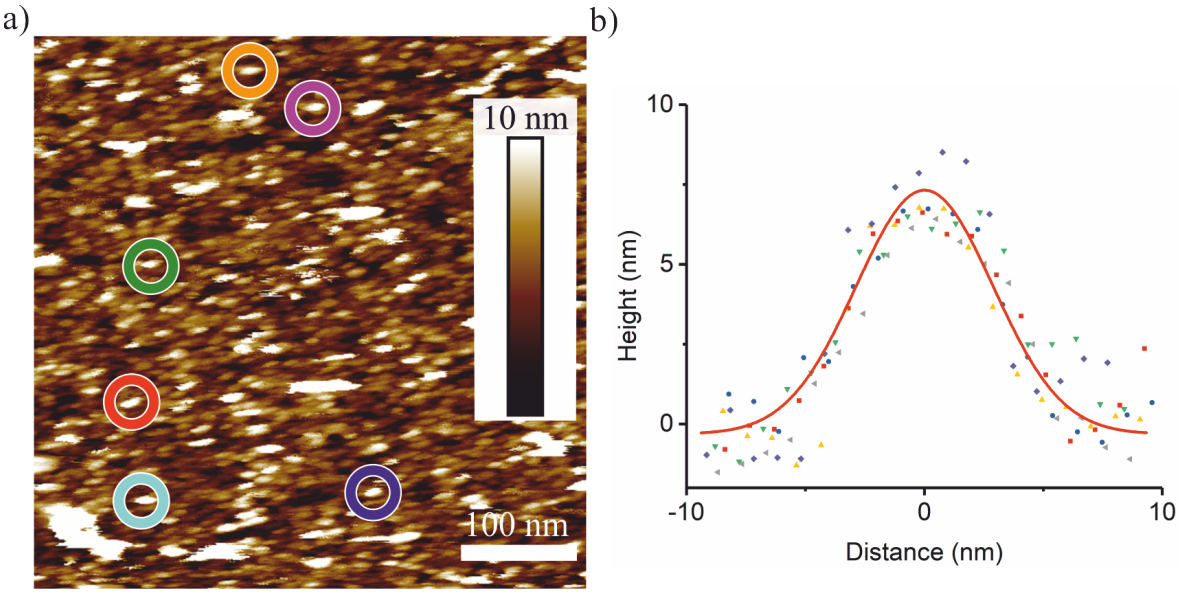

Figure 4.5 – ***Selection of individual NA (H3N2) and corresponding profiles:*** *a) A high resolution SFM image with a size of* $0.5 * 0.5\mu m^2$ *is shown. The image was taken with a Multimode 8 using a tip of the type SNL. Six individual NA (H3N2) are highlighted by colored circles. b) The topographic profiles of the NA (H3N2) highlighted in a) are shown as scatter plots. The solid red line represents the best fit to the concatenated data by a Gaussian function. Profiles were offset by a constant value so that the offset of the fit function is* ≈ 0.

are shown in *Figure 4.5 b)*. The profiles overlap well, indicating that the individual proteins are of the same type. A Gaussian fit is used to determine the height and width of the NA (H3N2) from the concatenated data. The fit returns a height of $h_{NA(H3N2)} \approx 7.6 \pm 0.3nm$ with a standard deviation of $\sigma_{NA(H3N2)} \approx 5.8 \pm 0.3nm$. The height is in good agreement with values reported in literature [163]. Hence, it is assured that the NTA-GS allows the immobilization of his-tagged proteins through metal chelate complexes using Ni^{2+} - ions.

4.1.2 The Influenza Virus A/Aichi/2/1968 (H3N2)

The binding strength and affinity of SA displaying ligands was not only probed for the interaction of the ligands with single proteins but also with whole virions of the strain A/Aichi/2/1968 (H3N2). Using virions has the advantage that the viral proteins NA

and HA are embedded in the viral membrane and, therefore, their natural state and activity is most likely preserved. The immobilization of the virions was achieved though coupling of the virions to a self-assembled monolayer (SAM) of mercaptohexadecanoic acid alkali thiols on a gold 111 surface. The incubation of the SAM with virions allows the virions to adhere to surface, where they become immobilized. A typical image, characteristic for a SAM with immobilized virions, is shown in *Figure 4.6*. The image shows that the SAM is covered with particles of spherical shape after incubation with virions. The particles have a height of $\sim 70 - 120nm$. Even though not all IV particles are always spherical, a diameter of $\sim 100nm$ has been confirmed by Boettcher and colleagues using TEM imaging [83]. This illustrates clearly, that the virions adhere well to the surface and form a dense coating.

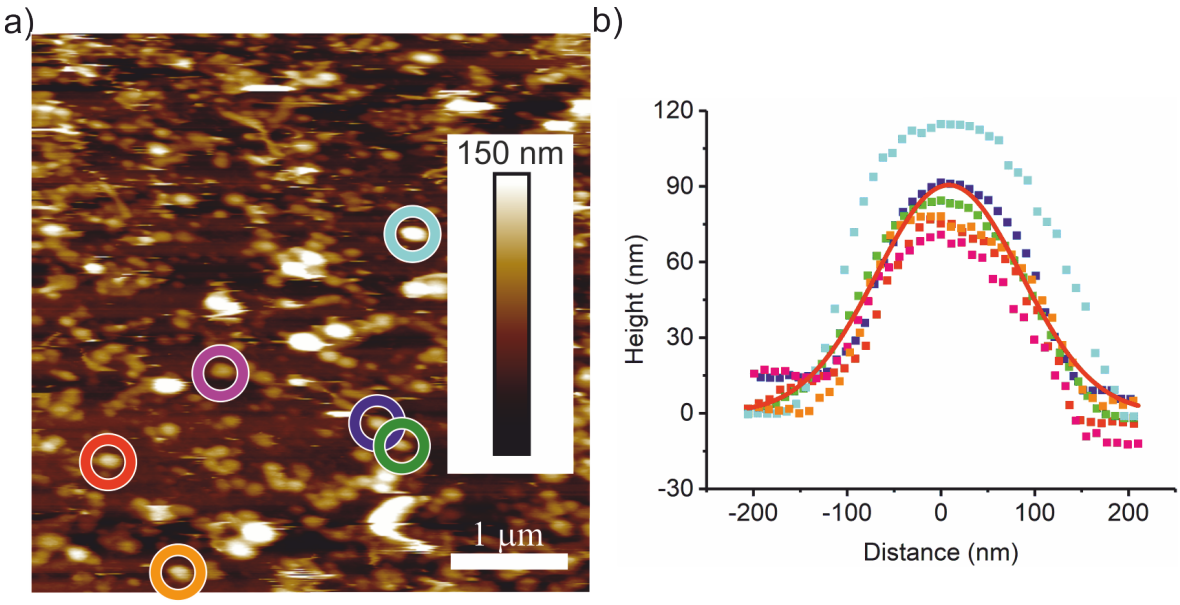

Figure 4.6 – ***IV virions (H3N2) immobilized onto Au-111:*** *a) The image shows the typical topography of the Au111 surface after immobilization with IV virions (H3N2) . The image size* $5 * 5\mu m^2$ *and the color scale represents* $200nm$*. Virions show up as quasi-spherical particles with a height of* $\approx 70 - 120nm$*. The surface is densely covered. b) The image shows the profile of the virion highlighted by the colored circles in a). The height agrees well with previously reported values [83]*

.

4.2 Single Molecule Force Spectroscopy

In the previous section, *section 4.1*, it was shown that viral proteins, as well as full virions, were successfully immobilized on solid substrates. Such an immobilization is essential for the ensuing measurements of binding kinetics. These binding kinetics will be presented and discussed in the upcoming section, which is organized as follows. To begin with, the aspects of the specificity and the valency of the interactions will be illuminated. To this end, the specificity will be confirmed in a competitive binding assay. Such a competitive binding assay might also inspire high throughput inhibitor tests. The aspect of valency will be covered with a theoretical approach that uses the Poisson statistics of bond formation. Secondly, the dynamic force spectra of NA-SA and HA-SA will be analyzed for HA and NA of the type H1N1. Hereby, two models of bond dissociation under force will be examined. The first model is the classic Kramers-Bell-Evans (KBE) model and the second model is the Friddle-Noy-De Yoreo (FNDY) model [128, 147]. From the force spectra, the kinetic parameters of the underlying dissociation will be derived. Following the description of dissociation, the stability of the HA (H1N1) - SA and NA (H1N1) - SA bonds will be investigated through an analysis of the association rate and determination of the dissociation constant. It will be shown that force spectroscopy can provide valuable insight into the stability of biomolecular bonds, but also that care must be taken to not over-interpret the quantitative results. Thirdly, the kinetic characteristics of multivalent protein-ligand interactions will be studied. Hereby, it will be differentiated between the dynamics of uncorrelated and correlated bonds. Uncorrelated bond rupture occurs when multiple ligands of the type SAPEGLA ligands unbind simultaneously. Correlated bond rupture occurs when a single dendritic ligand (dPGSA) binds with several functional groups to multiple neighboring ligand binding domains. Experimental data will be shown for the viral strain X-31 A/AIchi/2/1968 (H3N2). Finally, the experimentally obtained characteristics of the dissociation and association will be interpreted in the biological context of viral infectivity and transimissibility.

4.2.1 Specificity of Rupture Forces

Force spectroscopy suffers from a severe drawback. At no time during the experiment can the actual interaction be witnessed directly. Rather, the observer has to rely on secondary effects to decide whether a force-separation cycle describes receptor-ligand interaction or is the result of unspecific artifacts. An example for such secondary effects is the characteristic unfolding under force of the polymeric tethers that link the ligand to the SFM tip. The saw-tooth shaped stretching curve that is obtained when polymeric tethers, such as polyethylene glycol, are used is a valuable tool for identifying the molecular interactions of interest. An unbinding event specific for receptor-ligand interaction should not only show the characteristic stretching of the polymer but also bond rupture has to occur within a tip-sample separation smaller than the maximum length of the tether. The PEG tether used for the design of SAPEGLA and dPGSA has a contour length of about $40nm$. *Figure 4.7* shows that the bond rupture occurs at a tip-sample separation of about $12nm$ and more than 60% of all events lie within the contour length of the tether. This is a good indication that the ligands bind to the viral proteins.

Even though it provides a well-defined fingerprint, it is not yet sufficient to ensure the desired interactions are detected. This is due to the fact, that the fingerprint only indicates that the ligand on the SFM tip has bound to some part of the surface prior to bond rupture. However, it makes no assumption regarding to which part of the surface the ligand was attached. Without further experimental evidence, it cannot be excluded that the ligand bound unspecifically to the surface instead of binding to the surface immobilized proteins. Therefore, additional control experiments have to be performed to ensure that only specific events contribute to the measured distributions of force and loading rate.

These control experiments are based on a simple statistical approach that is outlined in the following. In general, two distinct kinds of events can occur in a force-separation cycle. Either the retraction trace shows a characteristic rupture event or not. The latter includes not only cases where no adhesion force at all was detected and therefore the retraction trace follows the approach trace, but also those where the adhesive force

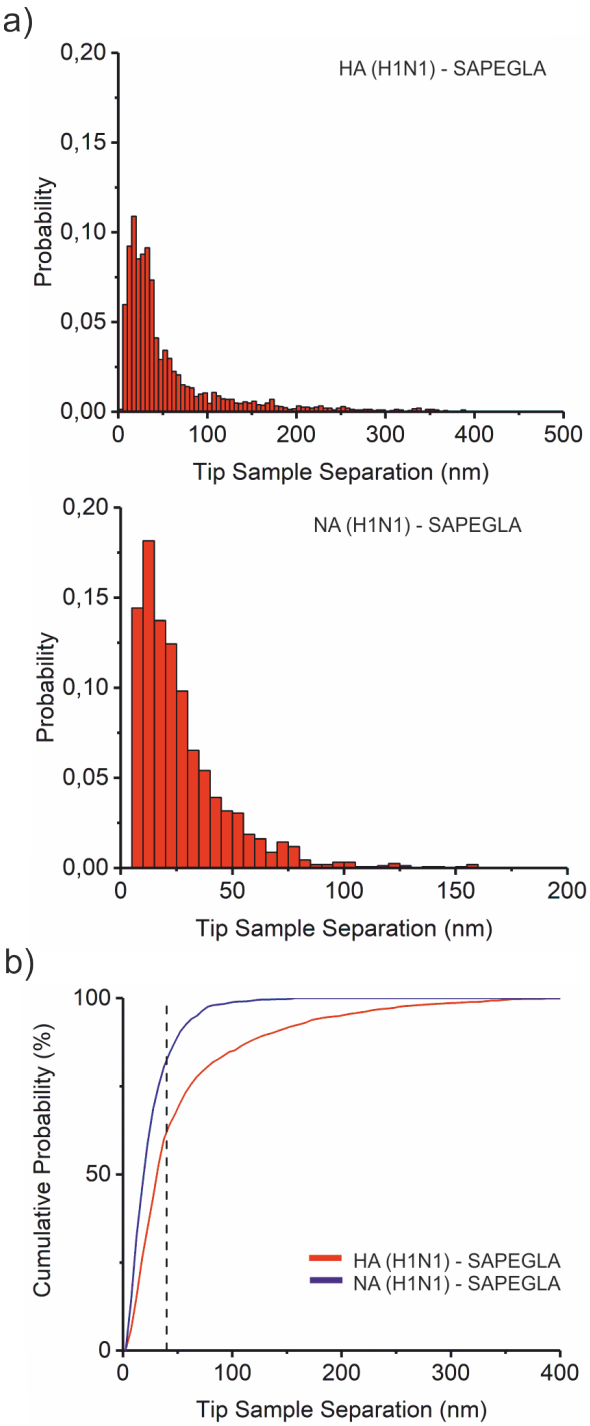

Figure 4.7 – ***Distribution of tip-sample separation at bond rupture:*** *Bonds rupture at different tip-sample separations (TSS). The TSS at bond rupture is used to filter the unbinding events. Unbinding events occurring at a TSS larger than the contour length of the PEG tether are eliminated from the analysis. Panel a) shows the distributions of the TSS at bond rupture of the HA (H1N1) - SAPEGLA and NA (H1N1) - SAPEGLA bonds. Panel b) shows the cumulative distribution function of the TSS at bond rupture of the HA (H1N1) - SAPEGLA (red curve) and NA (H1N1) - SAPEGLA (blue curve) bonds. The dashed, vertical line shows the cut off distance set by requiring the TSS be less than or equal to the contour length of the PEG tether. The most probable TSS is about* $12nm$.

increases linearly with the tip-sample separation. This latter case can be attributed to adhesion of the tip to the surface. By performing a sufficiently high number of force-separation cycles, it becomes possible to calculate the probability of the occurrence of a characteristic rupture event. This probability is called the binding probability p_b and is derived from

$$p_b = \frac{N_{events}}{N_{total}} \tag{4.2}$$

where N_{events} is the number of characteristic events and N_{total} is the total number of recorded force-separation cycles. The binding probability needs to be determined not only for the case where the experimental setup includes the receptor and the ligand that are to be studied, but also for the case when either of the two interaction partners is omitted or replaced by an alternative binder. Such an alternative binder must not have a specific affinity towards the remaining partner. Additionally, the binding probability should be determined for an experimental setup where the formation of a receptor-ligand bond is suppressed by a competitive binder. In the case of viral proteins, competitive binders can also be called inhibitors.

In order to determine p_b for the different scenarios, which are displayed in *Figure 3.3*, the force-separation measurements were generally conducted by approaching the SFM tip towards the support until the predefined setpoint of $\sim 100pN$ was reached, followed by immediate retraction. No additional contact time for molecular interaction was given. Under these condition, the p_b of the ligand SAPEGLA forming a bond with the $Ni^{2+}-NTA$ surface was $\approx 3\%$. When the experiment was repeated after the surface had been incubated with hemagglutinin, the probability of recording an unbinding event was similar, with $p_b \approx 4\%$. The probability of SAPEGLA interacting with neuraminidase was comparable, with $p_b \approx 4\%$. Since the likelihood of recording unspecific events was as high as recording a specific rupture of the protein-sialic acid bond, the surfaces could not be used without further modification. In numerous biochemical applications, including enzyme-linked immunosorbent assay, immunohistochemistry and western blots unspecific adsorption of proteins and protein interactions are blocked using bovine serum albumin (BSA) [164]. BSA is a serum albumin protein derived from cows, that is stable under most experimental conditions and moderately non-reactive. Therefore, it can be used to inhibit unspecific interactions and reduce the background in the

force distributions [144]. Nevertheless, the possibility that the BSA interacts with the influenza proteins and prevents interaction with sialic acid must be excluded. When the $Ni^{2+} - NTA$ surface had been incubated with a solution of $1mg/ml$ BSA in PBS for $0.5h$ prior to recording force-separation cycles, the probability of SAPEGLA interacting with the surface dropped to $p_b \approx 1\%$. When influenza proteins were immobilized on the $Ni^{2+} - NTA$ surface, followed by the incubation with the same BSA blocker solution, a significantly higher p_b was determined. For SPEGLA the probability was $p_b \approx 4\%$ for the interaction with either HA or NA. This demonstrates, on the one hand, that BSA is indeed suitable to reduce unspecific interaction of SAPEGLA with the surface. On the other hand, it shows that the BSA does not bind to the ligand binding domain of either HA or NA and therefore does not interfere with the measurement of the rupture forces of the protein-ligand complexes.

After the influence of the surface had been successfully reduced, further tests of the specificity of the detected rupture events were made. The test included probing the affinity of the control molecule OHPEGLA to either HA or NA, as well as probing the affinity of the ligand SAPEGLA in the presence of or after the incubation of the influenza proteins with competitive binders. As a competitive binder *4-amino-Neu5Ac2en* (*5-acetylamino-2,6-anhydro-4-amino-3,4,5-trideoxy-D-galacto-non-2-enoic acid*) was chosen. *Neu4Ac2en* is one of the few commercially produced neuraminidase inhibitors and is commonly known as oseltamivir carboxylate (OTV). It has previously been shown by Narayan and colleagues [165], that Neu4Ac2 binds to neuraminidase with a significantly higher affinity than sialic acid. Therefore, it was assumed that after the incubation of the surface immobilized neuramindiase further binding of the ligand SAPEGLA would be inhibited. As a second competitive binder *2,6-sialylactose* (6-SAL) was used. The affinity of 6-SAL to hemagglutinin can be considered to be rather low, according to McCullough and colleagues [166]. Nevertheless, it can be expected to prevent binding of the ligand SAPEGLAA, if its concentration is high enough. The summary of these tests can be seen in *Figure 4.8 a)*.

As predicted, *Neu4Ac2en* inhibited neuraminidase well and prevented further binding of the sialic acid on the ligand. The p_b dropped to approximately 1/4 of the p_b before incubation with the inhibitor. When hemagglutinin was incubated with *Neu4Ac2en*,

the p_b was only marginally reduced. This indicates that *Neu4Ac2en* does not have a significant inhibitory effect on hemagglutinin. This is a reasonable assumption, since *Neu4Ac2en* is specifically designed to match the binding pocket of neuraminidase. When the surface immobilized hemagglutinin was incubated with 6-SAL and the slides were rinsed with PBS buffer solution prior to measuring the rupture events, it did not reduce the p_b. When the measurements were repeated without rinsing the slide, the p_b was again reduced. Hence it seems, that even though 6-SAL only interacts weakly with hemagglutinin and can easily be removed, its affinity is still sufficient to inhibit the attachment of SAPEGLA, as long as a sufficiently high concentration is provided in the solution.

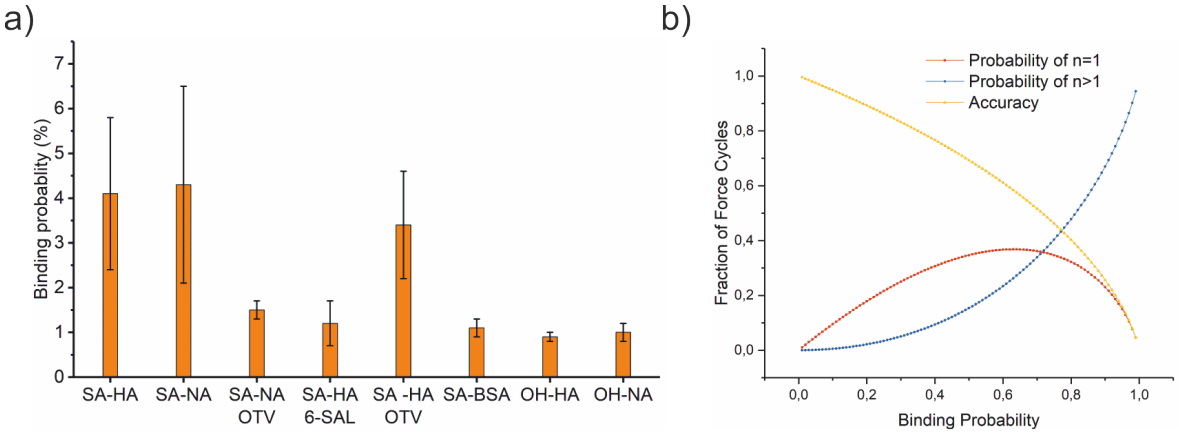

Figure 4.8 – ***Competitive binding assay and valency according to the Poisson distribution:*** *a) The binding probability of SAPEGLA to HA or NA is higher than that of OHPEGLA. After adding a competitive binder, the binding probability of SAPEGLA to HA or NA is reduced. The comparison of the binding probabilities proves the specificity of the interaction of SAPEGLA with the viral proteins. b) The fraction single and multivalent unbinding events of an ensemble of force-separation curves was calculated according to the Poisson statistics. With higher overall binding probability, the likelihood, of multibinding increases.*

The competitive binding assay shows clearly that the ligand SAPEGLA is interacting specifically with influenza proteins hemagglutinin and neuraminidase. Common inhibitors prove to be effective in preventing protein-ligand interactions. The experiments also show that binding of the ligand to the surface in a way that cannot be characterized is still possible and background noise, caused by unspecific rupture events,

will be inevitable in SMFS. Nevertheless, the immobilization of the influenza proteins by complexation of their polyhistidine tag with $Ni^{2+} - NTA$ in combination with the functionalization of the SFM tips with SA, through thiol-gold bond formation is suitable to detect specific protein-ligand interactions.

In order to derive kinetic parameters from DFS experiments, it is not only important to ensure the specificity of detected unbinding events, but also discriminate between the rupture of single and multiple receptor-ligand bonds. To this end, it is desirable to functionalize the receptor displaying surface and the ligand presenting force probe in such a way that only the desired number of bonds can from on probe-surface contact. If only single rupture events are to be studied, the grafting density of molecules on surface and force probe should be kept low. This cannot always be achieved and the detection of multi-bond rupture cannot be excluded. This is especially true when the contact between the force probe and the surface is maintained for longer time spans. The longer contact times will eventually lead to the formation of multiple receptor-ligand bonds. These multi-bonds can rupture simultaneously upon retraction of the force probe. Such a simultaneous rupture is difficult to differentiate from single bond rupture events. The likelihood of detecting single- or multi-bond rupture events can be estimated using Poisson statistics, as it was described by Johnson and colleagues [167]. Following their approach, the probability for single binding $P_{n=1}$ at a given overall binding probability p_b is calculated from

$$P_{n=1} = (p_b - 1) \ln (1 - p_b) \tag{4.3}$$

Consequently, the probability for the formation of multiple bonds $P_{n\neq1}$ is

$$P_{n\neq1} = p_b - P_{n=1} \tag{4.4}$$

The ratio of $P_{n=1}$ to p_b defines the accuracy A of detecting single bond interactions.

$$\begin{aligned} A &= \frac{P_{n=1}}{p_b} \\ &= \frac{(p_b - 1)\ln(1 - p_b)}{p_b} \\ &= \ln\left[(1 - p_b)^{1-\frac{1}{p_b}}\right] \end{aligned} \tag{4.5}$$

The theoretical dependencies calculated from *Equations 4.3, 4.4 and 4.5* are shown in *Figure 4.8 b)*. The figure shows that for small binding probabilities, i.e. $p_b < 0.7$, the probability of forming of a single bond is higher than that of multiple bonds. In the case $p_b \approx 0.04$ the possibility of detecting a single bond is approximately 50 times higher than detecting multiple bonds. This means that the low binding probabilities increase the likelihood of detecting single bond rupture events.

4.2.2 Dynamic Force Spectroscopy

The preceding section has shown that experimental setup is well suited to allow the measurement of specific protein-ligand interactions. This section is now dedicated to the description and analysis of the underlying rupture forces and the dynamic force spectra (DFS) that are obtained for the interaction of either HA or NA with SA. The dynamic force spectra, which illustrate the dependence of inter-molecular rupture forces on the rate of applied force loading, are the key to the extraction of the kinetic parameters of the protein-SA complex [168]. To begin with, the DFS will be analyzed in the framework of the most commonly applied Kramers-Bell-Evans (KBE) model. This approach, at first, is appropriate, since the KBE model is considered as the standard model to analyze DFS. Discrepancies between the extracted DFS and the predictions by the KBE model will be discussed. In the second part of the section, the DFS will be analyzed in the framework of the model developed by Friddle, Noy and De Yoreo (FNDY). It will be shown that the FNDY model provides an adequate description of the data and that it is justified to use the FNDY model for the analysis of further force spectra.

In order to obtain the dependence of the rupture forces over a wide range of loading rates, rupture forces were measured for several distinct retraction speeds in the range of $0.1 - 10\frac{\mu m}{s}$. By increasing the speed of retraction of the SFM tip, the rate of applied

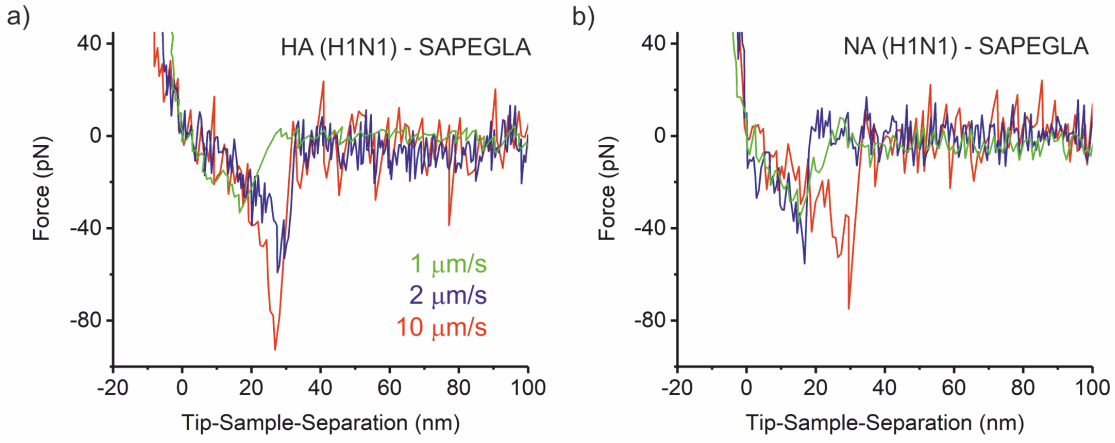

Figure 4.9 – ***Characteristic force-separation curves for HA (H1N1) - SAPEGLA and NA (H1N1) - SAPEGLA are displayed:*** *For the sake of clarity, only retraction traces are displayed. All curves show the characteristic saw-tooth shaped peak, indicating specific binding of the ligands. a) HA (H1N1) - SAPEGLA is shown. b) NA (H1N1) - SAPEGLA is shown. Compared to HA (H1N1) - SAPEGLA, the rupture forces determined for NA (H1N1) - SAPEGLA are similar at low retraction speeds,* $v_{pulling} < 1\mu m/s$. *At higher speeds,* $v_{pulling} > 1\mu m/s$, *NA (H1N1) - SAPEGLA ruptures at lower forces.*

force loading is increased. As mentioned in Chapter 3, Methods, up to several hundred force separation cycles showing characteristic rupture events were collected for each pulling speed. Representative examples of these curves are shown in *Figure 4.9*.

All example curves clearly show the saw-tooth shaped peak. The curves also overlap to a high degree, as it is expected from the stretching behavior of similar polymeric tethers. Additionally, all exemplifying curves have in common, that the bond rupture, indicated by the instantaneous relaxation of the cantilever, occurs at a tip-sample separation that is below the contour length of the PEG tether, $TSS_{bondrupture} < l_c(PEG) = 40nm$. This, together with the competitive binding assay that was described in Section subsection 4.2.1, leads to the conclusion that the displayed rupture events result from specific protein-ligand unbinding. The rupture forces were obtained from fitting the saw-tooth shaped peak with the FJC model as described in *chapter 3*. As expected from the KBE model, the force at which the bond ruptures increases with higher retraction speeds. When the rupture forces of HA (H1N1) - SAPEGLA are

compared with the ones determined for NA (H1N1) - SAPEGLA, it can be seen that the rupture forces are fairly similar at low retraction speeds. On the other hand, at high speeds, HA (H1N1) - SAPEGLA ruptures at higher forces. The rupture forces for each pulling speed were binned into histograms. Examples of these histograms are displayed in *Figure 4.10* for HA (H1N1) - SAPEGLA. At the lowest pulling speeds the rupture forces were $\approx 20pN$. At the highest pulling speeds the rupture forces of the NA (H1N1) - SAPEGLA bond reached $\approx 60pN$, while the rupture forces of the HA (H1N1) - SAPEGLA bond reached $\approx 90pN$.

Typically, all distributions have a similar appearance with a well-defined peak at lower forces and a shoulder at higher forces. This behavior deviates from the predicted classical KBE model. As shown in the Fundamentals, for a constant rate of force loading, the KBE model predicts a force distribution with a tail at low forces and a steep decline at high forces. The forces contributing to the first peak are assigned to the single bond interactions. The forces that build up the shoulder are assumed to be the result of two different effects. On the one hand, the few remaining, inevitable interactions of the ligand with the surface will contribute to an overall background force. On the other hand, binding of multiple ligands and their almost simultaneous rupture upon tip retraction cannot be completely neglected. The probability density function (PDF) that provides the theoretical distribution of rupture forces is approximated by applying a multi-modal Gaussian fit to the histograms. The fits determine the most probable rupture force, which is the maximum of the PDF, and the standard deviation. The standard deviation characterizes the spreading of rupture forces as a result of the stochastic nature of the rupture process, as described in chapter 2.

Example of the distributions of the critical loading rates, that correlate with the rupture forces are shown in *Figure 4.11*.

The critical loading rates, that were extracted from the slope of the FJC fit to the saw tooth of the force-separation curve, show broad distribution. This illustrates the influence of polymeric tethers on the DFS. Nevertheless, the distributions have a well-defined peak. To extract the most probable loading rate, the histograms are fitted with multi-modal Gaussian functions.

In the same fashion, NA (H1N1) - SAPEGLA was studied. Typically obtained

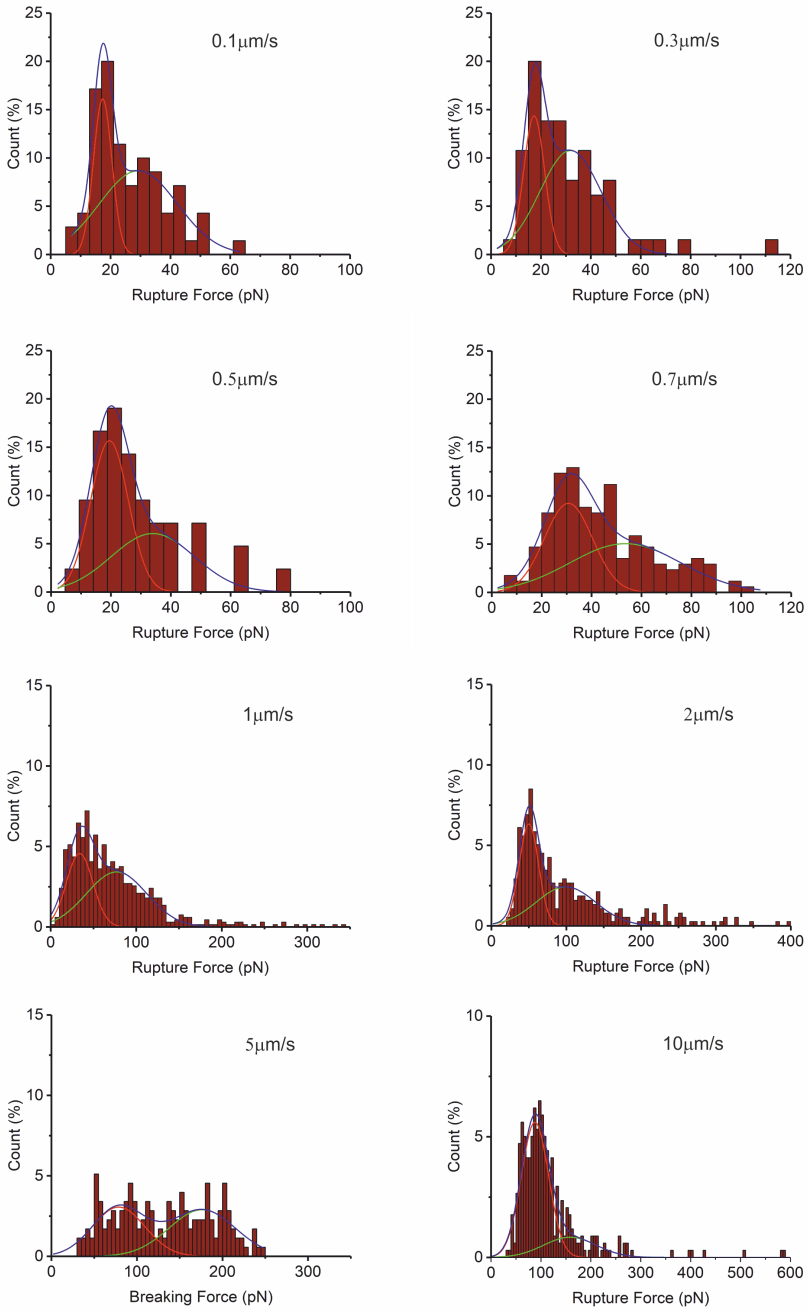

Figure 4.10 – ***Distributions of rupture forces obtained for HA (H1N1) - SAPEGLA:*** *The distributions are typically characterized by a distinct peak at low forces and a shoulder at higher forces. The peak at low forces is assumed to be the result of single bond rupture. In several cases the shoulder resembles the shape of a second peak. Forces of the second peaks tend to match multiples of the single bond peak. The distribution at different retraction speeds show that the most probable rupture forces of the single bond interactions increase with increasing retraction speed.*

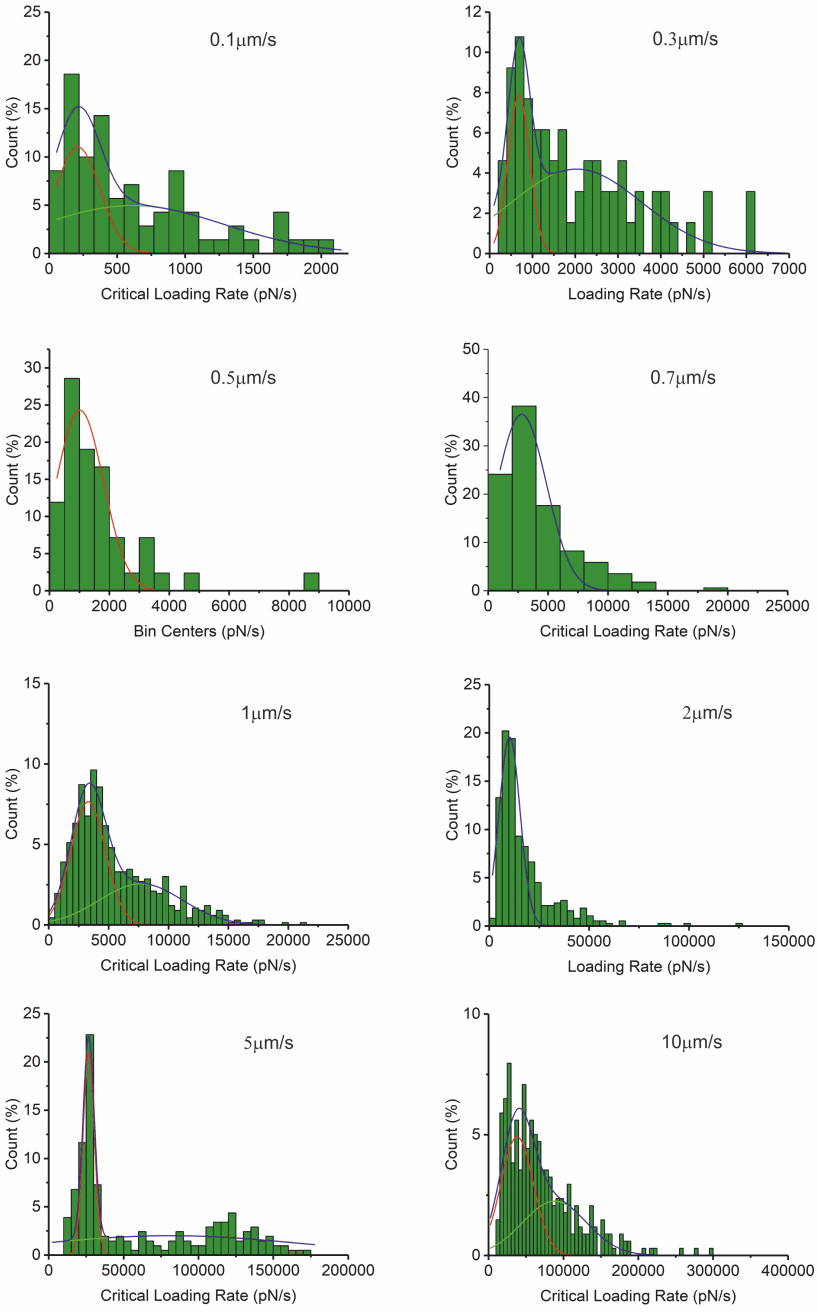

Figure 4.11 – ***Distributions of critical loading rates obtained for HA (H1N1) - SAPEGLA*** *The distributions are typically characterized by a distinct peak at low loading rates and a shoulder at higher loading rates. Distributions are fitted with bi-modal Gaussian functions to derive the most probable critical loading rate.*

distributions of the rupture forces are shown in *Figure 4.12*, while the corresponding distributions of the critical loading rates are shown in *Figure 4.13*. With the determination of the most probable forces at the most probable critical loading rates for a broad range of pulling speeds, the DFS can be plotted. The spectra are illustrated in *Figure 4.14*.

The force histograms *Figures 4.10 and 4.12* show that the measured rupture forces are small, especially in the case of low pulling speeds. This raises the question, whether these forces are truly intrinsic of the underlying molecular unbinding process or whether they are overlaid by the instrumental and statistical noise [169]. For a typical setup for force spectroscopy experiments, there is a force threshold that limits the range of detectable forces. If modern instrumentation is used, the instrumental noise, i.e. the Johnson noise, is minimal [170, 171]. Therefore, the limiting noise is determined from the thermal fluctuations of the SFM cantilever. Typical force spectra are recorded at pulling speeds between $0.1 - 10\mu m/s$ and the force probe moves over a distance of $\approx 1\mu m$ during approach and retract. This results in a measurement frequency between $0.1 - 10s^{-1}$. In this context, the measurement frequency describes the frequency, at which force-separation curves are measured. It is the reciprocal of the duration of one complete force-separation cycle. This measurement frequency is approximately three orders of magnitude smaller than the fundamental resonance of the SFM cantilevers, used in the experiments. As a result, the RMS noise ΔF becomes a function of the thermal energy k_BT, the spring constant k_c and the angular resonance frequency ω_0 of the cantilever [169].

$$\Delta F = \left(\frac{4k_BTk_cB}{\omega_0 Q}\right)^{1/2} \tag{4.6}$$

Here B is the detection bandwidth and Q the quality factor. The bandwidth depends linearly on the pulling velocity v_{pull} and the density D_N of recorded data points per travel distance. With $B = v_{pull}D_N/2$ the dependence of ΔF on v_{pull} can be calculated.

$$\Delta F = \left(\frac{2k_BTk_cD_N}{\omega_0 Q}v_{pull}\right)^{1/2} \sim v_{pull}^{1/2} \tag{4.7}$$

In order to compare the experimental data with the force threshold, the RMS noise

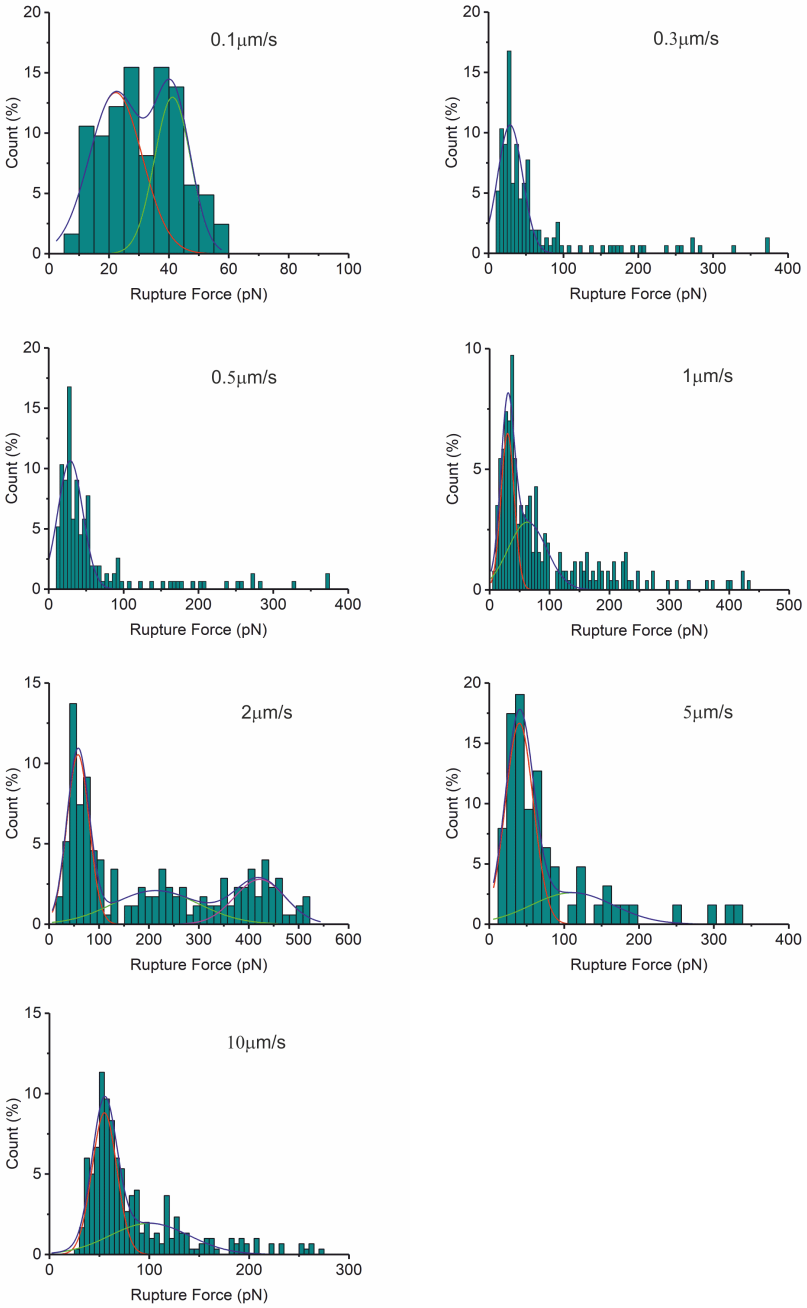

Figure 4.12 – ***Distributions of rupture forces obtained for NA (H1N1) - SAPEGLA:*** *The distributions are typically characterized by a distinct peak at low forces and a shoulder at higher forces. The peak at low forces is assumed to be the result of single bond rupture. In several cases the shoulder resembles the shape of a second peak. Forces of the second peaks tend to match multiples of the single bond peak. The distributions at different retraction speeds show that the most probable rupture force of the single bond interactions increases with increasing retraction speed.*

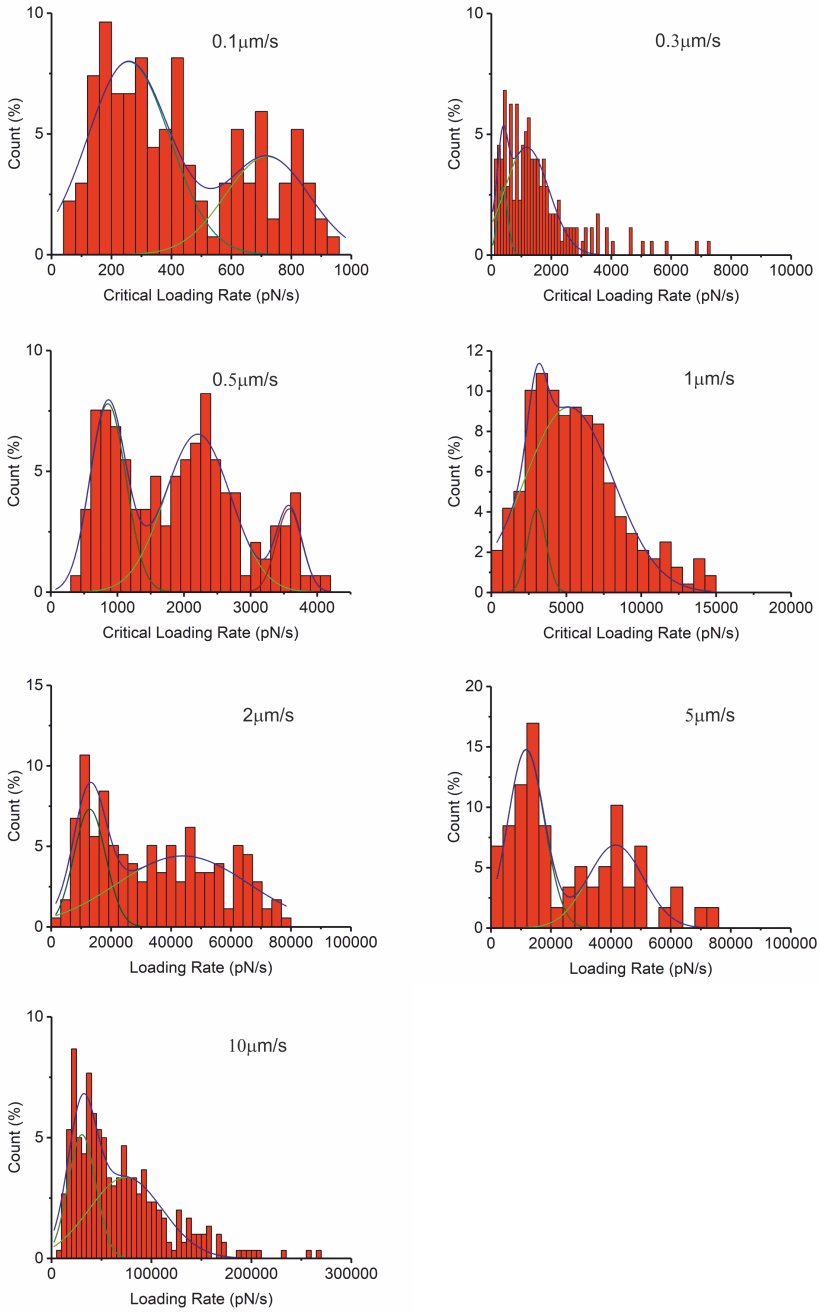

Figure 4.13 – ***Distributions of critical loading rates obtained for NA (H1N1) - SAPEGLA:*** *The distributions are typically characterized by a distinct peak at low loading rates and a shoulder at higher loading rates. Distributions are fitted with multi-modal Gaussian functions to derive the most probable critical loading rate.*

was calculated for the OBL cantilever. For the spring constant, the nominal value of $30mN/m$ was used. The resonance frequency and quality factor were determined from the thermal noise spectrum of the cantilever in PBS buffer. This returned $\omega_0 = 10kHz$ and $Q = 2$. The final force threshold levels were calculated for a signal-to-noise ratio (SNR) of $SNR = 1$ as well as $SNR = 4$ and are shown in *Figure 4.14 a)* together with the most probable rupture forces of the HA (H1N1) - SAPEGLA and NA (H1N1) - SAPEGLA rupture events. The figure illustrates that the rupture forces, that were determined from the force histograms, are well above the force threshold of the experimental setup. This holds even for a signal-to-noise ratio of $SNR = 4$. Therefore, the pulling speed dependent RMS noise does not interfere with the analysis of the protein-ligand bonds.

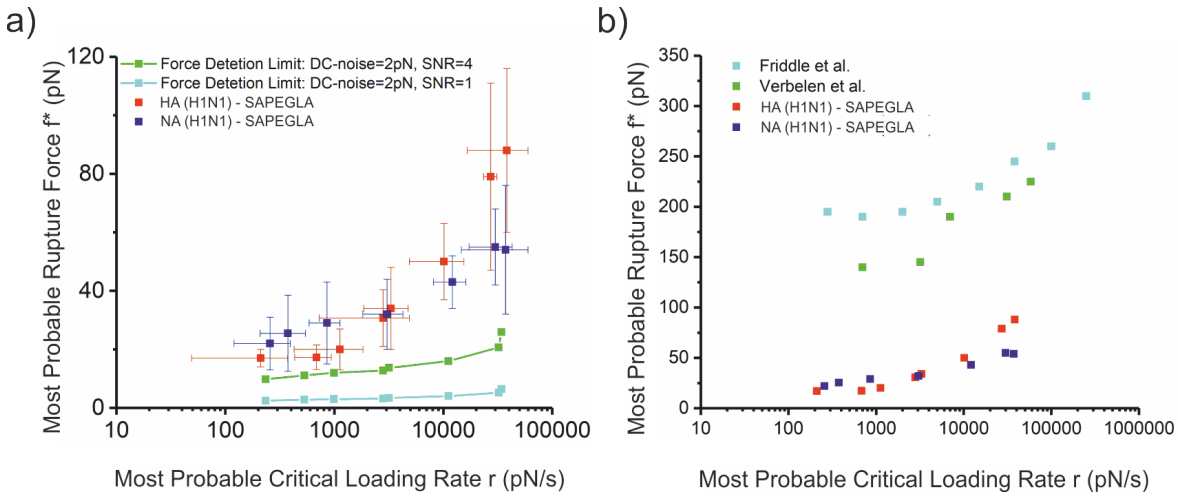

Figure 4.14 – ***Dynamic force spectra, the noise induced force threshold and the strength of* histag – Ni^{2+} – NTA***:*** *a) The DFS of the HA (H1N1) - SAPEGLA (red) and NA (H1N1) -SAPEGLA (blue) interaction are shown along with the velocity dependent detection limit, which limits the detection of rupture events. The detection limit was calculated for a signal-to-noise ratio of $SNR = 1$ (cyan) and $SNR = 4$ (green). All of the rupture forces ($\pm SD$) are well above the detection limit, even for $SNR = 4$. b) The most probable rupture forces of the protein-SAPEGLA bonds are shown in relation to the bond strength that was measured for histag – Ni^{2+} – NTA bonds by Verbelen and colleagues and Friddle and colleagues [172, 147]. The protein-SAPEGLA bond is significantly weaker and will rupture before the protein torn off the surface.*

The most probable rupture forces of the protein-ligand interaction are shown in

Figure 4.14 b) together with the rupture forces of the $histag - Ni^{2+} - NTA$ bonds that were determined by Verbelen and colleagues and Friddle and colleagues [172, 147]. This illustrates that the forces required to rupture the protein-ligand bonds are far weaker than those required to rupture the $histag - Ni^{2+} - NTA$ bonds. Hence the ligands will be separated from the protein before the critical force is reached at which the protein is ripped from the surface.

Analysis within the Bell-Evans Framework

With the most probable rupture forces and loading rates determined, it now becomes possible to analyze the kinetics of HA (H1N1) - SAPEGLA as well as NA (H1N1) - SAPEGLA. As previously described in *chapter 3*, the DFS illustrates the dependence of the bond strength on the rate of applied force. Following the KBE model, a log-linear dependence is expected and the kinetic parameters k_{off} and x_β are derived. In the simplest case, a single energetic barrier for the bond dissociation is assumed. Therefore, the fit of the DFS depends on only two free parameters. Both spectra are fitted with the KBE model that was introduced in *section 2.5*, assuming a single barrier. To commemorate its fundamental significance, *Equation 2.6* is once more shown below.

$$F(r) = \frac{k_B T}{x_\beta} ln\left(\frac{r x_\beta}{k_{off} k_B T}\right) \tag{4.8}$$

With the off rate k_{off} the height of the energy barrier ΔG can be calculated [148].

$$\Delta G = -k_B T ln\left(\frac{k_{off}\hbar}{k_B T}\right) \tag{4.9}$$

The DFS of HA (H1N1) - SAPEGLA and NA (H1N1) - SAPEGLA are displayed in *Figure 4.15* together with the fits according to the KBE model.

It shows, that the DFS data of the NA (H1N1) - SAPEGLA complex follows the predictions of the KBE model fairly well and a $k_{off} = (1.3 \pm 0.7)\, s^{-1}$ together with a $x_\beta = (657 \pm 68)\, pm$ is obtained. The errors account for the standard error of the fit. Using the k_{off} the barrier is derived: $\Delta G = (29 \pm 1)\, k_B T$. The error is calculated according to the Gaussian error propagation. While the single barrier approach provides a reasonable description of the NA (H1N1) - SAPEGLA complex, it

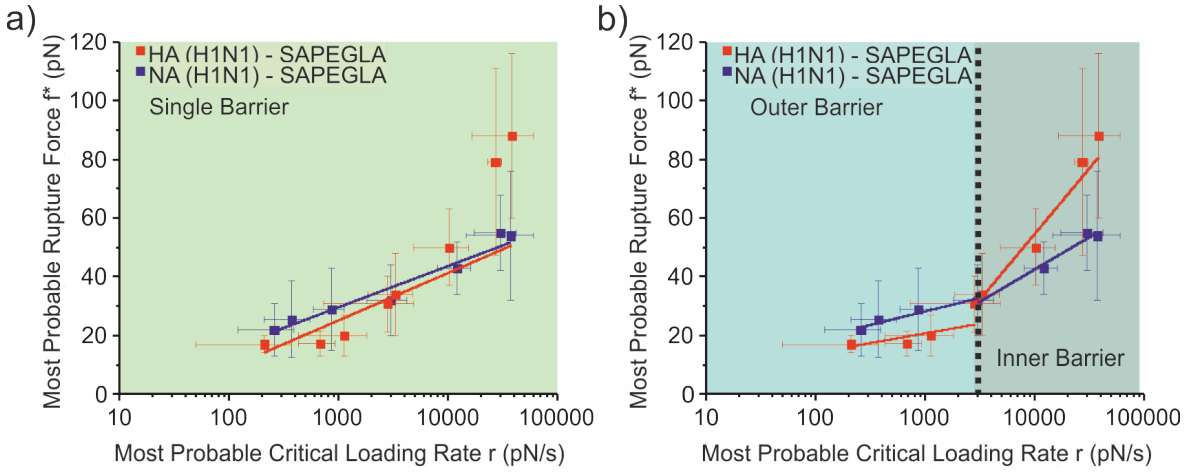

Figure 4.15 – ***Dynamic force spectra and the KBE model:*** *a) The DFS were fitted with the KBE model, assuming a single transition state. The fit describes the DFS of NA (H1N1) - SAPEGLA well, but fails to match the DFS of HA (H1N1) - SAPEGLA. b) With the assumption of two energetic barriers, the DFS of both interactions can be split into a regime of low and of high rates of force loading. The KBE model fits both regimes well and kinetic parameters, which describe the inner as well as the outer barrier, are obtained.*

fails to match the full DFS data obtained for the HA (H1N1) - SAPEGLA complex. By taking a closer look on the experimental force spectrum, a deviation from the log-linear dependence can be seen. Appearance of more than one log-linear regime is a common phenomenon in SMFS [147]. Typically, this mismatch of the experimental data with the theoretical prediction is interpreted as the coexistence of several barriers in the free energy landscape of the molecular bond. These additional barriers are related to intermediate states [173]. Under the assumption of two barriers, the DFS data of the HA (H1N1) - SAPEGLA complex is split into two independent regimes. The regime of low loading rates is defined by $r < 300pN/s$ and the regime of high loading rates is defined by $r > 3000pN/s$. Within each regime, the dependence is expected to follow the theoretical prediction and the kinetic parameters are obtained using *Equations 2.6* and *4.9*. For low loading rates one obtains: $k_{off} = (0.7 \pm 1.4)\, s^{-1}$, $x_\beta = (1.1 \pm 0.5)\, 10^3 pm$ and $\Delta G = (30 \pm 2)\, k_B T$. For the high loading rates one obtains: $k_{off} = (31 \pm 5)\, s^{-1}$, $x_\beta = (206 \pm 25)\, pm$ and $\Delta G = (26.1 \pm 0.2)\, k_B T$. Even though the DFS of the NA (H1N1) - SAPEGLA interaction does not clearly show

Table 4.2 – ***Kinetic parameters extracted from the DFS data by application of the KBE model as seen in Figure 4.15***

Protein	**Type of Barrier**	k_{off}	τ	x_β	ΔG
		s^{-1}	s	pm	k_BT
NA (H1N1)	single	1.3 ± 0.7	0.8	657 ± 68	29 ± 1
	slow loading	0.2 ± 0.2	5	$(1 \pm 0.2) * 10^3$	31 ± 1
	fast loading	12 ± 5	0.08	450 ± 50	27.0 ± 0.5
HA (H1N1)	single	3 ± 3	0.3	571 ± 169	$28 \pm 1.$
	slow loading	0.7 ± 1.4	1.4	$(1.1 \pm 0.5) * 10^3$	30 ± 2
	fast loading	31 ± 5	0.03	206 ± 25	26.1 ± 0.2

two distinctive linear regimes, it is well worth considering this approach. In fact, a closer examination of the DFS indicates indeed a non-linear trend. Therefore, the force spectrum is split into a regime of low and a regime of high loading rates, analogous to the DFS of HA (H1N1) - SAPEGLA. The independent fitting of the two regimes yields the following kinetic parameters. In the regime of low loading rates: $k_{off} = (0.2 \pm 2)\, s^{-1}$, $x_\beta = (1.0 \pm 0.2)\, 10^3 pm$ and $\Delta G = (31 \pm 1)\, k_BT$. In the regime of high loading rates: $k_{off} = (12 \pm 5)\, s^{-1}$, $x_\beta = 450 \pm 50 pm$ and $\Delta G = (27.0 \pm 0.5)\, k_BT$. All kinetic parameters that were determined using either the single barrier or the double barrier approach, are summarized in *Table 4.2*

Analysis within the Friddle-De Yoreo Framework

Non-linear force spectra are a common sight in force spectroscopy [147]. This is especially true if the DFS is recorded over a large interval of loading rates [174, 175, 176]. Typically, the force spectra are fitted with a sequence of successive linear regimes. This method was successfully applied in the previous part. In some studies on different receptor-ligand interactions of various complexity, even more than two regimes are assumed [177]. While this might be the correct interpretation for systems of high complexity, simpler systems will most likely dissociate along a direct path without intermediate states. In addition, simulated force spectra at loading rates beyond the experimentally

accessible regime have shown that non-linearity is omnipresent [36].

In the following paragraph, the force spectra of both protein-ligand complexes will be analyzed in the framework developed by Friddle, De Yoreo and colleagues [178, 147, 151]. The model provides an adequate description of non-linear force spectra by assuming an equilibrium and a kinetic regime. In the equilibrium regime the kinetics are influenced by the potential of the force transducer. The potential of the transducer allows broken bonds to rebind. Only in the kinetic regime are the proteins and ligands truly irreversibly separated. As outlined in *chapter 2*, the equation that was derived by Friddle and colleagues is given in *Equation 2.15*. It spans over the equilibrium and kinetic regimes.

The force dependent transition rates for unbinding, $k_u(F)$, and binding, $k_b(F)$, define the transition from the equilibrium regime to the kinetic regime. The rate equations were introduced in *Equation 2.11* and *Equation 2.11*. These equations allow an estimation of f_{eq} by using typical kinetic parameters of the system. Sieben and colleagues studied the interaction of influenza A virions of the types H3N2 and H1N1 with several cell lines [69]. The values extracted for the virion-cell constellation $H1N1-A549$ were $k_{off} = (1.16 \pm 0.13)\, s^{-1}$ and $x_\beta = (0.18 \pm 0.06)\, nm$. The characteristic properties of the force transducers in SFM based SMFS are the resonance frequency ν_{res}, which sets the binding rate at $F = 0$, and the stiffness k_t. Therefore, reasonable values are $k_u^0 = 10^4 s^{-1}$ and $k_t = 10pN/nm$. The force dependent transition rates calculated with these values are shown in *Figure 4.16*.

As the force is increased, the binding rate quickly drops, while the unbinding rate increases. The intersection of both rates sets the equilibrium force, $f_{eq} \approx 28pN$. This force is well within the DFS data determined for HA (H1N1) - SAPEGLA and also, to a lesser extent, within the data of NA (H1N1) - SAPEGLA. Even though the actual forces and kinetic parameters of the IV-cell interaction might be different from the more artificial protein-ligand complex and also, the effects of different experimental parameters, such as k_t and k_u^0 have an effect on the transition rates, it is still fair to take *Figure 4.16* and the extracted f_{eq} as an indication that the FNDY model is applicable to the DFS data of HA (H1N1) - SAPEGLA and NA (H1N1) - SAPEGLA. Finally, the nonlinear DFS data were fit with *Equation 2.17*. As can be seen in *Figure 4.17*,

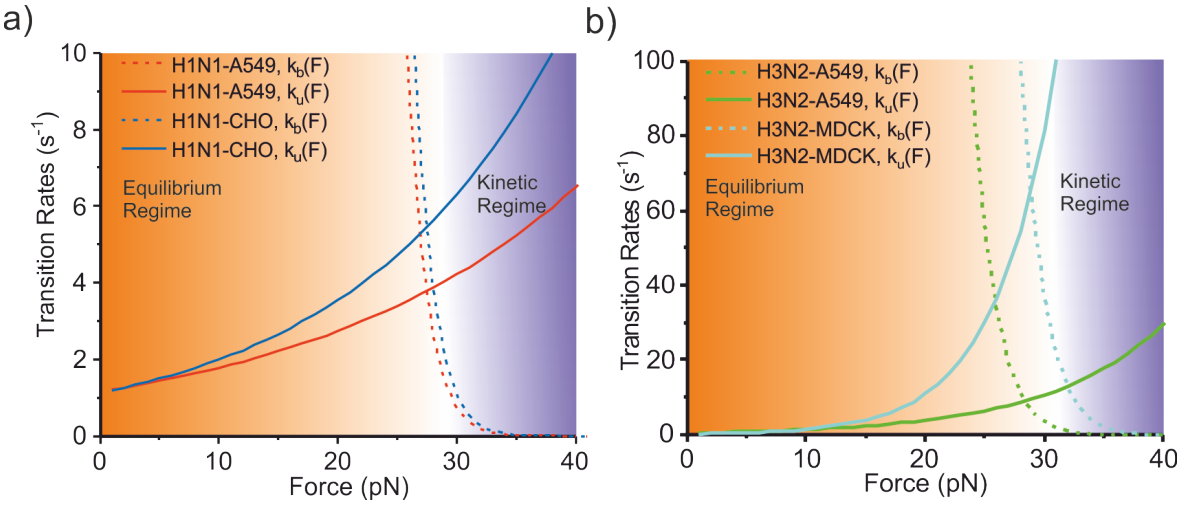

Figure 4.16 – ***Force dependent transition rates and the application of the FNDY model onto the DFS:*** *Force dependent transition rates were calculated for typical kinetic parameters, taken from SMFS studies with IV and cells. The figure illustrates the rapid drop of the binding rate as the force increases, while meanwhile the unbinding rate increases. Both rates intersect at the equilibrium force f_{eq}. The intersection of the rates defines the equilibrium regime, where reforming of the inter-molecular bond is allowed, and the kinetic regime, where rebinding is prohibited due to the high loading rates. The calculations are based on parameters found by Sieben and colleagues [69]. a) Rates are calculated for virions of the type H1N1. b) Rates are calculated for virions of the type H3N2.*

the FNDY provides a good description of the experimental data obtained from both proteins.

The fit determines the equilibrium force f_{eq}, the force scale f_β and the dissociation rate $k_{off}\,(f_{eq})$ that occurs when the bond is loaded with f_{eq}, as previously described. These fit parameters allow the derivation of the rupture length x_β, the energy barrier ΔG and the thermal dissociation rate, k^0_{off} in the absence of external forces. All parameters are summarized in *Table 4.3*. As expected from the dynamic force spectra shown in *Figure 4.17* the NA (H1N1) - SAPEGLA bond is characterized by a higher f_{eq} compared to the HA (H1N1) - SAPEGLA bond. The energy barrier is calculated by using the expression $\Delta G = {f_{eq}}^2/\,(2 * k_t)$. This implies a higher energetic barrier for the dissociation of SA from NA (H1N1) than from HA (H1N1). As a consequence of

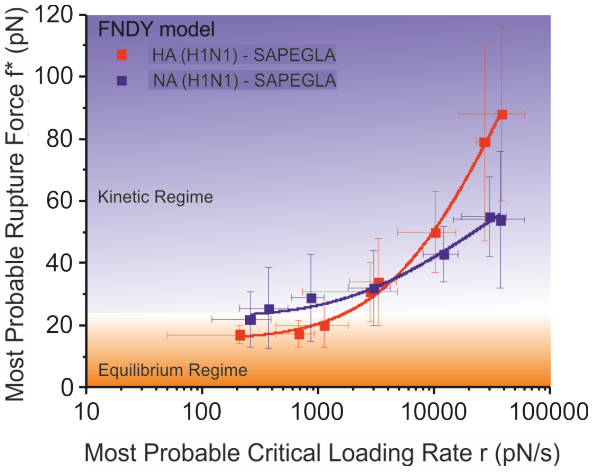

Figure 4.17 – ***Application of the FNDY model onto the DFS:*** *The FNDY model, which includes rebinding effects in the process of forced dissociation, describes the DFS of HA (H1N1) - SAPEGLA and NA (H1N1) - SAPEGLA well and the kinetic bond parameters are obtained.*

Table 4.3 – ***Kinetic parameters extracted from the DFS data by application of the FNDY model*** *The spectra were fitted with Figure 4.17*

Protein	f_{eq}	f_β	$k_{off}\,(f_{eq})$	k^0_{off}	x_β	ΔG
	pN	pN	s^{-1}	s^{-1}	pm	k_BT
NA (H1N1)	22.3 ± 1.6	12 ± 3	112 ± 52	18 ± 8	345 ± 87	32 ± 8
HA (H1N1)	15.1 ± 0.8	38 ± 9	97 ± 19	66 ± 13	106 ± 26	12 ± 2

its lower f_β, the NA (H1N1) - SAPEGLA bond features a larger x_β. These findings show that the NA (H1N1) - SAPEGLA bond is characterized by a deeper and broader potential well. The dissociation rate of unforced dissociation k^0_{off} is calculated by rearranging *Equation 2.11* and inserting $k_{off}\,(f_{eq})$. It follows, that k^0_{off} is larger for HA (H1N1) - SAPEGLA than for NA (H1N1) - SAPEGLA and therefore the bond lifetime τ is larger for NA (H1N1) - SAPEGLA. This is in agreement with the predicted shape of the energy landscape. According to the Kramers theory of molecular dissociation, the bound complex needs more attempts in order to overcome the higher barrier. This results in the longer bond lifetime.

So far, it has been shown that the kinetic parameters that describe the dissociation of the ligand SAPEGLA from either HA (H1N1) or NA (H1N1) can be derived from the dynamic force spectra. It can be seen in *Tables 4.2 and 4.3* that the actual values of the kinetic parameters depend on the model that is used to fit the DFS as well as the number of energetic barriers of the energy landscape. Therefore, it is worth comparing the results that were obtained by the different assumptions.

In *Figure 4.18* k_{off}^0 and the corresponding x_β are plotted simultaneously. It shows, that in general the KBE model results in a lower k_{off} and higher x_β. This is in agreement with the primary condition of the KBE model of irreversible unbinding. The FDYN model results in higher dissociation rates, since it includes rebinding effects. In the case of a single energetic barrier or the low loading rate regime, the KBE model produces large x_β between $6 - 12\text{Å}$. These large values could be interpreted as indications that rebinding is influencing the DFS, especially in the low loading rate regime. If rebinding is occurring in the low loading rate regime, large separation distances between protein and ligand are required to irreversibly separate the protein-ligand complex. Also, the large relative standard error indicates that the KBE model is not well suited to fitting the full DFS. In the regime of high loading rates, the KBE model leads to a significantly higher k_{off} relative to the regime of low loading rates or the assumption of a single barrier. The increase is on the order of one magnitude. On the other hand, x_β is reduced by a factor of approximately two to five. The kinetic parameters obtained with the KBE model in the regime of high loading rates are rather similar to the ones obtained using the FDYN mode. This is especially true in the case of NA (H1N1). This is a good indication that the FNDY model is well suited for describing the complete force spectra. The agreement of the kinetic parameters clearly shows, that the FNDY model is an extension of the KBE model to include reversible binding. Regarding HA (H1N1), the x_β that are derived from the two approaches are fairly similar, but the k_{off} derived from the FDYN model is approximately twice as large as the one derived from the KBE model. This is not a surprise, if the fit with the KBE model in *Figure 4.15* is examined. The fit underestimates the high forces at high loading rates as a consequence of their large standard deviation. The discrepancy between the two dissociation rates can be explained if it is assumed that, even at high loading rates, the unbinding of the

HA (H1N1) - SAPEGLA complex is still influenced by rebinding effects. Therefore, the DFS displayed in *Figure 4.15* might not show the true kinetic regime of HA (H1N1) - SAPEGLA unbinding. Unfortunately, the unbinding forces could not be determined at higher loading rates, since the instrumental limitations had been reached. Nevertheless, a quantitative as well as qualitative description of the unbinding of SA from either HA (H1N1) or NA (H1N1) could be achieved.

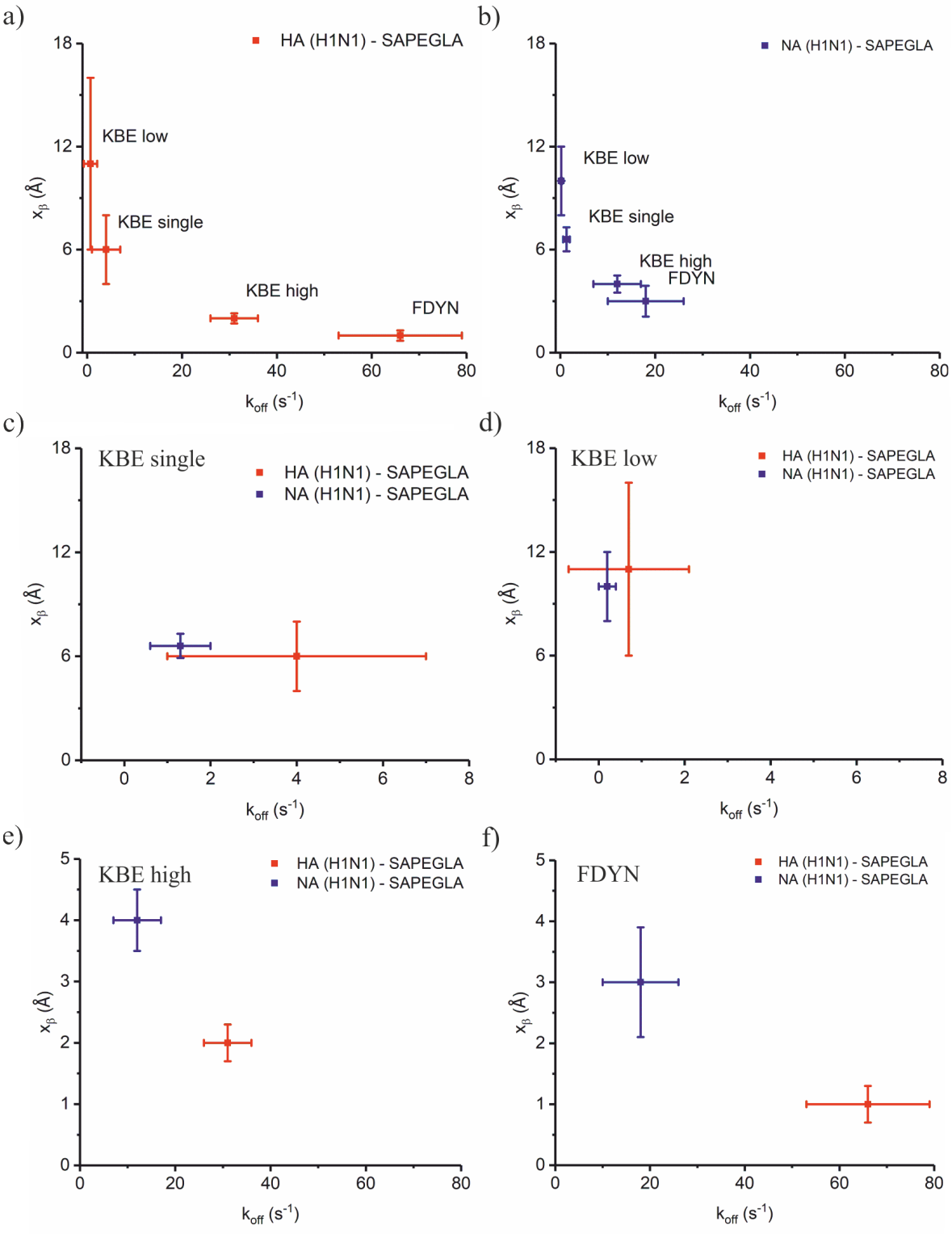

Figure 4.18 – ***The dissociation rate,*** $\mathbf{k_{off}}$***, and rupture length,*** $\mathbf{x_{beta}}$***, of HA (H1N1) - SAPEGLA and NA (H1N1) - SAPEGLA:*** *The parameters were determined using either the KBE or the FDYN model. When the KBE model was used, parameters were determined for either a single or two energetic barriers.*

4.2.3 Receptor-Ligand Association and Bond Stability

The stability of large systems that are composed of a high number of macro-molecules interacting with one another is not only affected by the dissociation rate of a single bond. In such ensembles the dissociation of just a single or even a few bonds is usually not significant for the whole. More likely it is the interplay of permanent formation and separation of receptor-ligand pairs that ensures a stable equilibrium condition [179]. This equilibrium is defined by the dissociation constant K_D or its reciprocal the association constant K_A [180].

If $[protein]$ and $[SA]$ denote the molar concentration of protein and SA and $[proteinSA]$ the molar concentration of the protein-SA complex, then K_D and K_A are defined by *Equations 4.10* and *4.11* with the dissociation and association rates k^0_{off} and k_{on}.

$$K_D = \frac{[protein]\,[SA]}{[proteinSA]} = \frac{k^0_{off}}{k_{on}} \tag{4.10}$$

$$K_A = \frac{[proteinSA]}{[protein]\,[SA]} = \frac{k_{on}}{k^0_{off}} \tag{4.11}$$

In this sense, in order to further characterize the stability of the protein-SA bond K_D will be determined. Since in the previous part k^0_{off} has been determined, this paragraph will focus on the calculation of k_{on}. The k_{on} describes the number of receptor-ligand pairs that form within an interaction time τ in the accessible effective volume, as described by Hinterdorfer and colleagues [179]. Following this approach, k_{on} can be calculated using *Equation 4.12*, with the Avogadro constant N_A, the effective Volume for interaction V_{eff}, the number of involved protein-ligand pairs n and the interaction time τ. The interaction time sets the timescale for the formation of a single receptor-ligand bond.

$$k_{on} = N_A V_{eff} / (n\tau) \tag{4.12}$$

The probability p_b for bond formation is examined in order to determine the interaction time. Since it can be assumed that p_b is an intrinsic property of the protein-

ligand complex within a given time t_1, it can be expected that it will increase for a longer time $t_2 > t_1$. Given enough time, the p_b will saturate at a maximum that is the results of the equilibrium between the formation and dissociation of bonds. The time until the p_b reaches half its maximum, $p(\tau) = p_b^{max}/2$ is called the interaction time τ.

The dependence of the binding probability p_b on the contact time t_c follows an exponential decay, that is given by *Equation 4.13* [181].

$$p_b(t_c) = p_b^{max}\{1 - \exp[-(t_c - t_0)/\tau]\} \tag{4.13}$$

According to *Figure 4.19 b)* both protein-ligand complexes exhibit a similar dependence of $p_b(t_c)$ and therefore the interaction time τ is also similar with $\tau_{H1-SA} = (1.16 \pm 0.05)\,s$ and $\tau_{N1-SA} = (1.3 \pm 0.1)\,s$.

Since the interaction time has been determined for both viral proteins, the association rate can be calculated. To this extend it is essential to consider the volume V_{eff}, within which a bound SA molecule can interact with a protein on the surface. According to Baumgartner and colleagues [180] the effective Volume is equal to a half-sphere with the effective radius r_{eff}, where r_{eff} is related to the free equilibrium state of the ligand SAPEGLA. Hence, it is a good first assumption to associate the gyration radius of the PEG tether, r_g^{PEG}, with r_{eff}. The PEG used for the synthesis of the ligand SAPEGLA has a molar weight of $m_M = 5kDa$, which is equivalent to about 110 monomers. Hence, r_g^{PEG} is approximately $4nm$ [182]. Force-separation curves typically showed only one, if any, unbinding event of specific interaction. Even when the contact time was increased, the number of unbinding events remained 0 or 1 and seldom 2. This is a clear indication, that only one protein-ligand pair was available for complex formation during the particular force-separation curve, and therefore, it holds that $n = 1$. This agrees well with the Poisson analysis that was illustrated in *Figure 4.8 b)*. Since the overall binding probabilities, *Figure 4.19*, barely exceed 30%, the theoretical likelihood of finding single-binding events is $> 80\%$.

The association rate can now be calculated using *Equation 4.12*, resulting in $(67 \pm 6)\,M^{-1}s^{-1}$ for HA (H1N1) - SAPEGLA and $(62 \pm 5)\,M^{-1}s^{-1}$ for NA (H1N1) - SAPEGLA. As a consequence of the similar interaction time, the association rates are the same within error and the dissociation constant depends solely on the dissociation

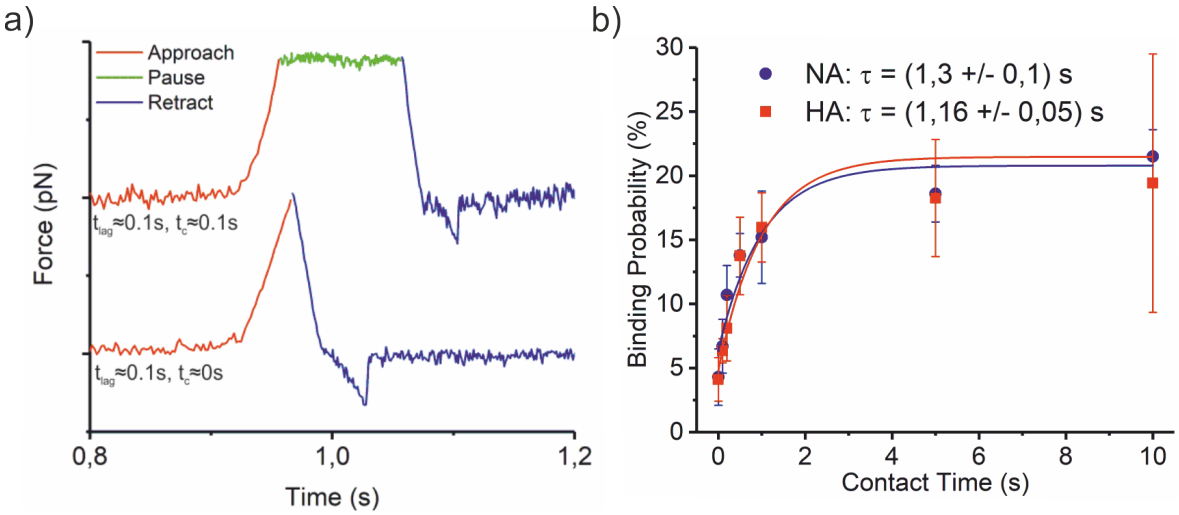

Figure 4.19 – ***Force-time curves with the same lag time but different contact time and the dependence of the binding probability on contact time:*** *a) The Image illustrates the difference between lag and contact time. In both force-time curves the approach speed is* $0.5\mu m/s$*, the retract speed is* $1\mu m/s$ *and the setpoint defining the force at which retraction starts is* $100pN$*. Therefore, the resulting lag time is the same for both curves, with* $t_{lag} \approx 0.1s$*. This sets the minimal duration of the contact between SFM tip and surface. In the upper curve an additional contact time* t_c *is introduced, during which tip-surface contact is maintained. The probability to detect specific rupture events is expected to increase with* t_c*. b) The binding probability increases with increasing contact time. As the time of contact between the SFM tip and the surface is increased, the time for SA to find and attach to a LBD on either HA (H1N1) or NA (H1N1) is also increases. Hence, the probability of bond formation and detection of rupture events will increase likewise. The experimental data can be fitted with an exponential decay function,* $p_b(t_c) = p_b^{max}\{1 - \exp[-(t_c - t_0)/\tau]\}$*, yielding the interaction time.*

rate k_{off}^0. The dissociation constants of the protein-SA complexes are calculated using *Equation 4.10* and it yields: $K_D^{HA} = (950 \pm 190)\, mM$ and $K_D^{NA} = (290 \pm 130)\, mM$. These values unveil, that NA (H1N1) is forming a stronger bond with SA compared to the bond between HA (H1N1) and SA. Nevertheless, both connections appear to be very weak. Indeed, the K_D values determined here are one to two orders of magnitude larger than those typically found in literature, e.g. determined by NMR spectroscopy [25, 23]. This discrepancy can be explained through the different experimental conditions, in which K_D values were determined. Unlike NMR spectroscopy, where the dissociation behavior of freely flowing proteins and SA is observed, SMFS imposes more constrains on the interaction between HA (H1N1) and NA (H1N1) with SA [183]. Therefore, it has to be carefully examined, how these constrains affect the stability of HA (H1N1) - SAPEGLA and NA (H1N1) - SAPEGLA. Through the immobilization of receptors and ligands to either the surface or the SFM tip their freedom of motion will be limited. This will most likely reduce the association rate k_{on}. Furthermore, the thermal motion of the PEG tether induces additional stress on the molecular bond, which in the process increases the dissociation rate k_{off} [183]. Regarding the influence of the PEG tether, it is also worth to consider the dependence of K_D on r_{eff}. From *Equation 4.12*, which shows a cubic dependence of the dissociation constant on the effective radius, $K_D \sim r_{eff}^3$, it becomes clear that the right choice of r_{eff} will have a enormous effect on the determination of K_D. Even though it has been a reasonable assumption that bond formation occurs mostly at equilibrium conditions and that the gyration radius of the PEG tether accounts for the effective radius, $r_{eff} = r_g^{PEG} \approx 4nm$, it is worth to consider association kinetics far from equilibrium where the PEG tether is partially stretched. In theory r_{eff} is only limited by the contour length of the tether, with $r_{eff} \leqq l_C^{PEG} \approx 40nm$. The dependence of K_D on r_{eff} can be seen in *Figure 4.20*. As predicted, K_D drops rapidly as r_{eff} increases. At roughly 1/3 of the contour length, which is equal to $\approx 13nm$, and above the K_D tends to values that are very close to those previously reported. Most importantly it shows that K_D^{NA} is approximately three times larger than K_D^{HA}, independent of the absolute value. This fully conforms the higher stability of the NA (H1N1) - SAPEGLAcomplex compared to the HA (H1N1) - SAPEGLA complex.

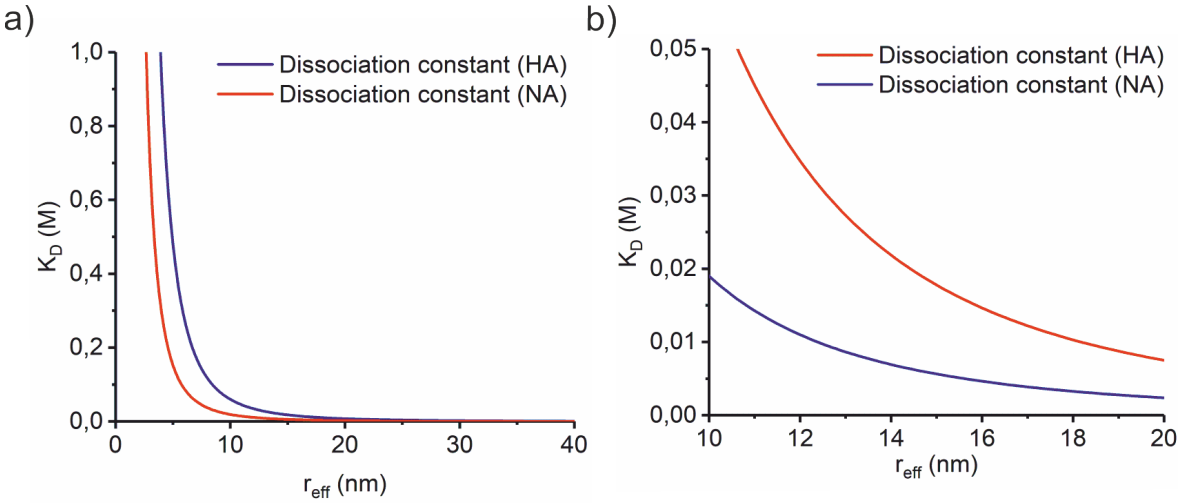

Figure 4.20 – ***Dissociation constant*** $\mathbf{K_D}$***:*** *The dissociation constant decreases at a larger effective radius* r_{eff}*. In* ***a)****,* K_D *is shown for* r_{eff}*, for which it holds:* $0nm < r_{eff} < l_c^{PEG} = 40nm$*. In* ***b)****,* K_D *is displayed for an interval of* r_{eff}*, that is more relevant for binding. Independently of the effective radius, hemagglutinin shows an approximately three times larger* K_D *than neuraminidase. This confirms the more stable binding of SAPEGLA to NA (H1N1) compared to HA (H1N1)*

4.3 Multivalent protein-ligand binding

Generally, in DFS, multivalent binding can occur in two different constellations. On the one hand, DFS can create the situation, where several monovalent ligands bind simultaneously to a multitude of receptors. This case is typically a result of dense surface coating with receptors in combination with dense functionalization of the force probe with ligands. The formation of multiple bonds can also be triggered when the time of contact between the surface and the force probe is increased, giving more time to the ligands to find receptors. On the other hand, a single ligand can be designed in such a way, that it displays several reactive terminal groups. All of these terminal groups have the ability to bind to receptors and therefore, the ligand is multivalent in itself. This situation is in fact inherent to the majority of DFS experiments, since most receptor-ligand pairs are multivalent on the atomistic level. This applies for example to the ligand SAPEGLA, since it interacts simultaneously with several amino acids within the LBD of HA and NA through multiple hydrogen bonds. Yet, in many experiments

such atomistic details can be neglected. In the case of SAPEGLA the actual binding strength will not simply be the sum of all hydrogen bonds but rather be influenced by other effects such as conformational entropy. Another example for a multivalent ligand is the dendritic ligand dPGSA, which can be considered as a true multivalent ligand, since its binding strength is expected to substantially depend on its ability to simultaneously bind multiple ligand binding domains [22].

First, this section will focus on the simultaneous interactions of several monovalent ligands. In the second part of the section, the interaction of the dendritic ligand dPGSA, which was outfitted with multiple SA and specifically designed to inhibit IAV, will be described.

4.3.1 Kinetics of Multiple Parallel Bonds

In order to study the simultaneous binding of monovalent ligands of the type SAPEGLA to HA full influenza virions of the strain A/Aichi/2/1968 (H3N2) were used. The virions provide the advantage that their surface is densely covered with the transmembrane proteins. This ensures that a multitude of ligands is presented when the force probe is brought in close proximity to an individual virion. The kinetics of multiple bonds between SAPEGLA and NA were examined using recombinant NA of the same viral strain. Once a certain number $n > 2$ of receptor-ligand bonds has been formed and the force probe is retracted, two different mechanisms of bond rupture are possible. The bonds can either fail one after another or all bonds fail almost simultaneously so that the rupture of the individual bonds is recognized as a single event. If the bonds rupture one after another, the process of force loading of an individual bond is most likely obscured. Therefore, it is difficult and requires complex descriptions of the underlying polymer dynamics that precede bond dissociation. If multiple bonds rupture simultaneously, kinetic parameters can be derived more easily. In this case the external force is shared among all protein-ligand bonds and rupture of bond leads to the immediate failure of the whole cluster. The arrangement of bonds is also referred to as a system of uncorrelated parallel bonds [129]. It will be addressed in this section.

It has been shown in the previous section, *Section 4.2.3*, that the probability of bond formation increases when the contact time between probe and surface is increased. It has

also been illustrated in *Figure 4.8 b)*, that the probability of the formation of multiple bonds depends on the single bond binding probability. Consequently, an increase of the contact time between probe and surface will inevitably lead to the formation of multiple bonds. The simultaneous rupture of these multi-bonds will result in higher rupture forces, since the total force will be shared among individual bonds [184]. Sharing of the force also influences the rate of force loading [185]. In the multivalent system the PEG tethers that connect the individual ligands to the force probe will be stretched simultaneously and have to be similarly treated to a parallel arrangement of springs. This leads to a higher stiffness of the force transducer, since the combined stiffness of springs arranged in parallel is equal to the sum of the stiffness of the individual springs. Therefore, force loading at a given separation speed will be higher in the multivalent system compared to the monovalent. Such a behavior is illustrated in *Figure 4.21*. The force-separation curves, that are shown in *Figure 4.21 a)*, represent characteristic curves of the interaction between HA (H3N2) and SAPEGLA, while the force-separation curves in *Figure 4.21 b)* are representative for the interaction between NA (H3N2) and SAPEGLA. The separation speed is the same in all curves. The force separation curves show clearly, that the bond strength is increased at a higher bond valency. The loading rate at a fixed pulling speed is also increased likewise, since the effective stiffness of the force transducer is increased as a result of the PEG tethers that are arranged in parallel. This can be seen from the increased negative slope at the point of bond rupture.

In principle, it is possible to determine the exact valency of the underlying interaction in each individual force-separation curve by fitting the curves with a multivalent FJC model [186]. However, this not necessary, since the most probable rupture forces and most probable critical loading rates can as well be determined from the bulk data [181]. To this extent, the rupture forces and the corresponding critical loading rates extracted at a particular pulling speed were binned into histograms to obtain the distributions of the rupture forces and loading rates. Two examples of these histograms are displayed in *Figure 4.22*, showing the rupture forces for HA (H3N2)- SAPEGLA and NA (H3N2) - SAPEGLA determined at one separation speed.

The distributions of the rupture forces at each pulling speed appear similarly shaped. They are characterized by several distinctive peaks. The relative height of the peaks is

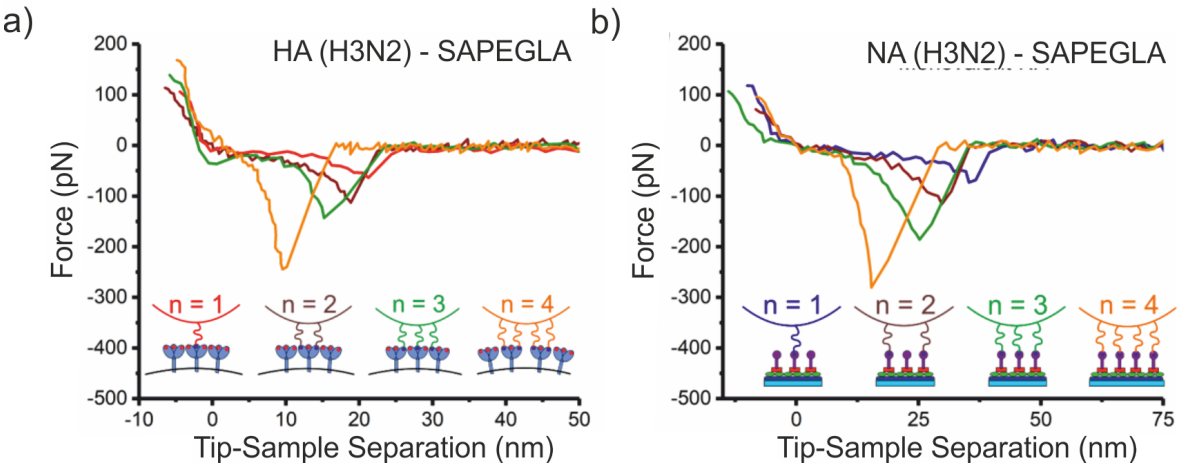

Figure 4.21 – ***Multivalent binding of monovalent ligand:*** *Characteristic force-separation curves taken at a fixed pulling speed are shown: a) For the interaction of HA (H3N2) - SAPEGLA. b) For the interaction of NA (H3N2) - SAPEGLA. The force-separation curves show the expected increase in bond strength with the number bond. The increase of the loading rate, as a result of the higher stiffness of the force transducer in the case of multi-bonds, can be observed. (Parts of the image were provided by Dr. Jose Luis Cuellar-Camacho).*

reduced with increasing force. Typically, four peaks can be identified in each histogram. The individual peak forces appear to be multiples of the force of the lowest peak force. This finding is similar to the study on biotin-avidin interaction by Ernst-Ludwig Florin, Vincent T. Moy and Hermann E. Gaub in which rupture force histograms with multiple distinctive peaks were also observed [140]. Using an autocorrelation analysis, the peaks were related to a 'force quantum' of about $160pN$ characteristic of the underlying molecular unbinding. The existence of such a force quantum was also suggested by Allen and colleagues [187]. The quantization of the unbinding force of multiple parallel bonds was revised by Philip M. Williams who estimated the most probable unbinding forces f_p^* of the parallel bonds to be below integer multiples of the most probable single bond rupture force f_s^*, i.e. $f_p^* < f_s^*$ [188]. Rupture force histograms of multivalent binding were also extensively examined by Erdmann and colleagues who derived an expression for the distribution of rupture forces assuming equal sharing of the force between the closed bonds [189]. These preceding considerations allow to correlate the peaks found in the distributions of rupture forces with the bond number and extract

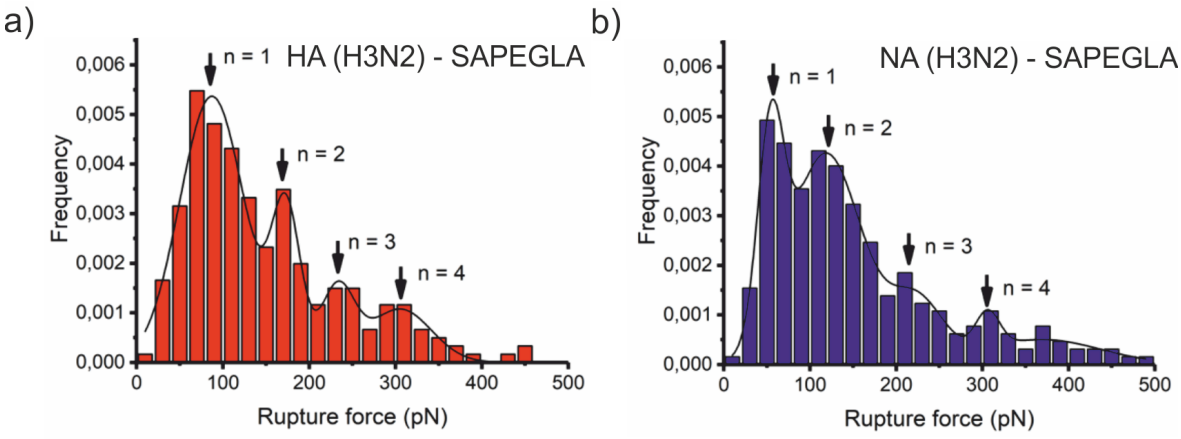

Figure 4.22 – ***Multivalent rupture forces of the interaction between H3HA-SAPEGLA and N2NA-SAPEGLA:*** *a) The ruptures forces determined for H3HA-SAPEGLA are shown. b) The ruptures forces determined for N2NA-SAPEGLA are shown. Both histograms were obtained from force separation curves taken at the same separation speed. The histograms show distinctive peaks with decreasing intensity indicating the rupture of n=1,2, and 4 bonds. (Parts of the image were provided by Dr. Jose Luis Cuellar-Camacho)*

the most probable rupture forces. The peaks at the lowest force are attributed to the rupture of a single protein-ligand bond. The peaks at higher forces are consequently attributed to the simultaneous rupture of two, three or four protein-ligand bonds. The peak positions and standard deviations are determined from fitting the histograms with multi-modal Gaussian functions, in analogy to the studies by Baumgartner and colleagues and Rankl and colleagues [190, 181]. The distributions of the critical loading rates are treated likewise and the most critical loading rates are obtained relative to the bond number and retraction speed. Therefore, the correlation between bond strength and the rate of force loading is determined for increasing bond valency. The resulting dynamic force spectra of the interactions between HA (H3N2) and NA (H3N2) with SAPEGLA are displayed in *Figure 4.23*.

As expected, the forces required to rupture the protein-ligand bonds increased if more bonds are ruptured at the same time. All force spectra, but especially those of low valency, feature a non-linear dependence of f^* on $\ln\left(\frac{df}{dt}\right)$. Similar to the analysis of the interaction between HA (H1N1) and NA (H1N1) with SAPEGLA the transition

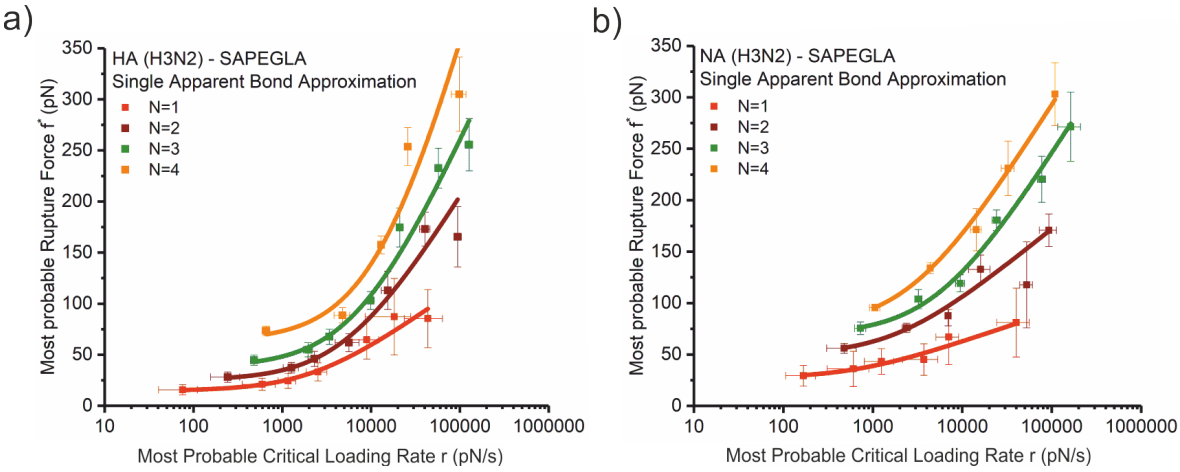

Figure 4.23 – ***Force spectra of the interaction HA (H3N2) - SAPEGLA and NA (H3N2) - SAPEGLA:*** *a) The force spectra determined for HA (H3N2) - SAPEGLA are shown. b) The force spectra determined for NA (H3N2) - SAPEGLA are shown. The force spectra illustrate the increased of the most probable rupture forces at higher valency. A deviation from the linear dependence on* $\ln(r)$ *is observed. The solid lines represent the fits to the spectra according to the FNDY model using the assumption of a single apparent bond.*

rates for binding, $k_{on}(f)$, and unbinding, $k_{off}(f)$, of a single bond between SAPEGLA and HA (H3N2) or NA (H3N2) under force can be estimated from *Equations 2.12 and 2.11*, which were introduced in *Section 4.2.2*. For the estimation of $k_{off}(f)$ and $k_{on}(f)$, the parameters were used that had been reported by Sieben and colleagues [69]. The dependence of both rates on the applied force was shown in *Figure 4.16*. The rates cross at the equilibrium force $f_{eq} \approx 28pN$.

This suggests, that the dynamic force spectra for both proteins stretch over the equilibrium and the kinetic regime. Therefore, the FNDY model is appropriate for the determination of the kinetic parameters. From a conceptual point of view, it is plausible to treat the parallel arrangement of identical bonds as a single apparent bond between two interacting multivalent surfaces. This so called 'single apparent bond approximation' was introduced by Friddle and colleagues [147]. The dynamic force spectra are individually fitted with *Equation 2.17* under the assumption of generic equilibrium force f_{eq}, an apparent thermal force scale f_{β}^{app} and an apparent force induced dissociation rate $k_{off}^{app}(f_{eq})$ at the equilibrium force.

Table 4.4 – ***Kinetic parameters extracted from the multivalent DFS of HA (H3N2) - SAPEGLA by application of the FNDY model, as seen in 4.23***

Valency	f_{eq}	f_{β}^{app}	$k_{off}\,(f_{eq})$	$k_{off}^{app}(0)$	x_{β}^{app}	ΔG
	pN	pN	s^{-1}	s^{-1}	nm	k_BT
1	15 ± 2	27 ± 6	48 ± 13	28 ± 8	0.15 ± 0.03	15 ± 5
2	25 ± 5	62 ± 16	51 ± 19	35 ± 13	0.07 ± 0.02	14 ± 6
3	38 ± 5	84 ± 17	51 ± 14	32 ± 9	0.05 ± 0.01	27 ± 8
4	64 ± 13	139 ± 105	56 ± 31	36 ± 20	0.03 ± 0.02	48 ± 20

Table 4.5 – ***Kinetic parameters extracted from the multivalent DFS of NA (H3N2) - SAPEGLA by application of the FNDY model, as seen in 4.23***

Valency	f_{eq}	f_{β}^{app}	$k_{off}\,(f_{eq})$	$k_{off}^{app}(0)$	x_{β}^{app}	ΔG
	pN	pN	s^{-1}	s^{-1}	nm	k_BT
1	27 ± 5	13 ± 5	29 ± 27	4 ± 4	0.31 ± 0.12	37 ± 14
2	49 ± 8	31 ± 8	34 ± 21	7 ± 4	0.13 ± 0.03	49 ± 16
3	69 ± 8	60 ± 16	52 ± 23	17 ± 7	0.07 ± 0.02	71 ± 20
4	77 ± 4	60 ± 7	26 ± 6	7 ± 2	0.07 ± 0.01	60 ± 14

The kinetic parameters that were extracted from the fits are given in *Table 4.4* and *Table 4.5*.

The values given in these tables show an outcome that is unexpected at first glance. Firstly, the dissociation rate k_{off}^{app} is constant and does not change with the bond number N in the case of both proteins. This surprises, because the dissociation rate of the multivalent system is expected to decrease since more bonds are supposed to increase the overall stability. Secondly, the rupture length x_{β}^{app} decreases to values as small as $0.01nm$ that is about an order of magnitude smaller than the atomic length scale of $0.1nm$. Such small values are unrealistic from the chemical point of view. This discrepancy between the kinetic parameters obtained from the single apparent bond approximation and the expected was pointed out by Friddle and colleagues who suggested that the

Table 4.6 – ***Thermal force scale, rupture length and dissociation rate of the HA (H3N2) - SAPEGLA interaction after scaling of f_β^{app} with N***

Valency	f_β^{app} pN	f_β nm	x_β s^{-1}	$k_{off}(0)$
1	27 ± 6	27 ± 6	0.15 ± 0.03	28 ± 8
2	62 ± 16	31 ± 8	0.13 ± 0.02	23 ± 9
3	84 ± 17	28 ± 6	0.15 ± 0.01	13 ± 4
4	138 ± 105	35 ± 26	0.12 ± 0.02	9 ± 5

thermal force scale f_β scales with the number of bonds [147]. In this article, they also derived an extension of their equation, *Equation 2.15* to describe a cluster of a number N of multivalent parallel bonds. This extended FNDY model is shown in *Equation 4.14*.

$$\begin{aligned} f^* &\cong f_{eq} + N f_\beta \exp\left(\frac{N}{R\left(f_{eq}/N\right)}\right) E_1\left(\frac{N}{R\left(f_{eq}/N\right)}\right) \\ R\left(f_{eq}/N\right) &= \frac{r}{k_u\left(f_{eq}/N\right) f_\beta} \end{aligned} \tag{4.14}$$

The comparison of *Equation 4.14* with *Equation 2.15* leads to the conclusion that the single apparent bond approximation results in an apparent thermal force scale f_β^{app} that is proportional to the number of bonds, as shown in *Equation 4.15*. The rupture length and force free dissociation rate can now be corrected using this scaling relation.

$$f_\beta^{app} = N * f_\beta \tag{4.15}$$

The corrected values obtained are given in *Table 4.6* and *Table 4.7*.

The correlations between the kinetics of the multivalent protein-ligand complexes and the valency are depicted in *Figure 4.24*. The figure also illustrates the differences between HA (H3N2) and NA (H3N2). The experimentally obtained kinetic parameters are compared to theoretical predictions that follow the assumptions proposed by Williams and Evans that will be discussed in the following [129, 188].

In *Figure 4.24 a)* the dependence of the force free dissociation rate k_{off} on the

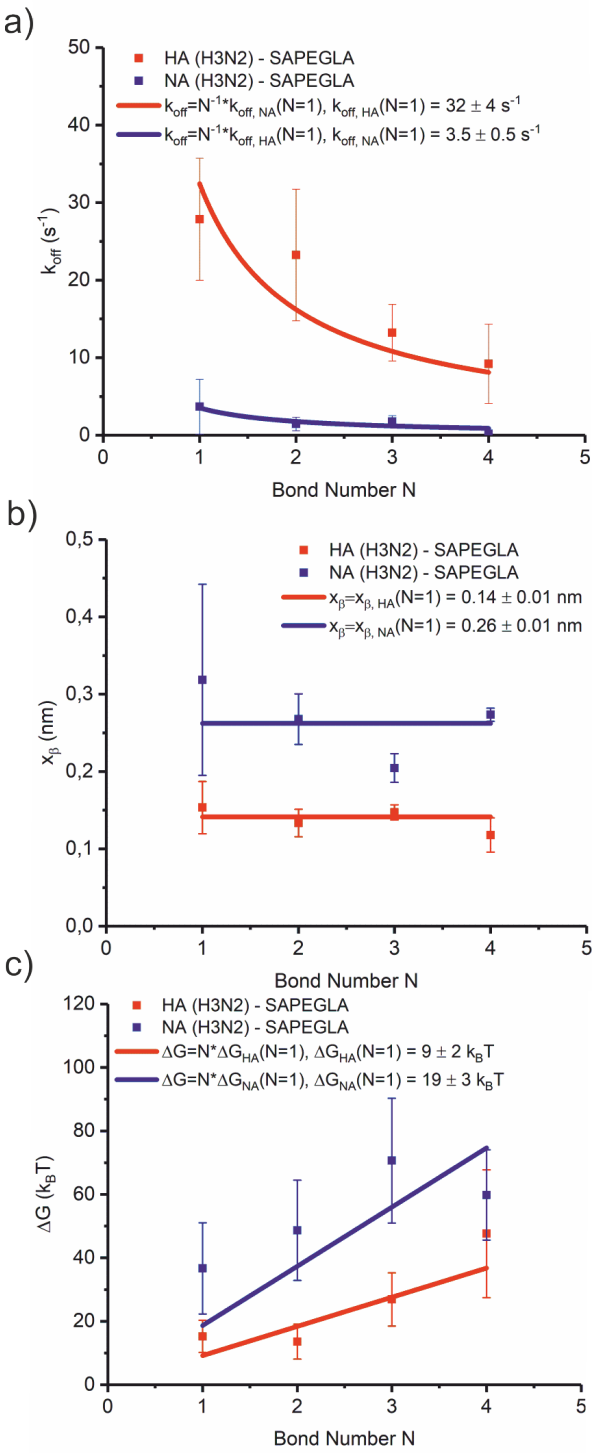

Figure 4.24 – ***Kinetic parameters of HA (H3N2) - SAPEGLA and NA (H3N2) - SAPEGLA with respect to valency:*** *Both proteins show higher stability with increasing bond number. NA (H3N2) is more stable than HA (H3N2), especially for low valency. The solid lines represent fits to data based on the theoretical calculation according to Williams and Evans [129, 188].*

Table 4.7 – ***Thermal force scale, rupture length and dissociation rate of the NA (H3N2) - SAPEGLA interaction after scaling of f_β^{app} with N***

Valency	f_β^{app} pN	f_β nm	x_β s^{-1}	$k_{off}(0)$
1	13 ± 5	13 ± 5	0.32 ± 0.12	4 ± 4
2	31 ± 8	15 ± 4	0.27 ± 0.03	1.4 ± 0.9
3	60 ± 16	20 ± 5	0.20 ± 0.02	1.8 ± 0.8
4	60 ± 7	15 ± 2	0.27 ± 0.01	0.18 ± 0.04

valency is shown. In the case of HA (H3N2) - SAPEGLA, k_{off} is reduced significantly as the bond number increases. The dissociation of a single HA (H3N2) - SAPEGLA bond is about three times faster than the dissociation of four H3-SA bonds. As a consequence of the decrease of k_{off}, the lifetime of the complex, which is the reciprocal of the dissociation rate, $\tau = {k_{off}}^{-1}$, increases with higher bond number. While the lifetime of a single HA (H3N2) - SAPEGLA bond is just $\tau_{N=1}(HA-SA) \approx 0.036s$, the lifetime of a complex of four HA (H3N2) - SAPEGLA bonds is $\tau_{N=4}(HA-SA) \approx 0.11s$. The dissociation rate of the NA (H3N2) - SAPEGLA bond is even more reduced as the valency increases, compared to the dissociation rate of the HA (H3N2) - SAPEGLA bond. A single NA (H3N2) - SAPEGLA bond dissociates approximately 22 times faster than a complex of four NA (H3N2) - SAPEGLA bonds. The higher number of bonds within the complex increases the bond lifetime from $\tau_{N=1}(NA-SA) \approx 0.25s$ to $\tau_{N=4}(NA-SA) \approx 6s$. A similar, but even more extreme, trend was found by Sulchek and colleagues when investigating parallel Mucin1-antibody bonds [186]. The average lifetime of three Mucin1-antibody bonds was about 10^5 times longer than that of a single bond. An analytical expression, *Equation 4.16*, for the decrease of the dissociation rate is given by Williams for the dissociation of truly uncorrelated parallel bonds [188].

$$k_{off}(f,N) = \left[\sum_{n=1}^{N} \frac{1}{n * k_{off}(f=0,N=1)} * \exp\left(-\frac{f}{n * f_\beta}\right)\right]^{-1} \tag{4.16}$$

The dependence of $k_{off}(f=0)$ on N follows immediately and is shown in *Equa-*

tion 4.17.

$$k_{off}(f=0,N) = k_{off}(f=0,N=1) * \left[\sum_{n=1}^{N} \frac{1}{n}\right]^{-1} \tag{4.17}$$

This equation was used to fit the experimental data while keeping the force free dissociation rate of the single bond as the free fit parameter. *Figure 4.24 a)* shows that the fit follows the experimental data well and it holds that $k_{off,HA}(N=1) = 32 \pm 4s^{-1}$ and $k_{off,NA}(N=1) = 3.5 \pm 0.5s^{-1}$. The obtained values for the kinetics of the single bonds are in close agreement with the experimental ones.

In *Figure 4.24 b)* the dependence of the rupture length x_β on the valency is shown. The rupture length seems to be rather constant with a tendency to decrease with N in the case of HA while it does not follow a clear trend in the case of NA. It was reviewed in *chapter 2* that rupture length remains constant if identical bonds are loaded in parallel. This idealized description (*Equation 4.18*) is used to fit the experimental data and x_β is kept as the free parameter.

$$x_\beta(N) = x_\beta(N=1) = constant \tag{4.18}$$

The fit matches both data sets fairly well and it holds that $x_{\beta,HA}(N=1) = 0.26 \pm 0.01nm$ and $x_{\beta,NA}(N=1) = 0.14 \pm 0.01nm$. The fit reproduces the experimentally obtained single bond value well in the case of HA but seems to underestimate x_β in the case of NA. Nevertheless, the values overlap within the experimental precision.

In *Figure 4.24 c)* the dependence of the free energy ΔG on the valency is shown. Overall, the NA (H3N2) - SAPEGLA bonds are characterized by a higher ΔG than the HA (H3N2) - SAPEGLA bonds. An increase of the valency leads to an increase of ΔG. This is in good agreement with the model by Williams and Evans, that assumes a deeper potential well in the case of multiple parallel bonds [129]. In this model, the combined ΔG of N identical bonds is the single bond ΔG multiplied by N and therefore, a linear dependence of $\Delta G(N)$ on N is expected. The experimental data sets are fitted with *Equation 4.19.*

$$\Delta G(N) = N * \Delta G(N=1) \tag{4.19}$$

The fit matches the experimental data reasonably well, but ΔG is underestimated in the case of NA.

Overall, the quantification of the unbinding characteristic of multiple identical bonds provides valuable insight in to the principle of multivalency. Therefore, these results will help to understand the behavior of a multivalent ligand, which will be discussed in the next section. The quantitative data provides approximations for the kinetics of the truly multivalent system and aids in identifying different binding modes.

4.3.2 Multivalent interaction of a Dendritic Ligand

The previous section, *Section 4.3.1*, showed that in general the strength of molecular interaction can increase when the number of receptor-ligand pairs that are loaded simultaneously is increased. This section will focus on the interaction of a multivalent ligand with the influenza virus proteins HA and NA of the type H3N2. The dendritic ligand dPGSA, which was introduced in *chapter 3*, was used as an example of such a multivalent ligand. The ligand was originally designed to match the distances between individual binding pockets of HA on the viral envelope [22]. An enhanced binding strength and reduced dissociation rate is expected when dPGSA binds to more than one ligand binding domain. Due to its design this will be more likely when probing the interaction with HA (H3N2). Conceptual sketches of the different binding modes are depicted in .

dPGSA will bind monovalenly (*Figure 4.25 a)*) when the distance d_{SA} between SA moieties on dPGSA is larger than the distance d_{LBD} between ligand binding domains. Multivalent binding is expected when d_{SA} matches d_{LBD}. This can occur when the ligand binding domains of two neighboring proteins are separated by d_{SA} (*Figure 4.25 b)*) or when intra-protein distances between ligand binding domains match d_{SA} (*Figure 4.25 c)*).

Examples of the force-separation curves that were obtained for the interactions HA (H3N2) - dPGSA or NA (H3N2) - dPGSA and the distributions of rupture forces are shown in *Figure 4.26 a) - d)*. As expected, the rupture forces increase with increasing loading rate. The histograms show the typical distribution of the rupture forces that

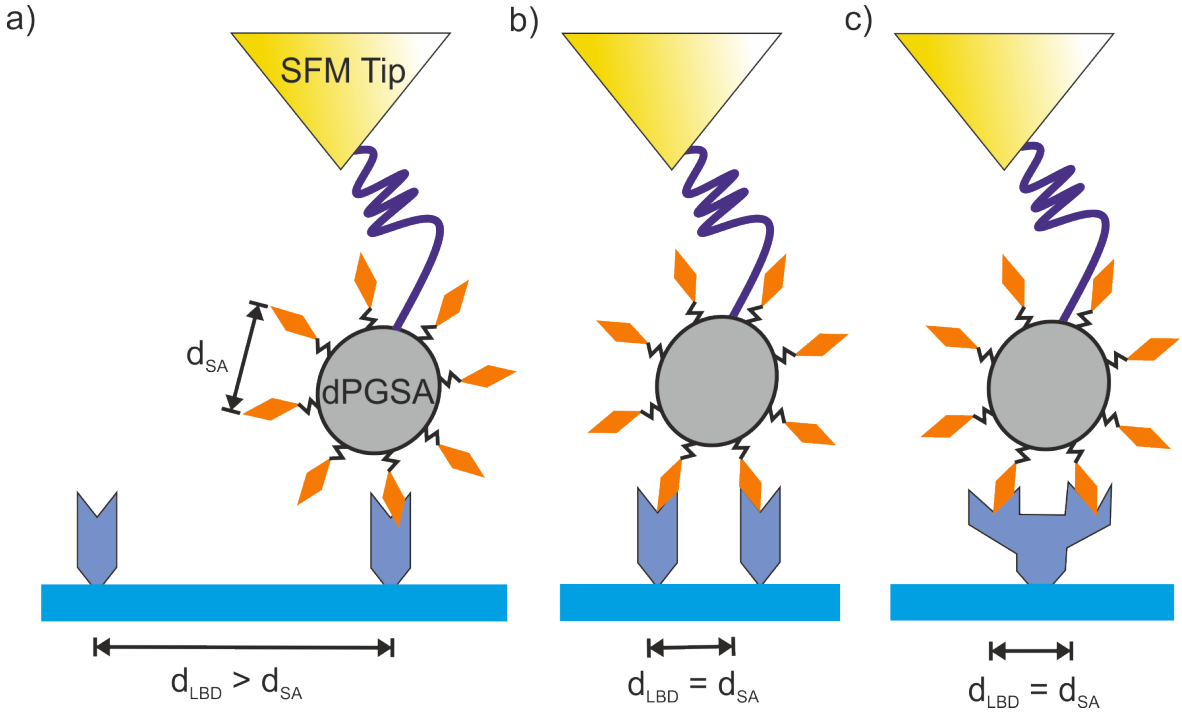

Figure 4.25 – ***Mono- and multivalent binding modes of the dendritic ligand dPGSA:*** *a) The distance d_{SA} between SA moieties does not fit to the distance d_{LBD} between ligand binding domains (LBD) on the surface. Therefore, dPGSA can only bind monovalently and binding kinetics are expected to be similar to those found for SAPEGLA. This can be caused by either the inter- or the intra-protein spacing of the LBD. b) and c) The spacing between LBD matches the spacing of SA moieties on the ligand. Multivalent enhancement of bond stability is expected.*

were already obtained with the ligand SAPEGLA. The distributions feature a high peak at lower forces and a shoulder at higher forces. In analogy to the investigation of SAPEGLA the most probable rupture forces, which are determined by fitting with multi-modal Gaussian functions, are plotted against the most probable loading rates. The resulting force spectra are displayed in *Figure 4.26 e)*. The force spectra overlap to a high degree and show also the non-linear dependence on $\ln\left(\frac{df}{dt}\right)$. From the FNDY model the kinetic parameters are obtained. These parameters are listed in *Table 4.8*.

The equilibrium force determined with the dendritic ligand on HA (H3N2) is higher compared to the equilibrium force that was determined for the interaction of SAPEGLA with HA (H3N2). This results in a higher ΔG of the HA (H3N2) - dPGSA bond. The increased ΔG suggests that the dPGSA binds multivalently to HA (H3N2), as it was

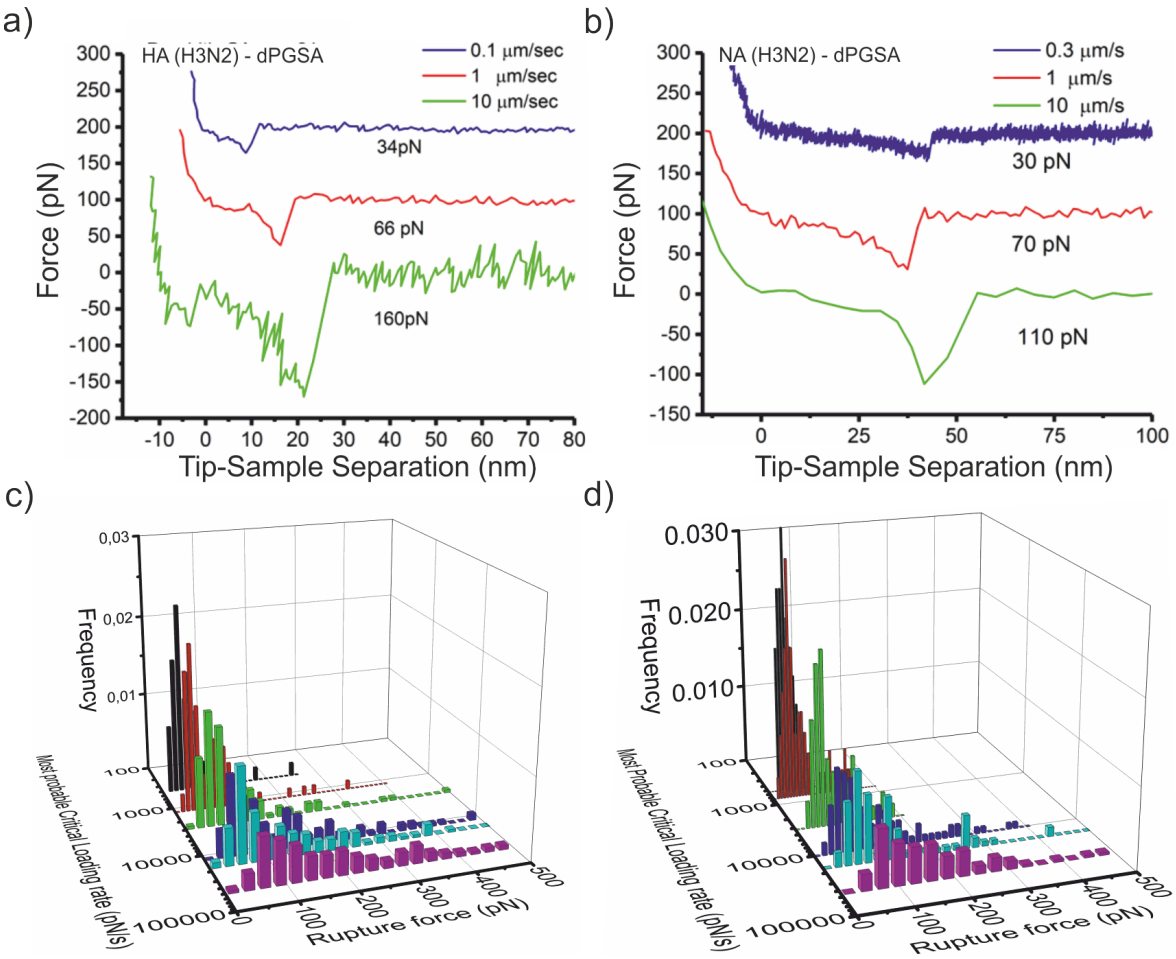

Figure 4.26 – ***Interaction of a dendritic ligand, that is designed to inhibit HA, with H3 and N2:*** *a) and b) force-separation curves are shown that characteristic of the rupture of bonds between the dendritic ligand dPGSA and HA (H3N2) or NA (H3N2). The curves are horizontally offset for clarity. c) and d) The rupture forces of the HA (H3N2) - dPGSA and NA (H3N2) - dPGSA unbinding show a distinctive peak and increase with increasing loading rate. (Parts of the image were provided by Dr. Jose Luis Cuellar-Camacho.)*

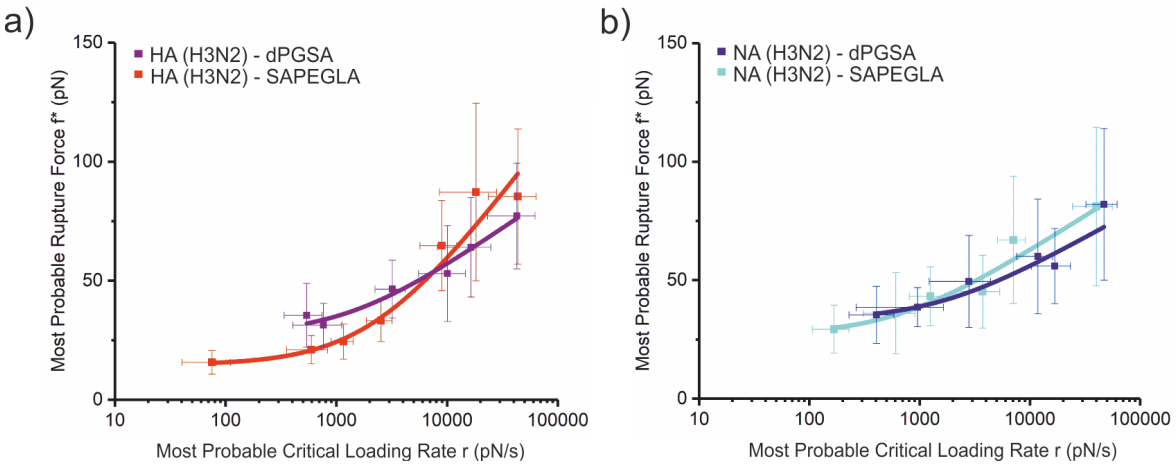

Figure 4.27 – ***DFS of the interaction of the dendritic ligand dPGSA compared to those of SAPEGLA:*** *a) The figure shows the DFS of the dPGSA-HA (H3N2) interaction together with the DFS of the SAPEGLA-HA (H3N2) interaction. The DFS of the dPGSA-HA (H3N2) interaction tends to a higher f_{eq} in the equilibrium regime.*

originally intended. The equilibrium force that was determined for the NA (H3N2) - dPGSA bond is similar to the one determined with SAPEGLA and therefore ΔG is also within the same range. This suggests, that the dendritic ligand binds only monovalently and cannot bridge individual N2 proteins on the NTA-surface. This is supported by the inter-protein distances that were measured in *Section 4.1.* A complete picture of the kinetic parameters is displayed in *Figure 4.28* relative to the kinetics of SAPEGLA. It shows that the dissociation rate of HA (H3N2) - dPGSA is significantly higher than that of a single HA (H3N2) - SAPEGLA bond. In fact, the dissociation rate of the multivalent ligand $k_{off}^{HA(H3N2)-dPGSA} = 8 \pm 8$ is within the range of three to four combined single bonds. The rupture length is also increased by factor of two to three. Interestingly, the dissociation rate and rupture length of HA (H3N2) dPGSA are close to those determined for NA (H3N2) - SAPEGLA. This result emphasizes the importance of a tuned balance of HA and NA kinetics for viral fitness. The energy barrier ΔG of the bonds is shown in *Figure 4.28 b).* ΔG is higher in the case of the dendritic ligand binding to HA compared to ΔG of the single bond interaction albeit it is only in the range of two connections.

Table 4.8 – ***Kinetic parameters of dissociation of the dendritic ligand, extracted from the DFS data by application of the FNDY model, as seen in Figure 4.27.***

Protein	f_{eq} pN	f_β pN	$k_{off}\,(f_{eq})$ s^{-1}	k^0_{off} s^{-1}	x_β nm	ΔG k_BT
HA (H3N2)	27 ± 5	14 ± 5	54 ± 52	8 ± 8	0.3 ± 0.1	23 ± 10
NA (H3N2)	33 ± 6	11 ± 7	77 ± 120	5 ± 7	0.4 ± 0.2	35 ± 13

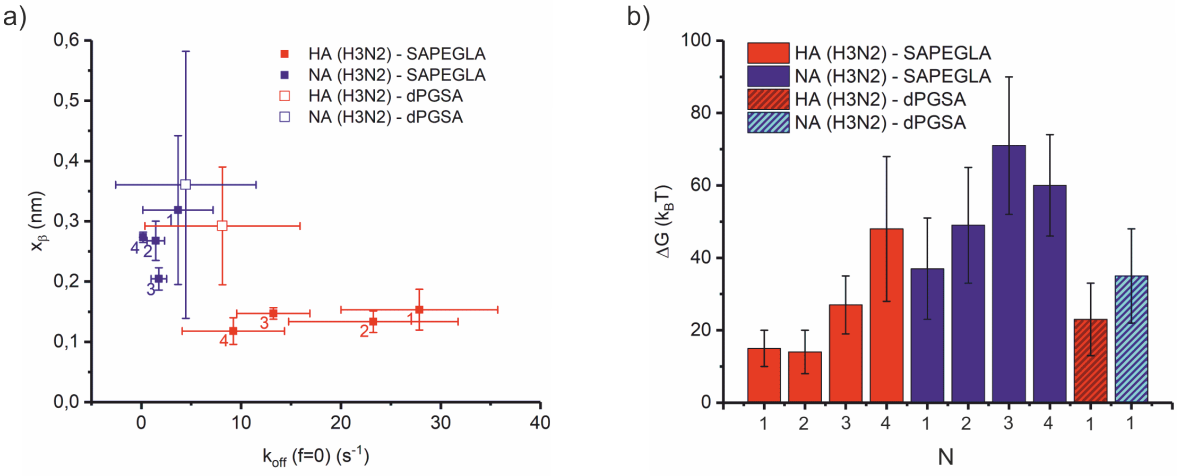

Figure 4.28 – ***Comparison of k_{off}, x_β and ΔG for the interactions of SAPEGLA and PGSA with HA and HA of the type (H3N2):*** *a) x_β is plotted relative to k_{off}. b) ΔG is depicted.*

4.4 Influence on Viral Infectivity and Transmissibility

The preceding sections, especially *Section 4.2.2* and *Section 4.3.1*, were focused on the physics of molecular interaction and on the extraction of the characteristic kinetic parameters. This section will now analyze and interpret the findings in a more biological context. When the rates of association and dissociation as well as the energy landscapes that are characteristic for the protein-ligand complexes are compared with the dynamics of the natural interaction for the influenza virus virion with cells it must not be forgotten that the force spectra are the result of rather artificial experimental systems. Even though the kinetics of the protein-ligand interactions that were determined in this study might deviate from in-vivo experiments valuable qualitative insight into the complex dynamics of biological systems can be gained.

In general, the force spectra that were experimentally determined using the monovalent ligand SAPEGLA showed that the dissociation of a single the HA-SA bond was typically faster than that of a NA-SA bond. This held true for both viral strains that were examined. Hence, the SA binds stronger to NA than to HA at least in the case of H1N1 and H3N2. The superior binding strength of the NA might be necessary to compensate the small number of NA relative to HA. It also correlates well with recent studies that indicate a contribution of NA in the initial adhesion to epithelial cells [191, 192]. A complete overview of the monovalent interaction of the proteins of the two different viral strains is given in *Figure 4.29*

Furthermore, it must not be forgotten that the NA possesses enzymatic activity [70, 193, 72]. The enzymatic activity allows the NA to cleave terminal SA from glycoconjugates, which is still considered the primary function of NA [70]. Hence, the stability of an NA-SA bond must be considered with respect to the rate of enzymatic cleavage. The capability to cleave SA did not have an effect in the force spectroscopy, since the PEG-tether structure is not accessible to the enzymatic activity of the NA [194]. A measure for the rate of enzymatic activity is k_{cat} alongside the Michaelis-Menten constant K_m. Several biochemical studies have characterized the enzymatic activity

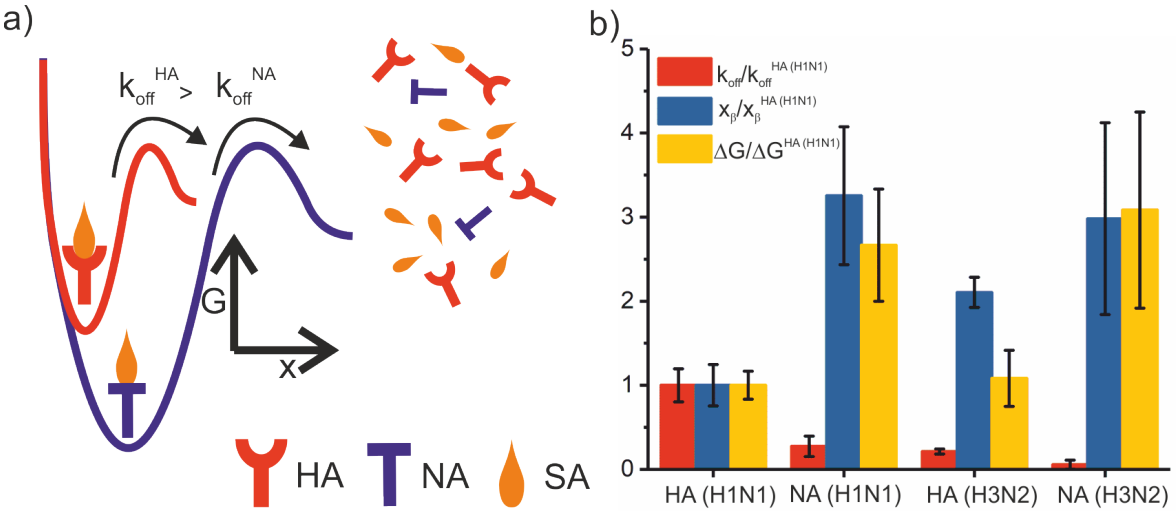

Figure 4.29 – ***Comparison of the kinetic parameters*** k_{off}, x_β ***and*** ΔG ***determined for the different viral strains H1N1 and H3N2:*** *a) The image shows a generalized sketch of the energy landscapes of HA and NA. NA features a deeper and broader potential well. Therefore, it holds that:* ${k_{off}}^{HA} > {k_{off}}^{NA}$. *b) The kinetic parameters* k_{off}, x_β *and* ΔG *are displayed for the monovalent interaction of the different proteins. All quantities are given relative to the values determined for HA (H1N1). Both strains have in common that SA dissociates faster from HA than NA. HA (H3N2) and NA (H3N2) show stronger binding compared to HA (H1N1) and NA (H1N1).* x_β *is similar in the case of NA (H1N1) and NA (H3N2) and also to a lesser degree in the case of HA (H3N2).* ΔG *of NA (H1N1) is close to that of NA (H3N2) and* ΔG *of HA (H1N1) is close to that of HA (H3N2).*

and allow a comparison to the kinetics determined with force spectroscopy [191, 195]. For further considerations the values of k_{cat} and K_m that were measured by Xu and colleagues for H1N1 on the artificial substrate $4-MU-NANA$ will be used exemplary. In this study it was found that $k_{cat} = 3.17 \pm 0.1 s^{-1}$ and $K_m = 373 \pm 8 \mu M$ [195]. The value for k_{cat} is related to an average timescale τ_{cat} for cleaving one SA from its linkage. It holds, that $\tau_{cat} = {k_{cat}}^{-1} \approx 0.3 s$. Association rates k_{on} of ligands to the active site of NA can be obtained from the study by Sung and colleagues [92]. In the case of SA binding to NA of the type H1N1 it holds that $k_{on} \approx 0.17 \mu M$. The relation between k_{cat}, K_m, k_{on} and k_{off} is given in *Equation 4.20* [191].

$$k_{off} = K_m k_{on} - k_{cat} \tag{4.20}$$

From *Equation 4.20* it follows, that $k_{off} = 60s^{-1}$, which corresponds to a bond lifetime $\tau_{off} \approx 0.02s$. This is in good agreement to the results from SMFS where an average bond life time $\tau_{off} = 0.06s$ had been determined for NA. This clearly demonstrates that force spectroscopy using synthetic ligands can adequately characterize kinetics of biological processes. It also follows from these consideration, that the probability of dissociation of SA from an active site of NA is about 6 times higher than that of enzymatic cleavage [160]. Therefore, multiple SA-NA interactions are needed for efficient cleavage of SA.

Chapter 5

Conclusions and Perspectives

Mono- and multivalent bonds of HA and NA of the type H1N1 and H3N2 with SA were individually quantified on the single molecule level using SMFS and the bond strength was found to be between $10 - 100pN$ for single bonds.

The dynamic force spectra of the protein-ligand bonds did not show the log-linear trend predicted by the classical KBE model, which is most commonly applied in SMFS. It was concluded that the more recent FNDY model is better suited to extract the dissociation rate and the shape of the free energy landscape from the dynamic force spectra. In this description, the shallower slope at low loading rates is caused by rebinding effects that inhibit the measurements of lower forces than the equilibrium force, which is related to the free energy difference between the bound and unbound state.

It was found, independently of the viral strain, that, despite similar unbinding forces, the single HA-SA bond dissociates in the case of type H1N1 at an approximately three times faster rate than the NA-SA bond while the single HA-SA bond of the type H3N2 showed an seven times faster dissociation rate than the NA-SA bond of the same strain. Furthermore, NA-SA bonds are characterized by a deeper and wider free energy landscape. These results highlight the importance of NA for viral attachment to epithelial cells, which has recently drawn much attention. It is reasoned that the higher stability compensates the smaller amount of neuraminidase on the viral envelope, compared to hemagglutinin. Without sufficient neuraminidase binding, the virus would suffer from a lack of siliac acid cleavage and remain stuck in the mucus or at the cell

membrane.

The bond strength of a cluster of monovalent ligands increased as expected with the number of bonds in the cluster and followed the theoretical predictions. This allowed to obtain a glimpse at the expectable strength of the multivalent ligand.

It was also found that, at least for the type H1N1, the dissociation rate of a single NA-SA bond is on the order of, but still faster than, the catalytic rate of neuraminidase, which can be seen as the average time for cleavage of a single sialic acid. This correlates well with the fact that monomeric NA lacks enzymatic activity and therefore multiple attachments are needed for SA cleavage. Therefore, the patched arrangement of neuraminidase on the viral envelope is a requirement as it locally increases the rate of sialic acid cleavage and leads to higher viral motility.

The comparison of the unbinding kinetics between the types H1N1 to H3N2 showed that the stability of the HA-SA and NA-SA bonds is higher in the case of H3N2. Interestingly, the the dissociation rate and width of the energy landscape of NA of the type H1N1 were found to be close to those found for both proteins of the type H3N2. It is suggested that the pandemic type of the influenza virus, which features the H1N1 proteins, is less prone to adhering to the membranes of the host cell or the mucus. This might be a requirement for the virion to adjust to the structurally different presentations of SA on the cell membranes of different hosts. Whether this is also true for other strains of the influenza virus may be investigated in further studies.

The dendritic ligand, which had been designed to match the spacing of ligand binding domains of the HA, showed higher thermal stability on HA (H3N2) than its monovalent counterpart and the dissociation rate was found to be on the order of three to four monovalent ligands. This comes as a surprise, since it was shown in earlier studies by Bhatia and colleagues that the functional endgroup of the multivalent ligand most likely binds only two to three ligand binding domains [22]. Hence, it is assured that the multivalent ligand interacts cooperatively. This was not the case on NA (H3N2) and therefore the quantitative data illustrates that the enhancement of the binding strength due to multivalent effects is not always favored through the simple increase in active groups that are presented by the ligand. It is more likely that an optimized interplay of numbers, geometry and flexibility is required to strengthen a biomolecular

interaction.

Future research should focus on the characterization of the interaction potential of further ligands, that will be designed to inhibit the IAV by binding to HA and NA. In this sense, SFM based SMFS could be used as an inhibitory assay as it was done in this thesis to prove the specificity of the unbinding events. Once well-defined arrays of proteins or other biomolecules have been created, the strength and affinity of various ligands can be probed with the SFM at high throughput rates. Upcoming studies should also focus on the differences in binding kinetics between proteins of different viral strains, since this can contribute to understanding the mechanisms of viral transmissibility and drug resistance. This knowledge could then be used to quantify mechanical properties of other biomolecules with high spatial precision, which will support medical research and contribute to tackling the challenges posed by infectious diseases.

Bibliography

[1] B. Nagel, H. Dellweg, and L. M. Gierasch. Glossary for chemists of terms used in biotechnology (IUPAC recommendations 1992). *Pure and Applied Chemistry*, 64 (1):143–168, jan 1992. doi:10.1351/pac199264010143.

[2] Michel Vert, Yoshiharu Doi, Karl-Heinz Hellwich, Michael Hess, Philip Hodge, Przemyslaw Kubisa, Marguerite Rinaudo, and François Schué. Terminology for biorelated polymers and applications (IUPAC recommendations 2012). *Pure and Applied Chemistry*, 84(2):377–410, jan 2012. doi:10.1351/pac-rec-10-12-04.

[3] Johan R C van der Maarel. *Introduction to Biopolymer Physics*. WORLD SCIENTIFIC, dec 2007. doi:10.1142/6644.

[4] Tom A. Rapoport. Protein translocation across the eukaryotic endoplasmic reticulum and bacterial plasma membranes. *Nature*, 450(7170):663–669, nov 2007. doi:10.1038/nature06384.

[5] Mingming Su, Yunchao Ling, Jun Yu, Jiayan Wu, and Jingfa Xiao. Small proteins: untapped area of potential biological importance. *Frontiers in Genetics*, 4, 2013. doi:10.3389/fgene.2013.00286.

[6] Logan C. Meyer and Nathan T. Wright. Structure of giant muscle proteins. *Frontiers in Physiology*, 4, 2013. doi:10.3389/fphys.2013.00368.

[7] A. E. Mirsky and L. Pauling. On the structure of native, denatured, and coagulated proteins. *Proceedings of the National Academy of Sciences*, 22(7):439–447, jul 1936. doi:10.1073/pnas.22.7.439.

[8] J. D. BERNAL. Structure of proteins. *Nature*, 143(3625):663–667, apr 1939. doi:10.1038/143663a0.

[9] C. Nick Pace, J. Martin Scholtz, and Gerald R. Grimsley. Forces stabilizing proteins. *FEBS Letters*, 588(14):2177–2184, may 2014. doi:10.1016/j.febslet.2014.05.006.

[10] Julie Ménétrey, Amel Bahloul, Amber L. Wells, Christopher M. Yengo, Carl A. Morris, H. Lee Sweeney, and Anne Houdusse. The structure of the myosin VI motor reveals the mechanism of directionality reversal. *Nature*, 435(7043):779–785, jun 2005. doi:10.1038/nature03592.

[11] George M. Whitesides and Vijay M. Krishnamurthy. Designing ligands to bind proteins. *Quarterly Reviews of Biophysics*, 38(04):385, nov 2005. doi:10.1017/s0033583506004240.

[12] H. Ekkehard Neuhaus. Transport of primary metabolites across the plant vacuolar membrane. *FEBS Letters*, 581(12):2223–2226, feb 2007. doi:10.1016/j.febslet.2007.02.003.

[13] Chiara Speziale, Livia Salvati Manni, Cristina Manatschal, Ehud M. Landau, and Raffaele Mezzenga. A macroscopic h+ and cl-ions pump via reconstitution of EcClC membrane proteins in lipidic cubic mesophases. *Proceedings of the National Academy of Sciences*, 113(27):7491–7496, jun 2016. doi:10.1073/pnas.1603965113.

[14] Mathai Mammen, Seok-Ki Choi, and George M. Whitesides. Polyvalent interactions in biological systems: Implications for design and use of multivalent ligands and inhibitors. *Angewandte Chemie International Edition*, 37(20):2754–2794, nov 1998. doi:10.1002/(sici)1521-3773(19981102)37:20<2754::aid-anie2754>3.0.co;2-3.

[15] Carlo Fasting, Christoph A. Schalley, Marcus Weber, Oliver Seitz, Stefan Hecht, Beate Koksch, Jens Dernedde, Christina Graf, Ernst-Walter Knapp, and Rainer Haag. Multivalency as a chemical organization and action principle. *Angewandte Chemie International Edition*, 51(42):10472–10498, sep 2012. doi:10.1002/anie.201201114.

[16] Steeve Boulant, Megan Stanifer, and Pierre-Yves Lozach. Dynamics of virus-receptor interactions in virus binding, signaling, and endocytosis. *Viruses*, 7(6): 2794 – 2815, jun 2015. doi:10.3390/v7062747.

[17] L. PAULING and M. DELBRUCK. THE NATURE OF THE INTERMOLECULAR FORCES OPERATIVE IN BIOLOGICAL PROCESSES. *Science*, 92(2378): 77–79, jul 1940. doi:10.1126/science.92.2378.77.

[18] Stephen C Harrison. Viral membrane fusion. *Nature Structural & Molecular Biology*, 15(7):690–698, jul 2008. doi:10.1038/nsmb.1456.

[19] Stephan Block, Vladimir P. Zhdanov, and Fredrik Höök. Quantification of multivalent interactions by tracking single biological nanoparticle mobility on a lipid membrane. *Nano Letters*, 16(7):4382–4390, jun 2016. doi:10.1021/acs.nanolett.6b01511.

[20] Ilona Papp, Christian Sieben, Kai Ludwig, Meike Roskamp, Christoph Böttcher, Sabine Schlecht, Andreas Herrmann, and Rainer Haag. Inhibition of influenza virus infection by multivalent sialic-acid-functionalized gold nanoparticles. *Small*, 6(24):2900–2906, nov 2010. doi:10.1002/smll.201001349.

[21] Ilona Papp, Christian Sieben, Adam L. Sisson, Johanna Kostka, Christoph Böttcher, Kai Ludwig, Andreas Herrmann, and Rainer Haag. Inhibition of influenza virus activity by multivalent glycoarchitectures with matched sizes. *ChemBioChem*, 12(6):887–895, mar 2011. doi:10.1002/cbic.201000776.

[22] Sumati Bhatia, Daniel Lauster, Markus Bardua, Kai Ludwig, Stefano Angioletti-Uberti, Nicole Popp, Ute Hoffmann, Florian Paulus, Matthias Budt, Marlena Stadtmüller, Thorsten Wolff, Alf Hamann, Christoph Böttcher, Andreas Herrmann, and Rainer Haag. Linear polysialoside outperforms dendritic analogs for inhibition of influenza virus infection in vitro and in vivo. *Biomaterials*, 138: 22–34, sep 2017. doi:10.1016/j.biomaterials.2017.05.028.

[23] Nicholas K. Sauter, Mark D. Bednarski, Beth A. Wurzburg, John E. Hanson, George M. Whitesides, John J. Skehel, and Don C. Wiley. Hemagglutinins from two influenza virus variants bind to sialic acid derivatives with millimolar

dissociation constants: a 500-MHz proton nuclear magnetic resonance study. *Biochemistry*, 28(21):8388–8396, oct 1989. doi:10.1021/bi00447a018.

[24] Chi-Hao Luan, Timothy M. Parker, Kari U. Prasad, and Dan W. Urry. Differential scanning calorimetry studies of NaCl effect on the inverse temperature transition of some elastin-based polytetra-, polypenta-, and polynonapeptides. *Biopolymers*, 31(5):465–475, apr 1991. doi:10.1002/bip.360310502.

[25] John E. Hanson, Nicholas K. Sauter, John J. Skehel, and Don C. Wiley. Proton nuclear magnetic resonance studies of the binding of sialosides to intact influenza virus. *Virology*, 189(2):525–533, aug 1992. doi:10.1016/0042-6822(92)90576-b.

[26] *Solid State NMR Spectroscopy for Biopolymers*. Kluwer Academic Publishers, 2006. doi:10.1007/1-4020-4303-1.

[27] Andrew L. Feig. Applications of isothermal titration calorimetry in RNA biochemistry and biophysics. *Biopolymers*, 87(5-6):293–301, 2007. doi:10.1002/bip.20816.

[28] Matthew W. Freyer and Edwin A. Lewis. Isothermal titration calorimetry: Experimental design, data analysis, and probing macromolecule/ligand binding and kinetic interactions. In *Biophysical Tools for Biologists, Volume One: In Vitro Techniques*, pages 79–113. Elsevier, 2008. doi:10.1016/s0091-679x(07)84004-0.

[29] Daniel Lauster, Maria Glanz, Markus Bardua, Kai Ludwig, Markus Hellmund, Ute Hoffmann, Alf Hamann, Christoph Böttcher, Rainer Haag, Christian P. R. Hackenberger, and Andreas Herrmann. Multivalent peptide-nanoparticle conjugates for influenza-virus inhibition. *Angewandte Chemie International Edition*, 56(21):5931–5936, apr 2017. doi:10.1002/anie.201702005.

[30] Vanessa Bertolino, Giuseppe Cavallaro, Stefana Milioto, Filippo Parisi, and Giuseppe Lazzara. Thermal properties of multilayer nanocomposites based on halloysite nanotubes and biopolymers. *Journal of Composites Science*, 2(3):41, jul 2018. doi:10.3390/jcs2030041.

[31] Svenja Ehrmann, Chih-Wei Chu, Shalini Kumari, Kim Silberreis, Christoph Böttcher, Jens Dernedde, Bart Jan Ravoo, and Rainer Haag. A toolbox

approach for multivalent presentation of ligand–receptor recognition on a supramolecular scaffold. *Journal of Materials Chemistry B*, 6(25):4216–4222, 2018. doi:10.1039/c8tb00922h.

[32] Evan Evans. Probing the relation between force—lifetime—and chemistry in single molecular bonds. *Annual Review of Biophysics and Biomolecular Structure*, 30(1):105–128, jun 2001. doi:10.1146/annurev.biophys.30.1.105.

[33] Alexander Fuhrmann, Jan C. Schoening, Dario Anselmetti, Dorothee Staiger, and Robert Ros. Quantitative analysis of single-molecule RNA-protein interaction. *Biophysical Journal*, 96(12):5030–5039, jun 2009. doi:10.1016/j.bpj.2009.03.022.

[34] Rainer Eckel, Robert Ros, Björn Decker, Jochen Mattay, and Dario Anselmetti. Supramolecular chemistry at the single-molecule level. *Angewandte Chemie International Edition*, 44(3):484–488, jan 2005. doi:10.1002/anie.200461382.

[35] G. Bell. Models for the specific adhesion of cells to cells. *Science*, 200(4342): 618–627, may 1978. doi:10.1126/science.347575.

[36] Matthias Rief and Helmut Grubmüller. Force spectroscopy of single biomolecules. *ChemPhysChem*, 3(3):255, mar 2002. doi:10.1002/1439-7641(20020315)3:3<255::aid-cphc255>3.0.co;2-m.

[37] Christoph Gerber and Hans Peter Lang. How the doors to the nanoworld were opened. *Nature Nanotechnology*, 1(1):3–5, oct 2006. doi:10.1038/nnano.2006.70.

[38] Stewart R. Durell and Arieh Ben-Naim. Hydrophobic-hydrophilic forces in protein folding. *Biopolymers*, 107(8):e23020, jun 2017. doi:10.1002/bip.23020.

[39] G. Binnig, C. F. Quate, and Ch. Gerber. Atomic force microscope. *Physical Review Letters*, 56(9):930–933, mar 1986. doi:10.1103/physrevlett.56.930.

[40] David Alsteens, Hermann E. Gaub, Richard Newton, Moritz Pfreundschuh, Christoph Gerber, and Daniel J. Müller. Atomic force microscopy-based characterization and design of biointerfaces. *Nature Reviews Materials*, 2(5):17008, mar 2017. doi:10.1038/natrevmats.2017.8.

[41] Andreas Engel and Daniel J. Müller. Observing single biomolecules at work with the atomic force microscope. *Nature Structural Biology*, 7(9):715–718, sep 2000. doi:10.1038/78929.

[42] F. Schwesinger, R. Ros, T. Strunz, D. Anselmetti, H.-J. Guntherodt, A. Honegger, L. Jermutus, L. Tiefenauer, and A. Pluckthun. Unbinding forces of single antibody-antigen complexes correlate with their thermal dissociation rates. *Proceedings of the National Academy of Sciences*, 97(18):9972–9977, aug 2000. doi:10.1073/pnas.97.18.9972.

[43] Markus Ritzefeld, Volker Walhorn, Dario Anselmetti, and Norbert Sewald. Analysis of DNA interactions using single-molecule force spectroscopy. *Amino Acids*, 44(6):1457–1475, mar 2013. doi:10.1007/s00726-013-1474-4.

[44] Xavier Sisquella, Karel de Pourcq, Javier Alguacil, Jordi Robles, Fausto Sanz, Dario Anselmetti, Santiago Imperial, and Xavier Fernandez-Busquets. A single-molecule force spectroscopy nanosensor for the identification of new antibiotics and antimalarials. *The FASEB Journal*, 24(11):4203–4217, nov 2010. doi:10.1096/fj.10-155507.

[45] Philip A. Gale and Jonathan W. Steed, editors. *Supramolecular Chemistry*. John Wiley & Sons, Ltd, mar 2012. doi:10.1002/9780470661345.

[46] András Perl, Alberto Gomez-Casado, Damien Thompson, Henk H. Dam, Pascal Jonkheijm, David N. Reinhoudt, and Jurriaan Huskens. Gradient-driven motion of multivalent ligand molecules along a surface functionalized with multiple receptors. *Nature Chemistry*, 3(4):317–322, mar 2011. doi:10.1038/nchem.1005.

[47] Matt McKenzie, Sung Min Ha, Aravind Rammohan, Ravi Radhakrishnan, and N. Ramakrishnan. Multivalent binding of a ligand-coated particle: Role of shape, size, and ligand heterogeneity. *Biophysical Journal*, 114(8):1830–1846, apr 2018. doi:10.1016/j.bpj.2018.03.007.

[48] Xing Du, Yi Li, Yuan-Ling Xia, Shi-Meng Ai, Jing Liang, Peng Sang, Xing-Lai Ji, and Shu-Qun Liu. Insights into protein–ligand interactions: Mechanisms, models,

and methods. *International Journal of Molecular Sciences*, 17(2):144, jan 2016. doi:10.3390/ijms17020144.

[49] Susanne Liese and Roland R Netz. Influence of length and flexibility of spacers on the binding affinity of divalent ligands. *Beilstein Journal of Organic Chemistry*, 11:804–816, may 2015. doi:10.3762/bjoc.11.90.

[50] Volker Walhorn, Ann-Kristin Möller, Christian Bartz, Thomas Dierks, and Dario Anselmetti. Exploring the sulfatase 1 catch bond free energy landscape using jarzynski's equality. *Scientific Reports*, 8(1), nov 2018. doi:10.1038/s41598-018-35120-0.

[51] Eva Maria Munoz, Juan Correa, Ricardo Riguera, and Eduardo Fernandez-Megia. Real-time evaluation of binding mechanisms in multivalent interactions: A surface plasmon resonance kinetic approach. *Journal of the American Chemical Society*, 135(16):5966–5969, apr 2013. doi:10.1021/ja400951g.

[52] Patrick A. Alexander, Yanan He, Yihong Chen, John Orban, and Philip N. Bryan. A minimal sequence code for switching protein structure and function. *Proceedings of the National Academy of Sciences*, 106(50):21149–21154, nov 2009. doi:10.1073/pnas.0906408106.

[53] Christopher M. Dobson. Protein folding and misfolding. *Nature*, 426(6968): 884–890, dec 2003. doi:10.1038/nature02261.

[54] G. P. Moss, P. A. S. Smith, and D. Tavernier. Glossary of class names of organic compounds and reactivity intermediates based on structure (IUPAC recommendations 1995). *Pure and Applied Chemistry*, 67(8-9):1307–1375, jan 1995. doi:10.1351/pac199567081307.

[55] L. Pauling, R. B. Corey, and H. R. Branson. The structure of proteins: Two hydrogen-bonded helical configurations of the polypeptide chain. *Proceedings of the National Academy of Sciences*, 37(4):205–211, apr 1951. doi:10.1073/pnas.37.4.205.

[56] C. B. Anfinsen. Principles that govern the folding of protein chains. *Science*, 181 (4096):223–230, jul 1973. doi:10.1126/science.181.4096.223.

[57] Joseph Feher. Protein structure. In *Quantitative Human Physiology*, pages 130–141. Elsevier, 2017. doi:10.1016/b978-0-12-800883-6.00012-4.

[58] Matthias Rief, Mathias Gautel, Filipp Oesterhelt, Julio M. Fernandez, and Hermann E. Gaub. Reversible unfolding of individual titin immunoglobulin domains by AFM. *Science*, 276(5315):1109–1112, may 1997. doi:10.1126/science.276.5315.1109.

[59] L Simonsen, M J Clarke, G D Williamson, D F Stroup, N H Arden, and L B Schonberger. The impact of influenza epidemics on mortality: introducing a severity index. *American Journal of Public Health*, 87(12):1944–1950, dec 1997. doi:10.2105/ajph.87.12.1944.

[60] Mark von Itzstein. The war against influenza: discovery and development of sialidase inhibitors. *Nature Reviews Drug Discovery*, 6(12):967–974, dec 2007. doi:10.1038/nrd2400.

[61] Florian Krammer, Gavin J. D. Smith, Ron A. M. Fouchier, Malik Peiris, Katherine Kedzierska, Peter C. Doherty, Peter Palese, Megan L. Shaw, John Treanor, Robert G. Webster, and Adolfo García-Sastre. Influenza. *Nature Reviews Disease Primers*, 4(1), jun 2018. doi:10.1038/s41572-018-0002-y.

[62] Debi P. Nayak, Rilwan A. Balogun, Hiroshi Yamada, Z. Hong Zhou, and Subrata Barman. Influenza virus morphogenesis and budding. *Virus Research*, 143(2): 147–161, aug 2009. doi:10.1016/j.virusres.2009.05.010.

[63] Nicole M. Bouvier and Peter Palese. The biology of influenza viruses. *Vaccine*, 26:D49–D53, sep 2008. doi:10.1016/j.vaccine.2008.07.039.

[64] Susanne Herold, Christin Becker, Karen M. Ridge, and G.R. Scott Budinger. Influenza virus-induced lung injury: pathogenesis and implications for treatment. *European Respiratory Journal*, 45(5):1463–1478, mar 2015. doi:10.1183/09031936.00186214.

[65] Sebastian Wasilewski, Lesley J. Calder, Tim Grant, and Peter B. Rosenthal. Distribution of surface glycoproteins on influenza a virus deter-

mined by electron cryotomography. *Vaccine*, 30(51):7368–7373, dec 2012. doi:10.1016/j.vaccine.2012.09.082.

[66] A. Harris, G. Cardone, D. C. Winkler, J. B. Heymann, M. Brecher, J. M. White, and A. C. Steven. Influenza virus pleiomorphy characterized by cryoelectron tomography. *Proceedings of the National Academy of Sciences*, 103(50):19123–19127, dec 2006. doi:10.1073/pnas.0607614103.

[67] Melike Lakadamyali, Michael J. Rust, and Xiaowei Zhuang. Endocytosis of influenza viruses. *Microbes and Infection*, 6(10):929–936, aug 2004. doi:10.1016/j.micinf.2004.05.002.

[68] Steven J. Gamblin and John J. Skehel. Influenza hemagglutinin and neuraminidase membrane glycoproteins. *Journal of Biological Chemistry*, 285(37):28403–28409, jun 2010. doi:10.1074/jbc.r110.129809.

[69] C. Sieben, C. Kappel, R. Zhu, A. Wozniak, C. Rankl, P. Hinterdorfer, H. Grubmuller, and A. Herrmann. Influenza virus binds its host cell using multiple dynamic interactions. *Proceedings of the National Academy of Sciences*, 109(34): 13626–13631, aug 2012. doi:10.1073/pnas.1120265109.

[70] Jean-Michel Garcia, Jimmy C. C. Lai, Thomas Haselhorst, Ka Tim Choy, Hui-Ling Yen, Joseph S. M. Peiris, Mark von Itzstein, and John M. Nicholls. Investigation of the binding and cleavage characteristics of n1 neuraminidases from avian, seasonal, and pandemic influenza viruses using saturation transfer difference nuclear magnetic resonance. *Influenza and Other Respiratory Viruses*, 8(2): 235–242, sep 2013. doi:10.1111/irv.12184.

[71] Peter Palese, Kiyotake Tobita, Masahiro Ueda, and Richard W. Compans. Characterization of temperature sensitive influenza virus mutants defective in neuraminidase. *Virology*, 61(2):397–410, oct 1974. doi:10.1016/0042-6822(74)90276-1.

[72] Julie L. McAuley, Brad P. Gilbertson, Sanja Trifkovic, Lorena E. Brown, and Jennifer L. McKimm-Breschkin. Influenza virus neuraminidase structure and functions. *Frontiers in Microbiology*, 10, jan 2019. doi:10.3389/fmicb.2019.00039.

[73] Ralf Wagner, Mikhail Matrosovich, and Hans-Dieter Klenk. Functional balance between haemagglutinin and neuraminidase in influenza virus infections. *Reviews in Medical Virology*, 12(3):159–166, 2002. doi:10.1002/rmv.352.

[74] A. Gaymard, N. Le Briand, E. Frobert, B. Lina, and V. Escuret. Functional balance between neuraminidase and haemagglutinin in influenza viruses. *Clinical Microbiology and Infection*, 22(12):975–983, dec 2016. doi:10.1016/j.cmi.2016.07.007.

[75] Matthias Müller, Daniel Lauster, Helen H. K. Wildenauer, Andreas Herrmann, and Stephan Block. Mobility-based quantification of multivalent virus-receptor interactions: New insights into influenza a virus binding mode. *Nano Letters*, 19 (3):1875–1882, feb 2019. doi:10.1021/acs.nanolett.8b04969.

[76] Jimmy Chun Cheong Lai, Herath M. T. K. Karunarathna, Ho Him Wong, Joseph S. M. Peiris, and John M. Nicholls. Neuraminidase activity and specificity of influenza a virus are influenced by haemagglutinin-receptor binding. *Emerging Microbes & Infections*, 8(1):327–338, jan 2019. doi:10.1080/22221751.2019.1581034.

[77] Gillian M. Air. Influenza neuraminidase. *Influenza and Other Respiratory Viruses*, 6(4):245–256, nov 2011. doi:10.1111/j.1750-2659.2011.00304.x.

[78] Jennifer L. McKimm-Breschkin. Influenza neuraminidase inhibitors: antiviral action and mechanisms of resistance. *Influenza and Other Respiratory Viruses*, 7: 25–36, dec 2012. doi:10.1111/irv.12047.

[79] Erhard van der Vries, Foekje F. Stelma, and Charles A.B. Boucher. Emergence of a multidrug-resistant pandemic influenza a (h1n1) virus. *New England Journal of Medicine*, 363(14):1381–1382, sep 2010. doi:10.1056/nejmc1003749.

[80] Matthew J. Memoli, A. Sally Davis, Kathleen Proudfoot, Daniel S. Chertow, Rachel J. Hrabal, Tyler Bristol, and Jeffery K. Taubenberger. MultiDrug-resistant 2009 pandemic influenza a(h1n1) viruses maintain fitness and transmissibility in ferrets. *The Journal of Infectious Diseases*, 203(3):348–357, feb 2011. doi:10.1093/infdis/jiq067.

[81] Victor Bandlow, Susanne Liese, Daniel Lauster, Kai Ludwig, Roland R. Netz, Andreas Herrmann, and Oliver Seitz. Spatial screening of hemagglutinin on influenza a virus particles: Sialyl-LacNAc displays on DNA and PEG scaffolds reveal the requirements for bivalency enhanced interactions with weak monovalent binders. *Journal of the American Chemical Society*, 139(45):16389–16397, nov 2017. doi:10.1021/jacs.7b09967.

[82] Victor Bandlow, Daniel Lauster, Kai Ludwig, Malte Hilsch, Valentin Reiter-Scherer, Christoph Böttcher, Jürgen Rabe, Andreas Herrmann, and Oliver Seitz. Sialyl-lacnac-pna-dna concatamers by rolling circle amplification as multivalent inhibitors for influenza a virus particles. *ChemBioChem*, dec 2018. doi:10.1002/cbic.201800643.

[83] Christoph Böttcher, Kai Ludwig, Andreas Herrmann, Marin van Heel, and Holger Stark. Structure of influenza haemagglutinin at neutral and at fusogenic pH by electron cryo-microscopy. *FEBS Letters*, 463(3):255–259, dec 1999. doi:10.1016/s0014-5793(99)01475-1.

[84] Nongluk SRIWILAIJAROEN and Yasuo SUZUKI. Molecular basis of the structure and function of h1 hemagglutinin of influenza virus. *Proceedings of the Japan Academy, Series B*, 88(6):226–249, 2012. doi:10.2183/pjab.88.226.

[85] Pallavi Kiran, Sumati Bhatia, Daniel Lauster, Stevan Aleksić, Carsten Fleck, Natalija Peric, Wolfgang Maison, Susanne Liese, Bettina G. Keller, Andreas Herrmann, and Rainer Haag. Exploring rigid and flexible core trivalent sialosides for influenza virus inhibition. *Chemistry – A European Journal*, 24(72):19373–19385, nov 2018. doi:10.1002/chem.201804826.

[86] Per A. Bullough, Frederick M. Hughson, John J. Skehel, and Don C. Wiley. Structure of influenza haemagglutinin at the pH of membrane fusion. *Nature*, 371 (6492):37–43, sep 1994. doi:10.1038/371037a0.

[87] S. Munier, T. Larcher, F. Cormier-Aline, D. Soubieux, B. Su, L. Guigand, B. Labrosse, Y. Cherel, P. Quere, D. Marc, and N. Naffakh. A genetically

engineered waterfowl influenza virus with a deletion in the stalk of the neuraminidase has increased virulence for chickens. *Journal of Virology*, 84(2):940–952, nov 2009. doi:10.1128/jvi.01581-09.

[88] Teddy Wohlbold and Florian Krammer. In the shadow of hemagglutinin: A growing interest in influenza viral neuraminidase and its role as a vaccine antigen. *Viruses*, 6(6):2465–2494, jun 2014. doi:10.3390/v6062465.

[89] M. N. Matrosovich, T. Y. Matrosovich, T. Gray, N. A. Roberts, and H.-D. Klenk. Neuraminidase is important for the initiation of influenza virus infection in human airway epithelium. *Journal of Virology*, 78(22):12665–12667, oct 2004. doi:10.1128/jvi.78.22.12665-12667.2004.

[90] Jimmy C. C. Lai, Jean-Michel Garcia, Jeffrey C. Dyason, Raphael Böhm, Paul D. Madge, Faith J. Rose, John M. Nicholls, J. S. Malik Peiris, Thomas Haselhorst, and Mark von Itzstein. A secondary sialic acid binding site on influenza virus neuraminidase: Fact or fiction? *Angewandte Chemie International Edition*, 51(9): 2221–2224, jan 2012. doi:10.1002/anie.201108245.

[91] R G Webster, G M Air, D W Metzger, P M Colman, J N Varghese, A T Baker, and W G Laver. Antigenic structure and variation in an influenza virus n9 neuraminidase. *Journal of virology*, 61:2910–2916, September 1987. ISSN 0022-538X.

[92] Jeffrey C. Sung, Adam W. Van Wynsberghe, Rommie E. Amaro, Wilfred W. Li, and J. Andrew McCammon. Role of secondary sialic acid binding sites in influenza n1 neuraminidase. *Journal of the American Chemical Society*, 132(9): 2883–2885, mar 2010. doi:10.1021/ja9073672.

[93] G. Binnig, H. Rohrer, Ch. Gerber, and E. Weibel. Surface studies by scanning tunneling microscopy. *Physical Review Letters*, 49(1):57–61, jul 1982. doi:10.1103/physrevlett.49.57.

[94] Gerd Binnig and Heinrich Rohrer. Scanning tunneling microscopy—from birth to adolescence. *Reviews of Modern Physics*, 59(3):615–625, jul 1987. doi:10.1103/revmodphys.59.615.

[95] P. Hansma, V. Elings, O Marti, and C. Bracker. Scanning tunneling microscopy and atomic force microscopy: application to biology and technology. *Science*, 242 (4876):209–216, oct 1988. doi:10.1126/science.3051380.

[96] O. MARTI, V. Elings, M. Haugan, C. E. Bracker, J. Schneir, B. Drake, S. A. C. Gould, J. Gurley, L. Hellemans, K. Shaw, A. L. Weisenhorn, J. Zasadzinski, and P. K. Hansma. Scanning probe microscopy of biological samples and other surfaces. *Journal of Microscopy*, 152(3):803–809, dec 1988. doi:10.1111/j.1365-2818.1988.tb01452.x.

[97] A Engel. Biological applications of scanning probe microscopes. *Annual Review of Biophysics and Biophysical Chemistry*, 20(1):79–108, jun 1991. doi:10.1146/annurev.bb.20.060191.000455.

[98] Daniel J Müller and Andreas Engel. Atomic force microscopy and spectroscopy of native membrane proteins. *Nature Protocols*, 2(9):2191–2197, sep 2007. doi:10.1038/nprot.2007.309.

[99] Daniel J. Müller and Yves F. Dufrêne. Atomic force microscopy as a multifunctional molecular toolbox in nanobiotechnology. *Nature Nanotechnology*, 3(5): 261–269, may 2008. doi:10.1038/nnano.2008.100.

[100] Yongho Seo and Wonho Jhe. Atomic force microscopy and spectroscopy. *Reports on Progress in Physics*, 71(1):016101, dec 2007. doi:10.1088/0034-4885/71/1/016101.

[101] R. Overney and E. Meyer. Tribological investigations using friction force microscopy. *MRS Bulletin*, 18(5):26–34, may 1993. doi:10.1557/s0883769400047096.

[102] Wenhua Liu, Keith Bonin, and Martin Guthold. Easy and direct method for calibrating atomic force microscopy lateral force measurements. *Review of Scientific Instruments*, 78(6):063707, jun 2007. doi:10.1063/1.2745733.

[103] Franz J. Giessibl. Advances in atomic force microscopy. *Reviews of Modern Physics*, 75(3):949–983, jul 2003. doi:10.1103/revmodphys.75.949.

[104] Nader Jalili and Karthik Laxminarayana. A review of atomic force microscopy imaging systems: application to molecular metrology and biological sciences. *Mechatronics*, 14(8):907–945, oct 2004. doi:10.1016/j.mechatronics.2004.04.005.

[105] Jürgen P. Rabe. Molecular workbench for imaging and manipulation of single macromolecules and their complexes with the scanning force microscope. In *Topics in Current Chemistry*, pages 77–102. Springer Berlin Heidelberg, 2008. doi:10.1007/128_2008_4.

[106] Jian Zhong and Juan Yan. Seeing is believing: atomic force microscopy imaging for nanomaterial research. *RSC Advances*, 6(2):1103–1121, 2016. doi:10.1039/c5ra22186b.

[107] Michael Krieg, Gotthold Fläschner, David Alsteens, Benjamin M. Gaub, Wouter H. Roos, Gijs J. L. Wuite, Hermann E. Gaub, Christoph Gerber, Yves F. Dufrêne, and Daniel J. Müller. Atomic force microscopy-based mechanobiology. *Nature Reviews Physics*, 1(1):41–57, nov 2018. doi:10.1038/s42254-018-0001-7.

[108] Antonio Aliano, Giancarlo Cicero, Hossein Nili, Nicolas G. Green, Pablo García-Sánchez, Antonio Ramos, Andreas Lenshof, Thomas Laurell, Aisha Qi, Peggy Chan, Leslie Yeo, James Friend, Mikael Evander, Thomas Laurell, Andreas Lenshof, Thomas Laurell, Jian Chen, Jean Christophe Lacroix, Pascal Martin, Hyacinthe Randriamahazaka, W. Jon. P. Barnes, Bart W. Hoogenboom, Kenji Fukuzawa, Hendrik Hölscher, Hendrik Hölscher, Alessia Bottos, Elena Astanina, Luca Primo, Federico Bussolino, Xuefeng Gao, Vinh-Nguyen Phan, Nam-Trung Nguyen, Chun Yang, Patrick Abgrall, Friedrich G. Barth, Pablo Gurman, Yitzhak Rosen, Orlando Auciello, C. J. Kähler, C. Cierpka, M. Rossi, Bharat Bhushan, Manuel L. B. Palacio, and Charles L. Dezelah. AFM, tapping mode. In *Encyclopedia of Nanotechnology*, pages 99–99. Springer Netherlands, 2012. doi:10.1007/978-90-481-9751-4_33.

[109] Dana Schwarz, Yu Noda, Jan Klouda, Karolina Schwarzová-Pecková, Ján Tarábek, Jiří Rybáček, Jiří Janoušek, Frank Simon, Maksym V. Opanasenko, Jiří Čejka, Amitava Acharjya, Johannes Schmidt, Sören Selve, Valentin Reiter-Scherer, Nikolai Severin, Jürgen P. Rabe, Petra Ecorchard, Junjie He, Miroslav Polozij, Petr

Nachtigall, and Michael J. Bojdys. Twinned growth of metal-free, triazine-based photocatalyst films as mixed-dimensional (2d/3d) van der waals heterostructures. *Advanced Materials*, 29(40):1703399, aug 2017. doi:10.1002/adma.201703399.

[110] Marica Marrese, Vincenzo Guarino, and Luigi Ambrosio. Atomic force microscopy: A powerful tool to address scaffold design in tissue engineering. *Journal of Functional Biomaterials*, 8(1):7, feb 2017. doi:10.3390/jfb8010007.

[111] Y. Martin, C. C. Williams, and H. K. Wickramasinghe. Atomic force microscope force mapping and profiling on a sub 100 a. 61(10):4723–4729, may 1987. doi:10.1063/1.338807.

[112] Yannan Zhao, Xiaoxing Sun, Guannan Zhang, Brian G. Trewyn, Igor I. Slowing, and Victor S.-Y. Lin. Interaction of mesoporous silica nanoparticles with human red blood cell membranes: Size and surface effects. *ACS Nano*, 5(2):1366–1375, feb 2011. doi:10.1021/nn103077k.

[113] L. Chopinet, C. Formosa, M.P. Rols, R.E. Duval, and E. Dague. Imaging living cells surface and quantifying its properties at high resolution using AFM in QI™ mode. *Micron*, 48:26–33, may 2013. doi:10.1016/j.micron.2013.02.003.

[114] Volkan Can, Zdravko Kochovski, Valentin Reiter, Nikolai Severin, Miriam Siebenbürger, Ben Kent, Justus Just, Jürgen P. Rabe, Matthias Ballauff, and Oguz Okay. Nanostructural evolution and self-healing mechanism of micellar hydrogels. *Macromolecules*, 49(6):2281–2287, feb 2016. doi:10.1021/acs.macromol.6b00156.

[115] Stefan Eilers and Jürgen P. Rabe. Manipulation of graphene within a scanning force microscope. *physica status solidi (b)*, 246(11-12):2527–2529, nov 2009. doi:10.1002/pssb.200982350.

[116] M. Radmacher, J.P. Cleveland, M. Fritz, H.G. Hansma, and P.K. Hansma. Mapping interaction forces with the atomic force microscope. *Biophysical Journal*, 66(6):2159–2165, jun 1994. doi:10.1016/s0006-3495(94)81011-2.

[117] Y. F. Dufrene. Atomic force microscopy, a powerful tool in microbiology. *Journal of Bacteriology*, 184(19):5205–5213, oct 2002. doi:10.1128/jb.184.19.5205-5213.2002.

[118] D. Bartkowiak, V. Merk, V. Reiter-Scherer, U. Gernert, J. P. Rabe, J. Kneipp, and E. Kemnitz. Porous mgf2-over-gold nanoparticles mon as plasmonic substrate for analytical applications. *RSC Advances*, 6(75):71557–71566, 2016. doi:10.1039/c6ra10501g.

[119] A L Weisenhorn, M Khorsandi, S Kasas, V Gotzos, and H J Butt. Deformation and height anomaly of soft surfaces studied with an AFM. *Nanotechnology*, 4(2): 106–113, apr 1993. doi:10.1088/0957-4484/4/2/006.

[120] J. J. Roa, G. Oncins, J. Diaz, F. Sanz, and M. Segarra. Calculation of young's modulus value by means of afm. *Recent Patents on Nanotechnology*, 5(1):27–36, jan 2011. doi:10.2174/187221011794474985.

[121] B.V Derjaguin, V.M Muller, and Yu.P Toporov. Effect of contact deformations on the adhesion of particles. *Journal of Colloid and Interface Science*, 53(2):314–326, nov 1975. doi:10.1016/0021-9797(75)90018-1.

[122] Yulia Glebova, Valentin Reiter-Scherer, Sari Suvanto, Tarmo Korpela, Tuula T. Pakkanen, Nikolai Severin, Vladimir Shershnev, and Jürgen P. Rabe. Nano-mechanical imaging reveals heterogeneous cross-link distribution in sulfur-vulcanized butadiene-styrene rubber comprising ZnO particles. *Polymer*, 107: 102–107, dec 2016. doi:10.1016/j.polymer.2016.11.011.

[123] Peter Hanggi. Escape from a metastable state. *Journal of Statistical Physics*, 42 (1-2):105–148, jan 1986. doi:10.1007/bf01010843.

[124] Manuel Gensler, Christian Eidamshaus, Arthur Galstyan, Ernst-Walter Knapp, Hans-Ulrich Reissig, and Jürgen P. Rabe. Mechanical rupture of mono- and bivalent transition metal complexes in experiment and theory. *The Journal of Physical Chemistry C*, 119(8):4333–4343, feb 2015. doi:10.1021/jp511104m.

[125] Manuel Gensler, Christian Eidamshaus, Maurice Taszarek, Hans-Ulrich Reissig, and Jürgen P Rabe. Mechanical stability of bivalent transition metal complexes analyzed by single-molecule force spectroscopy. *Beilstein Journal of Organic Chemistry*, 11:817–827, may 2015. doi:10.3762/bjoc.11.91.

[126] E. Evans. Physical actions in biological adhesion. In *Handbook of Biological Physics*, pages 723–754. Elsevier, 1995. doi:10.1016/s1383-8121(06)80008-4.

[127] E. Evans and K. Ritchie. Dynamic strength of molecular adhesion bonds. *Biophysical Journal*, 72(PMC1184350):1541–1555, April 1997. ISSN 1542-0086. URL `http://www.ncbi.nlm.nih.gov/pmc/articles/PMC1184350/`.

[128] Evan Evans. Introductory lecture energy landscapes of biomolecular adhesion and receptor anchoring at interfaces explored with dynamic force spectroscopy. *Faraday Discussions*, 111:1–16, 1999. doi:10.1039/a809884k.

[129] E. Evans and P. Williams. Dynamic force spectroscopy. In *Les Houches - Ecole d'Ete de Physique Theorique*, pages 145–204. Springer Berlin Heidelberg, 2002. doi:10.1007/3-540-45701-1_4.

[130] Evan Evans. Looking inside molecular bonds at biological interfaces with dynamic force spectroscopy. *Biophysical Chemistry*, 82(2-3):83–97, dec 1999. doi:10.1016/s0301-4622(99)00108-8.

[131] Katarzyna M. Tych, Toni Hoffmann, David J. Brockwell, and Lorna Dougan. Single molecule force spectroscopy reveals the temperature-dependent robustness and malleability of a hyperthermophilic protein. *Soft Matter*, 9(37):9016, 2013. doi:10.1039/c3sm51439k.

[132] H.A. Kramers. Brownian motion in a field of force and the diffusion model of chemical reactions. *Physica*, 7(4):284–304, apr 1940. doi:10.1016/s0031-8914(40)90098-2.

[133] Henry Eyring. The activated complex in chemical reactions. *The Journal of Chemical Physics*, 3(2):107–115, feb 1935. doi:10.1063/1.1749604.

[134] M. G. Evans and M. Polanyi. Some applications of the transition state method to the calculation of reaction velocities, especially in solution. *Transactions of the Faraday Society*, 31:875, 1935. doi:10.1039/tf9353100875.

[135] Peter Hänggi, Peter Talkner, and Michal Borkovec. Reaction-rate theory: fifty years after kramers. *Reviews of Modern Physics*, 62(2):251–341, apr 1990. doi:10.1103/revmodphys.62.251.

[136] Eli Pollak and Peter Talkner. Reaction rate theory: What it was, where is it today, and where is it going? *Chaos: An Interdisciplinary Journal of Nonlinear Science*, 15(2):026116, jun 2005. doi:10.1063/1.1858782.

[137] Sergi Garcia-Manyes, Jasna Brujc, Carmen L. Badilla, and Julio M. Fernandez. Force-clamp spectroscopy of single-protein monomers reveals the individual unfolding and folding pathways of i27 and ubiquitin. *Biophysical Journal*, 93(7): 2436–2446, oct 2007. doi:10.1529/biophysj.107.104422.

[138] O. K. Dudko, G. Hummer, and A. Szabo. Theory, analysis, and interpretation of single-molecule force spectroscopy experiments. *Proceedings of the National Academy of Sciences*, 105(41):15755–15760, oct 2008. doi:10.1073/pnas.0806085105.

[139] Anupam Garg. Escape-field distribution for escape from a metastable potential well subject to a steadily increasing bias field. *Physical Review B*, 51(21):15592–15595, jun 1995. doi:10.1103/physrevb.51.15592.

[140] E. Florin, V. Moy, and H. Gaub. Adhesion forces between individual ligand-receptor pairs. *Science*, 264(5157):415–417, apr 1994. doi:10.1126/science.8153628.

[141] V. Moy, E. Florin, and H. Gaub. Intermolecular forces and energies between ligands and receptors. *Science*, 266(5183):257–259, oct 1994. doi:10.1126/science.7939660.

[142] Gil U. Lee, David A. Kidwell, and Richard J. Colton. Sensing discrete streptavidin-biotin interactions with atomic force microscopy. *Langmuir*, 10(2):354–357, feb 1994. doi:10.1021/la00014a003.

[143] Yu-Shiu Lo, Neil D. Huefner, Winter S. Chan, Forrest Stevens, Joel M. Harris, and Thomas P. Beebe. Specific interactions between biotin and avidin studied by atomic force microscopy using the poisson statistical analysis method. *Langmuir*, 15(4):1373–1382, feb 1999. doi:10.1021/la981003g.

[144] Jean-Marie Teulon, Yannick Delcuze, Michael Odorico, Shu wen W. Chen, Pierre Parot, and Jean-Luc Pellequer. Single and multiple bonds in (strept)avidin-

biotin interactions. *Journal of Molecular Recognition*, 24(3):490–502, apr 2011. doi:10.1002/jmr.1109.

[145] Steffen M. Sedlak, Leonard C. Schendel, Marcelo C. R. Melo, Diana A. Pippig, Zaida Luthey-Schulten, Hermann E. Gaub, and Rafael C. Bernardi. Direction matters: Monovalent streptavidin/biotin complex under load. *Nano Letters*, 19 (6):3415–3421, oct 2018. doi:10.1021/acs.nanolett.8b04045.

[146] O. K. Dudko, A. E. Filippov, J. Klafter, and M. Urbakh. Beyond the conventional description of dynamic force spectroscopy of adhesion bonds. *Proceedings of the National Academy of Sciences*, 100(20):11378–11381, sep 2003. doi:10.1073/pnas.1534554100.

[147] R. W. Friddle, A. Noy, and J. J. De Yoreo. Interpreting the widespread nonlinear force spectra of intermolecular bonds. *Proceedings of the National Academy of Sciences*, 109(34):13573–13578, aug 2012. doi:10.1073/pnas.1202946109.

[148] F. T. Hane, S. J. Attwood, and Z. Leonenko. Comparison of three competing dynamic force spectroscopy models to study binding forces of amyloid-beta - 42. *Soft Matter*, 10(12):1924, 2014. doi:10.1039/c3sm52257a.

[149] Rafael Tapia-Rojo, Carlos Marcuello, Anabel Lostao, Carlos Gomez-Moreno, Juan J. Mazo, and Fernando Falo. A physical picture for mechanical dissociation of biological complexes: from forces to free energies. *Physical Chemistry Chemical Physics*, 19(6):4567–4575, 2017. doi:10.1039/c6cp07508h.

[150] Raymond W. Friddle, Paul Podsiadlo, Alexander B. Artyukhin, and Aleksandr Noy. Near-equilibrium chemical force microscopy. *The Journal of Physical Chemistry C*, 112(13):4986–4990, mar 2008. doi:10.1021/jp7095967.

[151] Aleksandr Noy and Raymond W. Friddle. Practical single molecule force spectroscopy: How to determine fundamental thermodynamic parameters of intermolecular bonds with an atomic force microscope. *Methods*, 60(2):142–150, apr 2013. doi:10.1016/j.ymeth.2013.03.014.

[152] Philip M. Morse. Diatomic molecules according to the wave mechanics. II. vibrational levels. *Physical Review*, 34(1):57–64, jul 1929. doi:10.1103/physrev.34.57.

[153] Jens Peder Dahl and Michael Springborg. The morse oscillator in position space, momentum space, and phase space. *The Journal of Chemical Physics*, 88(7): 4535–4547, apr 1988. doi:10.1063/1.453761.

[154] JERKER PORATH, JAN CARLSSON, INGMAR OLSSON, and GRETA BELFRAGE. Metal chelate affinity chromatography, a new approach to protein fractionation. *Nature*, 258(5536):598–599, dec 1975. doi:10.1038/258598a0.

[155] George B. Sigal, Cynthia Bamdad, Alcide Barberis, Jack Strominger, and George M. Whitesides. A self-assembled monolayer for the binding and study of histidine-tagged proteins by surface plasmon resonance. *Analytical Chemistry*, 68 (3):490–497, jan 1996. doi:10.1021/ac9504023.

[156] Evelyne L. Schmid, Thomas A. Keller, Zoltan Dienes, and Horst Vogel. Reversible oriented surface immobilization of functional proteins on oxide surfaces. *Analytical Chemistry*, 69(11):1979–1985, jun 1997. doi:10.1021/ac9700033.

[157] Federica Rusmini, Zhiyuan Zhong, and Jan Feijen. Protein immobilization strategies for protein biochips. *Biomacromolecules*, 8(6):1775–1789, jun 2007. doi:10.1021/bm061197b.

[158] Attila Nagy, Grzegorz Piszczek, and James R. Sellers. Extensibility of the extended tail domain of processive and nonprocessive myosin v molecules. *Biophysical Journal*, 97(12):3123–3131, dec 2009. doi:10.1016/j.bpj.2009.09.033.

[159] Claudia Friedsam, Aránzazu Del Campo Bécares, Ulrich Jonas, Hermann E. Gaub, and Markus Seitz. Polymer functionalized AFM tips for long-term measurements in single-molecule force spectroscopy. *ChemPhysChem*, 5(3):388–393, mar 2004. doi:10.1002/cphc.200300797.

[160] Valentin Reiter-Scherer, Jose Luis Cuellar-Camacho, Sumati Bhatia, Rainer Haag, Andreas Herrmann, Daniel Lauster, and Jürgen P. Rabe. Force spectroscopy shows dynamic binding of influenza hemagglutinin and neuramini-

dase to sialic acid. *Biophysical Journal*, 116(6):1037 – 1048, 2019. ISSN 0006-3495. doi:https://doi.org/10.1016/j.bpj.2019.01.041. URL `http://www.sciencedirect.com/science/article/pii/S0006349519301122`.

[161] Andreas Janshoff, Marcus Neitzert, York Oberdörfer, and Harald Fuchs. Force spectroscopy of molecular systems—single molecule spectroscopy of polymers and biomolecules. *Angewandte Chemie*, 39(18):3212–3237, sep 2000. doi:10.1002/1521-3773(20000915)39:18<3212::aid-anie3212>3.0.co;2-x.

[162] I. A. Wilson, J. J. Skehel, and D. C. Wiley. Structure of the haemagglutinin membrane glycoprotein of influenza virus at 3 a resolution. *Nature*, 289(5796): 366–373, jan 1981. doi:10.1038/289366a0.

[163] Nicholas G. Wrigley, John J. Skehel, Peter A. Charlwood, and Colin M. Brand. The size and shape of influenza virus neuraminidase. *Virology*, 51(2):525–529, feb 1973. doi:10.1016/0042-6822(73)90457-1.

[164] M. I. Chang, P. Panorchan, T. M. Dobrowsky, Y. Tseng, and D. Wirtz. Single-molecule analysis of human immunodeficiency virus type 1 gp120-receptor interactions in living cells. *Journal of Virology*, 79(23):14748–14755, nov 2005. doi:10.1128/jvi.79.23.14748-14755.2005.

[165] Colin J Barrow, Narayanan, Nair, Sanjeev, Rao, and Pullela. Design of multiligand inhibitors for the swine flu h1n1 neuraminidase binding site. *Advances and Applications in Bioinformatics and Chemistry*, page 47, aug 2013. doi:10.2147/aabc.s49503.

[166] Christopher McCullough, Minxiu Wang, Lijun Rong, and Michael Caffrey. Characterization of influenza hemagglutinin interactions with receptor by NMR. *PLoS ONE*, 7(7):e33958, jul 2012. doi:10.1371/journal.pone.0033958.

[167] Keith C. Johnson and Wendy E. Thomas. How do we know when single-molecule force spectroscopy really tests single bonds? *Biophysical Journal*, 114(9):2032–2039, may 2018. doi:10.1016/j.bpj.2018.04.002.

[168] Evan Evans and Florian Ludwig. Dynamic strengths of molecular anchoring and material cohesion in fluid biomembranes. *Journal of Physics: Condensed Matter*, 12(8A):A315–A320, feb 2000. doi:10.1088/0953-8984/12/8a/341.

[169] Senli Guo, Chad Ray, Andrea Kirkpatrick, Nimit Lad, and Boris B. Akhremitchev. Effects of multiple-bond ruptures on kinetic parameters extracted from force spectroscopy measurements: Revisiting biotin-streptavidin interactions. *Biophysical Journal*, 95(8):3964–3976, oct 2008. doi:10.1529/biophysj.108.133900.

[170] Mario B. Viani, Tilman E. Schäffer, Ami Chand, Matthias Rief, Hermann E. Gaub, and Paul K. Hansma. Small cantilevers for force spectroscopy of single molecules. *Journal of Applied Physics*, 86(4):2258–2262, aug 1999. doi:10.1063/1.371039.

[171] Ferdinand Kühner and Hermann E. Gaub. Modelling cantilever-based force spectroscopy with polymers. *Polymer*, 47(7):2555–2563, mar 2006. doi:10.1016/j.polymer.2005.12.090.

[172] Claire Verbelen, Hermann J. Gruber, and Yves F. Dufrêne. The NTA–his6 bond is strong enough for AFM single-molecular recognition studies. *Journal of Molecular Recognition*, 20(6):490–494, 2007. doi:10.1002/jmr.833.

[173] Ashok Garai, Yaojun Zhang, and Olga K. Dudko. Conformational dynamics through an intermediate. *The Journal of Chemical Physics*, 140(13):135101, apr 2014. doi:10.1063/1.4869869.

[174] Olga Dudko, Gerhard Hummer, and Attila Szabo. Intrinsic rates and activation free energies from single-molecule pulling experiments. *Physical Review Letters*, 96(10), mar 2006. doi:10.1103/physrevlett.96.108101.

[175] Gerhard Hummer and Attila Szabo. Kinetics from nonequilibrium single-molecule pulling experiments. *Biophysical Journal*, 85(1):5–15, jul 2003. doi:10.1016/s0006-3495(03)74449-x.

[176] Jakob T. Bullerjahn, Sebastian Sturm, and Klaus Kroy. Theory of rapid force spectroscopy. *Nature Communications*, 5(1), jul 2014. doi:10.1038/ncomms5463.

[177] R. Merkel, P. Nassoy, A. Leung, K. Ritchie, and E. Evans. Energy landscapes of receptor–ligand bonds explored with dynamic force spectroscopy. *Nature*, 397 (6714):50–53, jan 1999. doi:10.1038/16219.

[178] Aleksandr Noy. Force spectroscopy 101: how to design, perform, and analyze an AFM-based single molecule force spectroscopy experiment. *Current Opinion in Chemical Biology*, 15(5):710–718, oct 2011. doi:10.1016/j.cbpa.2011.07.020.

[179] P. Hinterdorfer, W. Baumgartner, H. J. Gruber, K. Schilcher, and H. Schindler. Detection and localization of individual antibody-antigen recognition events by atomic force microscopy. *Proceedings of the National Academy of Sciences*, 93(8): 3477–3481, apr 1996. doi:10.1073/pnas.93.8.3477.

[180] W. Baumgartner, H.J. Gruber, P. Hinterdorfer, and D. Drenckhahn. Affinity of trans-interacting VE-cadherin determined by atomic force microscopy. *Single Molecules*, 1(2):119–122, jun 2000. doi:10.1002/1438-5171(200006)1:2<119::aid-simo119>3.0.co;2-k.

[181] C. Rankl, F. Kienberger, L. Wildling, J. Wruss, H. J. Gruber, D. Blaas, and P. Hinterdorfer. Multiple receptors involved in human rhinovirus attachment to live cells. *Proceedings of the National Academy of Sciences*, 105(46):17778–17783, nov 2008. doi:10.1073/pnas.0806451105.

[182] Susanne Liese, Manuel Gensler, Stefanie Krysiak, Richard Schwarzl, Andreas Achazi, Beate Paulus, Thorsten Hugel, Jürgen P. Rabe, and Roland R. Netz. Hydration effects turn a highly stretched polymer from an entropic into an energetic spring. *ACS Nano*, 11(1):702–712, dec 2016. doi:10.1021/acsnano.6b07071.

[183] Susanne Liese and Roland R. Netz. Quantitative prediction of multivalent ligand–receptor binding affinities for influenza, cholera, and anthrax inhibition. *ACS Nano*, 12(5):4140–4147, feb 2018. doi:10.1021/acsnano.7b08479.

[184] Timothy V. Ratto, Robert E. Rudd, Kevin C. Langry, Rodney L. Balhorn, and Michael W. McElfresh. Nonlinearly additive forces in multivalent ligand binding to a single protein revealed with force spectroscopy. *Langmuir*, 22(4):1749–1757, feb 2006. doi:10.1021/la052087d.

[185] Todd Sulchek, Raymond W. Friddle, and Aleksandr Noy. Strength of multiple parallel biological bonds. *Biophysical Journal*, 90(12):4686–4691, jun 2006. doi:10.1529/biophysj.105.080291.

[186] T. A. Sulchek, R. W. Friddle, K. Langry, E. Y. Lau, H. Albrecht, T. V. Ratto, S. J. DeNardo, M. E. Colvin, and A. Noy. Dynamic force spectroscopy of parallel individual mucin1-antibody bonds. *Proceedings of the National Academy of Sciences*, 102(46):16638–16643, nov 2005. doi:10.1073/pnas.0505208102.

[187] Stephanie Allen, Xinyong Chen, John Davies, Martyn C. Davies, Adrian C. Dawkes, John C. Edwards, Clive J. Roberts, Joanna Sefton, Saul J. B. Tendler, and Philip M. Williams. Detection of antigen-antibody binding events with the atomic force microscope†. *Biochemistry*, 36(24):7457–7463, jun 1997. doi:10.1021/bi962531z.

[188] Philip M. Williams. Analytical descriptions of dynamic force spectroscopy: behaviour of multiple connections. *Analytica Chimica Acta*, 479(1):107–115, mar 2003. doi:10.1016/s0003-2670(02)01569-6.

[189] T. Erdmann, S. Pierrat, P. Nassoy, and U. S. Schwarz. Dynamic force spectroscopy on multiple bonds: Experiments and model. *EPL (Europhysics Letters)*, 81(4): 48001, jan 2008. doi:10.1209/0295-5075/81/48001.

[190] W. Baumgartner, P. Hinterdorfer, W. Ness, A. Raab, D. Vestweber, H. Schindler, and D. Drenckhahn. Cadherin interaction probed by atomic force microscopy. *Proceedings of the National Academy of Sciences*, 97(8):4005–4010, apr 2000. doi:10.1073/pnas.070052697.

[191] Donald J. Benton, Stephen A. Wharton, Stephen R. Martin, and John W. McCauley. Role of neuraminidase in influenza a(h7n9) virus receptor binding. *Journal of Virology*, 91(11), mar 2017. doi:10.1128/jvi.02293-16.

[192] Feng Wen and Xiu-Feng Wan. Influenza neuraminidase: Underrated role in receptor binding. *Trends in Microbiology*, 27(6):477–479, jun 2019. doi:10.1016/j.tim.2019.03.001.

[193] Miriam Cohen, Xing-Quan Zhang, Hooman P Senaati, Hui-Wen Chen, Nissi M Varki, Robert T Schooley, and Pascal Gagneux. Influenza a penetrates host mucus by cleaving sialic acids with neuraminidase. *Virology Journal*, 10(1):321, 2013. doi:10.1186/1743-422x-10-321.

[194] Jennifer C. Wilson, Milton J. Kiefel, Donald I. Angus, and Mark von Itzstein. Investigation of the stability of thiosialosides toward hydrolysis by sialidases using NMR spectroscopy. *Organic Letters*, 1(3):443–446, aug 1999. doi:10.1021/ol990652w.

[195] R. Xu, X. Zhu, R. McBride, C. M. Nycholat, W. Yu, J. C. Paulson, and I. A. Wilson. Functional balance of the hemagglutinin and neuraminidase activities accompanies the emergence of the 2009 h1n1 influenza pandemic. *Journal of Virology*, 86(17):9221–9232, jun 2012. doi:10.1128/jvi.00697-12.

List of Abbreviations

BSA	Bovine serum albumin
DFS	Dynamic force spectroscopy
dPGSA	Dendritic polyglycerol sialic acid ligand
FNDY	Friddle, Noy, De Yoreo
H1N1	Influenza virus strain A/California/04/2009pdm
H3N2	Influenza virus strain A/Aichi/2/1968
HA	Hemagglutinin
HIV	Human immunodeficiency virus
IAV	Influenza A virus
IUPAC	International Union of Pure and Applied Chemistry
IV	Influenza virus
KBE	Kramers, Bell and Evans
LBD	Ligand binding domain
NA	Neuraminidase
NTA	Nitrilo triacetic acid
NTA-GS	Nitrilo triacetic acid coated glass slide
OHPEGLA	Hydroxide polyethylene glycol lipoic acid molecule
OV	Oseltamivir
PDF	Probability density function
PEG	Polyethylene glycol
QNM	Quantitative nano-mechanical mapping
SA	Sialic acid

SAPEGLA	Sialic acid polyethylene glycol lipoic acid ligand
SAM	Self assembled monolayer
SFM	Scanning force microscopy
SMFS	Single molecule force spectroscopy
IUPAC	International Union of Pure and Applied Chemistry
ZM	Zanamivir

List of Figures

List of Tables

Publications and Contributions

Publications

1. **Force spectroscopy shows dynamic binding of influenza hemagglutinin and neuraminidase to sialic acid**
   Reiter-Scherer, V, Cuellar-Camacho, JL, Bhatia, S, Haag, R, Herrmann, A, Lauster, D, and Rabe, JP
   Biophys. J. **116** (2019), 1037-1048

2. **Sialyl-LacNAc-PNA DNA concatamers by rolling circle amplification as multivalent inhibitors for Influenza A virus particles**
   Bandlow, V, Lauster, D, Ludwig, K, Hilsch, M, Reiter-Scherer, V, Rabe, JP, Böttcher, C, Herrmann, A, and Seitz, O
   ChemBioChem **20** (2019), 159-165

3. **Twinned growth of metal-free, triazine-based photocatalyst films as mixed-dimensional (2D/3D) van der Waals heterostructures**
   Schwarz, D, Noda, Y, Klouda, J, Schwarzová-Pecková, K, Tarábek, J, Rybácek, J, Janousek, J, Simon, F, Opanasenko, MV, Cejka, J, Acharjya, A, Schmidt, J, Selve, S, Reiter-Scherer, V, Severin, N, Rabe, JP, Ecorchard, P, He, J, Polozij, M, Nachtigall, P, and Bojdys, MJ
   Adv. Mater. (2017), 1703399

4. **Nano-mechanical imaging reveals heterogeneous cross-link distribution in sulfur-vulcanized butadiene-styrene rubber comprising ZnO particles**
   Glebova, Y, Reiter-Scherer, V, Suvanto, S, Korpela, T, Pakkanen, T, Severin, N,

and Rabe, JP

Polymer **107** (2016), 102-107

5. **Nanostructural evolution and self-healing mechanism of micellar hydrogels**

   Can, V, Kochovski, Z, Reiter, V, Severin, N, Siebenbürger, M, Kent, B, Just, J, Rabe, JP, Ballauff, M, and Okay, O

   Macromolecules **49** (2016), 2281-2287

6. **Porous MgF2-over-gold nanoparticles (MON) as plasmonic substrate for analytical applications**

   Bartkowiak, D, Merk, V, Reiter-Scherer, V, Gernert, U, Rabe, JP, Kneipp, J, and Kemnitz, E

   RSC Adv. **6** (2016), 71557-71566

7. **Unraveling multiple bond kinetics of sialic acid receptors and influenza A virus hemagglutinin and neuraminidase glycoproteins**

   Jose Luis Cuellar Camacho, Sumati Bhatia, Valentin Reiter-Scherer, Daniel Lauster, Susanne Liese, Jürgen P. Rabe, Andreas Herrmann and Rainer Haag

   Manuscript under preparation

Selected Contributions to Conferences

1. **Dynamic Interactions of Influenza A Virus Proteins Hemagglutinin and Neuraminidase with Sialic Acid Revealed by Single Molecule Force Spectroscopy**

   Valentin Reiter-Scherer, Jose Luis Cuellar-Camacho, Sumati Bhatia, Daniel Lauster, Rainer Haag, Anderas Herrmann, Jürgen P. Rabe

   Polydays, Berlin, 11.-13.09.2019, (2019)

2. **Hooking on Viral Glycoproteins with Single Molecule Force Spectroscopy to Study Single and Multiple Bond Formations**

   . Lauster, V. Reiter-Scherer, J.L. Cuellar-Camacho, S. Bhatia, J.P. Rabe, R.

Haag, A. Herrmann

Biophys. J. 116 (3) Suppl. 1 (2019) 428a. DOI: 10.1016/j.bpj.2018.11.2305

3. **Characterisation of binding interaction of the influenza virus proteins hemagglutinin and neurominidase with a synthetic sialic acid receptor by single molecule force spectroscopy**

   Reiter-Scherer, V, Bhatia, S, Cuellar-Camacho, JL, Lauster, D, Haag, R, Herrmann, A, and Rabe, JP

   DPG Frühjahrstagung, BP 1.5, Berlin, 11.-16.3.2018, (2018)

4. **Single molecule force spectroscopy studies to characterize the interaction between the influenza virus proteins hemagglutinin and neuraminidase with sialic acid receptors**

   Valentin Reiter-Scherer, Sumati Bhatia, Daniel Lauster, Jose Luis Cuellar-Camacho, Rainer Haag, Andreas Herrmann, Jürgen P. Rabe 4th International Symposium of the CRC 765 "Multivalency in Chemistry and Biochemistry", Berlin, October 2016

5. **Influenza Virus Multivalency: From Single Ligand-Receptor Interactions to Full Virus Adhesion**

   Cuellar-Camacho, JL, Bhatia, S, Lauster, D, Reiter, V, Herrmann, A, Rabe, JP, and Haag, R

   Viruses 2016: At the Forefront of Virus-Host Interactions, Basel, Schweiz, 26.-28.1.2016 , (2016)

6. **Nano-structural evolution and self-healing of micellar hydrogels followed with scanning force microscopy**

   V. Reiter-Scherer, V. Can, Z. Kochovski, N. Severin, M. Siebenbürger, B. Kent, J. Just, J. P. Rabe, M. Ballauff, O. Okay

   Polydays 2016, Potsdam-Golm, (2016)

7. **Dissociation dynamics of the viral protein hemagglutinin and the cellular receptor sialic acid analyzed by single-molecule force spectroscopy**

   Reiter, V, Bhatia, S, Lauster, D, Gensler, M, Cuellar, L, Haag, R, Herrmann, A,

and Rabe, JP

DPG Frühjahrstagung, Regensburg, 6.-11.3.2016

8. **Multivalent interaction of hemagglutinin with sialic acid as studied by scanning force microscopy and force spectroscopy**

   Reiter, V, Gensler, M, Bhatia, S, Cuellar, L, Lauster, D, Haag, R, Herrmann, A, and Rabe, JP

   DPG Frühjahrstagung, Berlin, 15.-20.3.2015

9. **Multivalent interaction of hemagglutinin with sialic acid as studied by scanning force microscopy and force spectroscopy**

   Reiter, V, Gensler, M, Bhatia, S, Cuellar, L, Lauster, D, Haag, R, Herrmann, A, and Rabe, JP

   3rd International Symposium of the CRC 765 "Multivalency in Chemistry and Biochemistry", Berlin October 23 - 24, 2014

10. **Multivalency in the binding of the viral transmembrane protein hemagglutinin with the cellular receptor sialic acid studied by single molecule force spectroscopy**

    Reiter, V, Bhatia, S, Gensler, M, Sieben, C, Lauster, D, Liese, S, Herrmann, A, Haag, R, Netz, R, and Rabe, JP

    Spring Training School – COST CM1102 - MultiGlycoNano Joined meeting with the "Dynano" ITN network, 7-9 april 2014, University of Namur, Belgium

11. **Multivalency in the binding of the viral transmembrane protein hemagglutinin with the cellular receptor sialic acid studied by single molecule force spectroscopy**

    Reiter, V, Bhatia, S, Gensler, M, Sieben, C, Lauster, D, Liese, S, Herrmann, A, Haag, R, Netz, R, and Rabe, JP

    DPG Frühjahrstagung, CPP 19.15, Dresden, 30.3.-4.4.2014

12. **Single-Virus Force Measurements on sialic acid**

    Valentin Reiter, Sumati Bhatia, Manuel Gensler, Christian Sieben, Daniel Lauster, Andreas Herrmann, Rainer Haag3, and Jürgen P. Rabe

    DPG Frühjahrstagung, CPP, Regensburg, 2013

13. **Design and synthesis of custom-made inhibitors of influenza virus activity**

Christian Sieben, Daniel Lauster, Kai Ludwig, Valentin Reiter, Manuel Gensler, Jonathan Vonnemann, Sumati Bhatia, Min Shan, Susanne Liese, Roland Netz, Rainer Haag, Jürgen P. Rabe, Christoph Böttcher, Andreas Herrmann 2nd International Symposium of the CRC 765 "Multivalency in Chemistry and Biochemistry", Berlin October 23 - 24, 2012

Acknowledgements

I could never have written this thesis without the help and support of many people. I am enormously thankful for this and like to cordially thank all of them.

First of all, I thank Prof. Dr. Jürgen P. Rabe for giving me the opportunity to become a member of his group at Humboldt-University, and allowing me start working on this project, and funding me through the CRC 765 of the DFG. I am thankful for his guidance, his scientific advice and his patience. It has been a wonderful experience to contribute to many projects of different topics and extend my knowledge.

I thank all my colleagues with whom I could delve into highly interesting and challenging research and enjoy countless discussions. Especially, I thank Dr. Jose Luis Cuellar-Camacho who greatly supported me with measuring, analyzing and interpreting SFM and SMFS data. I also thank Ph.D. Sumati Bhatia for synthesizing the ligands that were used in this study and also for the interesting discussions about chemical interactions. I also thank Dr. Daniel Lauster and Prof. Andreas Herrmann for the fruitful cooperation and sharing their detailed knowledge about virus binding.

I thank Katie Herman for proof reading and teaching me proper comma placement.

I thank all members the group 'Physics of Macromolecules'. Special thanks goes to Evi Poblenz for assisting me in the laboratory and keeping the place running. Special thanks goes also to Sabine Schönherr, Sylwia Bojyarzen and Lothar Geyer for their help with administrative tasks and computer issues. It has been a pleasure to work with all my colleagues, especially Manuel Gensler, who shared the office with me and introduced me to SFM and SMFS. Furthermore, I thank Nicolai Severin, Stefan Kirstein, Jose Cojal Gonzales, Caro Falk, Egon Steeg, Rauf Abdul, Hu Lin, Bita Rezania, Fardin Gholami and all others that teamed up for some time of the journey for creating an

enjoyable working atmosphere.

I am grateful to all my friends, my parents Claudia and Franz Reiter, my parents in-law Babs and Bruno Scherer as well as my brother and sister who morally supported me on this long journey and helped me to stay on track.

I am eternally grateful to my beloved wife Michèle Scherer who stood beside me all the time with all her love, motivated me and pushed me onward when necessary.

Statutory Declaration

I declare that I have completed the thesis independently using only the literature, aids and tools specified. I have not applied for a doctor's degree in the doctoral subject elsewhere and do not hold a corresponding doctor's degree.

I have taken due note of the Faculty of Mathematics and Natural Sciences PhD Regulations, published in the Official Gazette of Humboldt-Universität zu Berlin no. 42 on July 11 2018.

Valentin D. Reiter-Scherer
Berlin;

Eidesstattliche Versicherung

Hiermit versichere ich an Eides statt, die Dissertation selbstständig und nur unter Verwendung der angegebenen Literatur, Hilfen und Hilfsmittel angefertigt zu haben. Ich habe mich nicht anderwärts um einen Doktorgrad in dem Promotionsfach beworben und besitze keinen entsprechenden Doktorgrad.

Die Promotionsordnung der Mathematisch-Naturwissenschaftlichen Fakultät, veröffentlicht im Amtlichen Mitteilungsblatt der Humboldt-Universität zu Berlin Nr. 42 am 11. Juli 2018, habe ich zur Kenntnis genommen.

Valentin D. Reiter-Scherer
Berlin;